Monthly Notices of the ROYAL ASTRONOMICAL SOCIETY

MNRAS **524,** 3396–3428 (2023) https://doi.org/10.1093/mnras/stad2042
Advance Access publication 2023 July 07

Examining NHD versus QHD in the GCM THOR with non-grey radiative transfer for the hot Jupiter regime

Pascal A. Noti [1,2★] Elspeth K. H. Lee [1★] Russell Deitrick [3] and Mark Hammond [4]

[1] *Center for Space and Habitability, Universität Bern, Gesellschaftsstrasse 6, CH-3012 Bern, Switzerland*
[2] *Physikalisches Institut, Universität Bern, Sidlerstrasse 5, CH-3012 Bern, Switzerland*
[3] *School of Earth and Ocean Sciences, Bob Wright Centre A405, University of Victoria, PO Box 1700 STN CSC, Victoria, BC V8W 2Y2, Canada*
[4] *Atmospheric, Oceanic and Planetary Physics, Clarendon Laboratory, Oxford, OX1 3PU, United Kingdom*

Accepted 2023 July 6. Received 2023 July 4; in original form 2023 February 22

ABSTRACT

Global circulation models (GCMs) play an important role in contemporary investigations of exoplanet atmospheres. Different GCMs evolve various sets of dynamical equations, which can result in obtaining different atmospheric properties between models. In this study, we investigate the effect of different dynamical equation sets on the atmospheres of hot Jupiter exoplanets. We compare GCM simulations using the quasi-primitive dynamical equations (QHD) and the deep Navier-Stokes equations (NHD) in the GCM THOR. We utilize a two-stream non-grey 'picket-fence' scheme to increase the realism of the radiative transfer calculations. We perform GCM simulations covering a wide parameter range grid of system parameters in the population of exoplanets. Our results show significant differences between simulations with the NHD and QHD equation sets at lower gravity, higher rotation rates, or at higher irradiation temperatures. The chosen parameter range shows the relevance of choosing dynamical equation sets dependent on system and planetary properties. Our results show the climate states of hot Jupiters seem to be very diverse, where exceptions to prograde superrotation can often occur. Overall, our study shows the evolution of different climate states that arise just due to different selections of Navier-Stokes equations and approximations. We show the divergent behaviour of approximations used in GCMs for Earth but applied for non Earth-like planets.

Key words: radiative transfer – methods: numerical – planets and satellites: atmospheres – planets and satellites: gaseous planets.

1 INTRODUCTION

Numerical weather and climate predictions provide useful information for our daily lives, naval and aviation safety, national policy, strategy development, and research in atmospheric science. Running numerical simulations can be computationally expensive; therefore, approximations of the Navier-Stokes equations (Navier 1823; Stokes 1845, 1846) have been proposed for global scale simulations. Bjerknes (1904) proposed the basis of the hydrostatic primitive equations (HPEs). Richardson (1922) derived a variation from Bjerknes's primitive equations to perform the first attempt at a numerical weather forecast by hand. Charney & Eliassen (1949) produced the first numerical weather model on ENIAC in 1950. Already at the dawn of numerical forecasting, Charney (1955) identified those approximations as an important obstacle to overcome.

The limits of the HPEs are still assessed to this day; for example, the energy conservation in global circulation models (GCMs) for Earth (Tort, Dubos & Melvin 2015), short-period waves at small scales (e.g. Álvarez et al. 2019), and global simulations of exoplanetary atmospheres (e.g. Mayne et al. 2019; Deitrick et al. 2020). While numerical models utilizing the primitive equations have been relatively successfully applied to Earth's atmosphere, the applicability of the primitive equation set has been questioned for exoplanet atmospheres. For example, Mayne et al. (2019) discovered important differences in the zonal advection between simulations using the 'primitive' equations and the 'full' Navier-Stokes equations [according to the nomenclature of Mayne et al. (2014a)]. Those differences in the zonal advection lead, for example, to significant differences in the atmospheric redistribution of heat in simulations of the warm and tidally locked small Neptune GJ 1214b. For hot Jupiters, Deitrick et al. (2020) see changes of 15–20 per cent in the peak zonal winds in simulations with the non-hydrostatic, deep atmospheres (NHD) and quasi-hydrostatic, deep atmosphere (QHD) equation sets.

Atmospheric simulations can be in the interest for observations of exoplanets; the era of JWST will bring us several phase curves observations of exoplanet atmospheres, ranging from hot giants to temperate terrestrials, at higher resolutions than ever before. Continuous and long duration observations combined with a larger spectral resolution, collecting area, and a wider spectral coverage ranging from 0.6 to 20 μm will lead the studies of exoplanets and their habitability to quantum leap forward in evolution (Stevenson et al. 2016; Bean et al. 2018). At the same time, Feng et al. (2016), Blecic, Dobbs-Dixon & Greene (2017), Dobbs-Dixon & Cowan (2017), Caldas et al. (2019), Flowers et al. (2019), Irwin et al. (2020), Taylor et al. (2020), Beltz et al. (2021), and Parmentier, Showman & Fortney (2021) highlight the importance of multidimensionality in interpreting observations. Therefore, simulations of the dynamics and the 3D structure of exoplanetary atmospheres are essential

★ E-mail: pascal-andreas.noti@unibe.ch (PAN); elspeth.lee@unibe.ch (EKHL)

tools for helping to understand and interpret the new observation data from JWST. Moreover, phase curve data of hot Jupiters in the optical and infrared wavelength regimes can benefit from the findings of 3D simulations of exoplanetary atmospheres: the Transiting Exoplanet Survey Satellite (Ricker et al. 2014), CHaracterising ExOPlanet Satellite (Broeg et al. 2013), the Atmospheric Remote-sensing Infrared Exoplanet Large survey (Tinetti et al. 2016), and the high altitude ballon mission EXoplanet Climate Infrared TElescope (Nagler et al. 2019). Since the 3D simulations of the exoplanetary atmospheres are necessary tools for the understanding of exoplanets, identifying significant differences between simulations with different dynamical equation sets is important.

White et al. (2005) and Mayne et al. (2014a) reviewed the shallow, deep, hydrostatic, quasi-hydrostatic, and non-hydrostatic equations (NHEs) in GCMs. For a complete overview on the NHD and QHD equation sets, see Deitrick et al. (2020). Other conventions of dynamical equation sets can also be used [e.g. Mendonça et al. (2016); Deitrick et al. (2020)].

Simulations with HPEs can represent gravity-waves and nearly geostropic motions (White et al. 2005). For representing nearly geostrophic or 'balanced' motion, much attention has been put into deriving approximations (see reviews in Norbury & Roulstone 2002a, b). Several approximations can be found in the HPEs: the 'hydrostatic' assumption, 'shallow atmosphere', 'spherical geopotential approximation', and the 'traditional approximation' (Eckart 1960).

The traditional approximation was first introduced to study the oceanic and atmospheric dynamics of Earth considering the negligible Coriolis terms in shallowness of the Earth (e.g. Eckart 1960; Gerkema et al. 2008; Zeitlin 2018). In the momentum equation, several terms go to zero (see Mayne et al. 2014a): for longitudinal wind u, the terms $2\Omega\omega\cos\phi$ (traditional approximation) and $\frac{-u\omega}{r}$ (shallow approximation); for latitudinal wind v, the term $\frac{-v\omega}{r}$ (shallow approximation); and for the vertical wind ω, the terms $2\Omega u\cos\phi$ (traditional approximation) and $\frac{u^2+v^2}{r}$ (shallow approximation). In astrophysics, the traditional approximation of rotation might describe the dynamics of gravito-inertial waves on stars (e.g. Mathis & Prat 2019) well, but it is problematic for some exoplanets such as dynamics of the warm and tidally locked small Neptune GJ 1214b, as Mayne et al. (2019) showed. The discussion of the $\cos\phi$ terms have been in contention for many years (White et al. 2005). Studies by Phillips (1990) and Thuburn, Wood & Staniforth (2002), using linearized and adiabatic analyses, showed those $\cos\phi$ terms are minor, given the parameters of Earth if the ratio of planetary rotation frequency to buoyancy frequency is very small ($\ll 1$). White et al. (2005) regarded the terms to be unsettling, because buoyancy frequency differs across the globe and diabatic processes drive the global circulation. Furthermore, they find that the $\cos\phi$ terms are problematic if the buoyancy frequency increases through climate change. Bretherton (1964) and de Verdière & Schopp (1994) showed the importance of the $\cos\phi$ terms near the equator. Moreover, the $\cos\phi$ terms become relevant for the mesoscale motion (Draghici 1989). The traditional approximation to models simulating exoplanets varies widely in their climate regimes. Therefore, we could assume that the traditional approximation might not be valid for many exoplanets.

Models with NHEs for global simulations are used for three reasons (White et al. 2005); models with HPEs cannot resolve effectively at high resolution, so Daley (1988) suggested to apply a single equation set for all scales. Secondly, Tanguay, Robert & Laprise (1990) saw that semi-implicit methods treat acoustic waves efficiently and that more accurate NHEs should be developed. Thirdly, White et al. (2005) judged the mathematically evolutionary derivations of HPEs as less mature compared to NHEs, which are designed for classical compressible fluid dynamics. Already outside the original discipline, the meteorology, some approximations perform already less well on Earth; For the dynamics of deep oceans, the $\cos\phi$ terms become more important (White et al. 2005) because of the larger ratio of the planetary rotation frequency to the buoyancy frequency. The larger ratio is due to the smaller buoyancy frequency in the ocean, by one order of magnitude (see p. 52 of Gill 1982).

For understanding the observational data better, Yamazaki, Skeet & Read (2004), Müller-Wodarg et al. (2006), Hollingsworth & Kahre (2010), and Lebonnois et al. (2010) implemented GCMs for Jupiter, Saturn, Mars, and Venus. Since first discovered (Mayor & Queloz 1995), several hundreds of exoplanets have been observed. Exoplanets and their central stars vary widely in their parameters, which makes modelling challenging (see for review Showman, Cho & Menou 2010). Hot Jupiters are of prime interest, since they represent easier targets for observation due to their large radius and the stronger thermal emitted radiation. Showman et al. (2009), Dobbs-Dixon & Lin (2008), and Dobbs-Dixon (2009) adapted some of the first GCMs to hot Jupiters.

Several groups have used GCMs or Radiative-Hydrodynamic models to study atmospheres of (ultra) hot Jupiters and warm Neptunes (e.g. Showman & Guillot 2002; Showman et al. 2009; Dobbs-Dixon, Cumming & Lin 2010; Rauscher & Menou 2010; Heng, Menou & Phillipps 2011a; Dobbs-Dixon & Agol 2013; Mayne et al. 2014b; Charnay et al. 2015; Kataria et al. 2015; Amundsen et al. 2016; Mendonça et al. 2016; Zhang & Showman 2017; Mayne et al. 2019; Carone et al. 2020; Deitrick et al. 2020; Lee et al. 2021; Deitrick et al. 2022; Lee et al. 2022). Several physical processes have been added to GCMs. Regarding radiative transfer (RT), GCMs contain the Newtonian relaxation (e.g. Showman et al. 2008; Rauscher & Menou 2010; Heng et al. 2011a; Mayne et al. 2014b; Carone et al. 2020) and multiband grey or non-grey schemes in various adaptations (e.g. Heng, Frierson & Phillipps 2011b; Rauscher & Menou 2012; Dobbs-Dixon & Agol 2013; Mendonça et al. 2018b) in studies for hot Jupiters. Such simplified RT schemes run in GCMs efficiently. The computational efficiency enables easier benchmarking between GCMs (e.g. Heng & Showman 2015) and for exploring parameters (e.g. Komacek & Showman 2016; Komacek, Showman & Tan 2017; Tan & Komacek 2019; Tan & Showman 2020) for investigations of dynamical regimes. Showman et al. (2009), Charnay et al. (2015), and Amundsen et al. (2016) combined detailed real gas, correlated-k RT schemes to GCMs, which led to more computational expensive operations. Studies such as Kataria et al. (2014, 2016), Amundsen et al. (2016), Parmentier et al. (2016), Schneider & Liu (2009), and Deitrick et al. (2022) perform GCM simulations, including real gas RT schemes. In Lee et al. (2021), they compared semigrey, non-grey picket-fence and correlated-k RT schemes and suggested to use the picket-fence scheme as simple and computationally efficient but realistic solution.

Regarding the validity, Tokano (2013) raises doubts about the primitive equations in relatively thick atmospheres. In such thick atmospheres, the ratio of scale height to the planetary radius gets sufficiently large so that the traditional approximation becomes inappropriate. Similarly, Tort et al. (2015) and Gerkema et al. (2008) analysed the limits of the primitive equations for Earth, respectively, the traditional approximation in particular. In the past decade, a few models with the full or deep Navier-Stokes equations have been developed for exoplanets: the 3D radiation-hydrodynamics model of Dobbs-Dixon & Agol (2013), the dynamical core of THOR (Mendonça et al. 2016; Deitrick et al. 2020), the modified UM ENDGame (Mayne et al. 2014b), and LFRic-Atmosphere (Adams

et al. 2019; Sergeev et al. 2023). However, only a few studies (e.g. Mayne et al. 2014b, 2019; Deitrick et al. 2020) have investigated differences between simulations with different dynamical equations for exoplanets. While Deitrick et al. 2020 uses two-stream, double-grey RT, respectively, only Mayne et al. (2019) applied a detailed real gas, correlated-k RT scheme for the comparison of the dynamical equations. They suggested to study differences emerging out of different dynamical equations by implementing a full RT solution as used in Amundsen et al. (2016).

In this study, we investigate the differing effects of simplified Navier-Stokes equations in a GCM. We use THOR GCM because of its computational efficiency and update the RT using the picket fence scheme of Lee et al. (2021). THOR allows us to simulate atmospheres with different dynamical equations, as shown by (Deitrick et al. 2020), with NHD and QHD equation sets. We will focus on the NHD and QHD equation sets in our investigation similarly.

For investigating the effects between the NHD and QHD equation sets, we analyse effects in a parameter grid space appropriate for the hot exoplanet regime. We alter the gravity, rotation period, and irradiation temperature at the top of the atmosphere separately to see the differences among the equations and their dependence of those parameters.

2 THOR MODEL

Mendonça et al. (2016) developed the open-source GCM THOR for the purpose to study exoplanet atmosphere dynamics. Further model developments were published by Mendonça et al. (2018a, 2018b, 2018c) and Deitrick et al. (2020, 2022). THOR simulates the global atmospheres in a full 3D icosahedral grid with a given horizontal resolution (customizable by the g_{levels} settings). Consequently, singularities and resolution crowding at the poles do not occur like in latitude-longitude grids.

2.1 Hydrodynamics

THOR evolves the general non-hydrostatic Euler equations (Mendonça et al. 2016). The integration schemes are horizontally explicit and vertically implicit. Mendonça et al. (2018b, 2018c) added a dry convective adjustment and a 'sponge layer' as a form of drag for numerical stability similar to most contemporary GCMs. Furthermore, the model offers hydrostatic shallow (HSS), quasi-hydrostatic deep (QHD), and non-hydrostatic deep (NHD) equation sets (Deitrick et al. 2020). In summary, the vertical momentum flux differs between both equation sets.

NHD and QHD vary mainly in three terms: $\frac{Dv_r}{Dt}$, the Langrangian derivative of the vertical velocity, $\mathcal{F}_r$, the hyperdiffusive flux, and $\mathcal{A}_r$, the vertical component of the advection term. The terms $\frac{Dv_r}{Dt}$ and $\mathcal{F}_r$ turn to zero in the QHD case. $\mathcal{A}_r = \nabla(\rho\vec{v} \otimes \vec{v})$ becomes

$$\mathcal{A}_r^{QH} = \frac{\rho \vec{v}_h \cdot \vec{v}_h}{r}, \tag{1}$$

where ρ is the density of the air, $\vec{v}_h$ the horizontal momentum vector, and r the radial distance from the centre of the planet. For a more complete review on the NHD and QHD equation sets, see Deitrick et al. (2020).

2.2 Picket-fence RT scheme

A two-stream, double-grey RT scheme is available in THOR since the update made by Deitrick et al. (2020). However, to increase the realism of the RT scheme, we use the non-grey 'picket-fence' (Chandrasekhar 1935) translated from Lee et al. (2021), who refer to the approaches of Parmentier & Guillot (2014) and Parmentier et al. (2015). The picket-fence approach of Lee et al. (2021) simulates the radiation propagating in five bands (three visible, two infrared) through the atmospheric layers. The picket fence scheme uses two representative opacities: the molecular and atomic line opacity and the general continuum opacity. The values of these opacities are derived from the Rosseland mean opacity computed through fitting functions (analytically derived by Parmentier & Guillot 2014; Parmentier et al. 2015).

Ignoring the effects of multiple scattering, the net flux, $F_{net,i}[Wm^{-2}]$, at each level i is given by the difference of the outgoing long-wave flux, $F_{IR\uparrow,i}$, to the downwards long-wave flux, $F_{IR\downarrow,i}$, and short-wave fluxes, $F_{V\downarrow,i}$,

$$F_{net,i} = F_{IR\uparrow,i} - F_{IR\downarrow,i} - F_{V\downarrow,i}. \tag{2}$$

Assuming hydrostatic equilibrium, the partial optical depth, $\Delta\tau_i$, (Parmentier & Guillot 2014), is given by

$$\Delta\tau_{i,b} = \kappa_{R,i,b}(p_i, T_i)\Delta h_i \rho_i, \tag{3}$$

where the opacity, $\kappa_{R,i,b}[m^2kg^{-1}]$, for the level i and for the band b, the height difference between levels Δh_i, and the density ρ_i determines the partial optical depth. We implemented a Bézier interpolation to compute p_i and T_i from the pressure and temperature at the layers of the model from the altitude levels. We consider the atmosphere above the model grid using a ghost layer with optical depth

$$\Delta\tau_{ghost} = \frac{\kappa_{R,top}(p_{top}, T_{top})p_{top}}{g}. \tag{4}$$

where $p[Pa]$ stands for the pressure and $g[ms^{-2}]$ for the gravity. The Rosseland mean opacity is calculated (Parmentier et al. 2015) as

$$\frac{1}{\kappa_R} \equiv \frac{\int_0^\infty \frac{1}{\kappa_\lambda}\frac{dB_\lambda}{dT}\,d\lambda}{\int_0^\infty \frac{dB_\lambda}{dT}\,d\lambda}, \tag{5}$$

where $\kappa_\lambda[m^2g^{-1}]$ is the wavelength-dependent opacity and $dB - \lambda/dT$ is the temperature derivative of the Planck function. In order to quantify the non-greyness of the atmosphere, $\kappa_{i,b}$ is computed for each level as well as for each V and IR band through the relation

$$\kappa_{P,i,b} \equiv \gamma_b \kappa_{R,i,b}(p_i, T_i), \tag{6}$$

where γ_b is the opacity ratio coefficient (Parmentier & Guillot 2014; Parmentier et al. 2015) for each band, b, and $\kappa_R(p_i, T_i)[m^2kg^{-1}]$ is the Rosseland mean opacity for each band b. Adding the opacity ratio coefficient to equations (3) and (4), the equations become

$$\Delta\tau_{i,b} = \gamma_b\kappa_{R,i,b}(p_i, T_i)\Delta h_i \rho_i, \tag{7a}$$

$$\Delta\tau_{ghost} = \frac{\gamma_b\kappa_{R,top,b}(p_{top}, T_{top})p_{top}}{g}, \tag{7b}$$

where $\gamma_b = 1$ accounts for a grey atmosphere and $\gamma_b > 1$ for a non-grey atmosphere in the band b (King 1956). Applying the formation definition in equation (5), the Rosseland mean opacity is computed from fitting function and tables in Freedman et al. (2014).

The γ_b, β, and the Bond albedo, A_B, depend on the effective temperature, $T_{\rm eff}[K]$. Therefore, $T_{\rm eff}[K]$ is computed in advance according to Parmentier et al. (2015) for each column as

$$T_{\rm eff} = \sqrt[4]{T_{int}^4 + (1 - A_B)\mu_\star T_{irr}^4}, \tag{8}$$

where $T_{int}[K]$ is the internal temperature, $\mu_\star = \cos\phi\cos\theta$ the cosine angle from the sub-stellar point, A_B the Bond albedo, and T_{irr} the

irradiation temperature at the substellar point. Equation (8) simplifies to $T_{\rm eff} = T_{int}$ for night-side profiles. We use the fit of Parmentier et al. (2015) to the Bond albedo, A_B, which depends on g, the gravity, and $T_{\rm eff}$.

The RT scheme operates for each column as follows:

(i) Computation of the Bond albedo according to Parmentier et al. (2015), with $T_{\rm eff}$ assuming $\mu_\star = 1/\sqrt{3}$.
(ii) Computation of all γ_b and β with $T_{\rm eff}$ calculated according to equation (8) for each column and according to the fitting coefficient tables in Parmentier et al. (2015) and definitions in Parmentier & Guillot (2014).
(iii) Compute the IR band Rosseland mean opacity, $\kappa_R(p_i, T_i)$, in each layer from the fits and tables of Freedman et al. (2014).
(iv) Compute the V band opacities in each layer using the γ_b and κ_R relationships as in the equation (6).
(v) Compute the IR band opacities in each layer using the γ_b and κ_R relationships as in the equations (6).
(vi) Compute the optical depth as in the equation(7b).
(vii) Compute the two-stream calculations for each V and IR band.

2.2.1 *Short-wave radiation*

For the stellar flux at the top of the atmosphere, F_0 $[Wm^{-2}]$ is given by the irradiation temperature, $T_{irr}[K]$ (Guillot 2010) as

$$F_0 = \sigma T_{irr}^4 = \left(\frac{R_\star}{a}\right)^2 \sigma T_\star^4, \tag{9}$$

where $\sigma[Wm^{-2}K^{-4}]$ is the Stefan–Bolzmann constant, $R_\star[m]$ the stellar radius, $a[m]$ the semimajor axis, and $T_\star[K]$ the effective temperature of the star.

The downward shortwave flux at each layer i is summed over the short-wave bands with the optical depth to layer i, $\tau_{i,b}$

$$F_{V\downarrow,i} = (1 - A_B) F_0 \mu_\star \sum_{b=1}^{N_b} \beta_{V,i} \exp\left(-\frac{\tau_{i,b}}{\mu_\star}\right), \tag{10}$$

where N_b stays for the number of V bands (3 in this study) and $\beta_{V,i}$ the fraction of stellar flux in band b (1/3 in this study).

2.2.2 *Long-wave radiation*

We implement a two-stream solution using the short characteristic method with linear interpolants introduced by Olson & Kunasz (1987). The downward intensity, the intensity of the ghost layer, the upward intensity, and the upward intensity at the bottom $I_{IR,g,i}[Wm^{-2}sr^{-1}]$ at levels i and in IR bands for a Gaussian quadrature g point are given by

$$I_{\downarrow,IR,g,i} = (\epsilon_{0i} - 1) I_{\downarrow,IR,g,i+1} + \alpha_i^- B_{i+1,IR} + \beta_i^- B_{i,IR}, \tag{11a}$$

$$I_{\downarrow,IR,g,ghost} = [1 - \exp(\tau_{IR,top})/\mu_g] B_{top-1}, \tag{11b}$$

$$I_{\uparrow,IR,g,i} = (\epsilon_{0i} - 1) I_{\uparrow,IR,g,i-1} + \beta_i^+ B_{i,IR} + \gamma_i^+ B_{i-1,IR}, \tag{11c}$$

$$I_{\uparrow,IR,g,bottom} = B_{int} + I_{\downarrow,IR,g,bottom}, \tag{11d}$$

where

$$\epsilon_{0i} = 1 - exp(-\Delta\tau_{IR,i}/\mu_g), \tag{12a}$$

$$\epsilon_{1i} = \Delta\tau_{IR,i}/\mu_g - 1 + exp(-\Delta\tau_{IR,i}/\mu_g) = \Delta\tau_{IR,i}/\mu_g - \epsilon_{0i}, \tag{12b}$$

with the coefficients for linear interpolation

$$\alpha_i^- = \epsilon_{0i} - \epsilon_{1i}/\Delta\tau_{IR,i}, \tag{13a}$$

$$\beta_i^- = \epsilon_{1i}/\Delta\tau_{IR,i}, \tag{13b}$$

$$\gamma_i^- = 0, \tag{13c}$$

$$\alpha_i^+ = 0, \tag{13d}$$

$$\beta_i^+ = \epsilon_{1i}/\Delta\tau_{IR,i}, \tag{13e}$$

$$\gamma_i^+ = \epsilon_{0i} - \epsilon_{1i}/\Delta\tau_{IR,i}, \tag{13f}$$

and for optical depth lower than 10^{-6}, the coefficients are set to

$$\alpha_i^- = 0.5 \cdot \epsilon_{0i}(B_{IR,i+1} + B_{IR,i})/B_{IR,i+1}, \tag{14a}$$

$$\beta_i^- = 0, \tag{14b}$$

$$\gamma_i^- = 0, \tag{14c}$$

$$\alpha_i^+ = 0, \tag{14d}$$

$$\beta_i^+ = 0.5 \cdot \epsilon_{0i}(B_{IR,i} + B_{i-1,b})/B_{IR,i}, \tag{14e}$$

$$\gamma_i^+ = 0, \tag{14f}$$

which reduces to the isothermal approximation to avoid numerical instability. μ_g is the emission angle, and $B_{IR,i}[Wm^{-2}sr^{-1}]$ is the wave-length integrated blackbody intensity defined as

$$B_{IR,i} = \beta_{IR} B_i = \beta_{IR} \sigma T_i^4/\pi, \tag{15}$$

where $\beta_{IR,b}$ is the fraction of flux in band b. This forces the RT scheme to return to the isothermal approximation at low optical depths where numerical stability would be an issue. The upward and downward long-wave fluxes $F_{IR,i}[Wm^{-2}]$ are given by

$$F_{IR\downarrow,i} = 2\pi \sum_{b}^{N_{IR}} \sum_{g}^{N_g} w_g \mu_g I_{\downarrow,IR,g,i} \tag{16a}$$

$$F_{IR\uparrow,i} = 2\pi \sum_{IR}^{2} \sum_{g}^{5} w_g \mu_g I_{\uparrow,IR,g,i}, \tag{16b}$$

where N_{IR} is the number of IR bands (here 2), N_g the number of Gauss quadrature points (here 2), and w_g the quadrature weight.

2.3 Altitude setup

Strong temperature gradients pose a problem in the simulations with a low vertical resolution. Instead of increasing vertical resolution, which would increase numerical cost, we instead alter the relative thickness of the atmosphere layers. Where the temperature gradient remains relatively constant (e.g. deeper atmosphere), a higher thickness can be tolerated. Therefore, we create a function, which increases the vertical resolution at a chosen relative height, h_{rel}, defined by

$$h_{lev}(i) = z(i) h_{top}, \tag{17a}$$

$$h_{lay}(i) = [h_{lev}(i) + h_{lev}(i+1)]/2, \tag{17b}$$

where i stands for the height index, h_{lev} for the altitude at the levels (interfaces), h_{lay} for the altitude at the layers, h_{top} is the chosen top altitude of the model, $z(i)$ is the relative height and was defined by

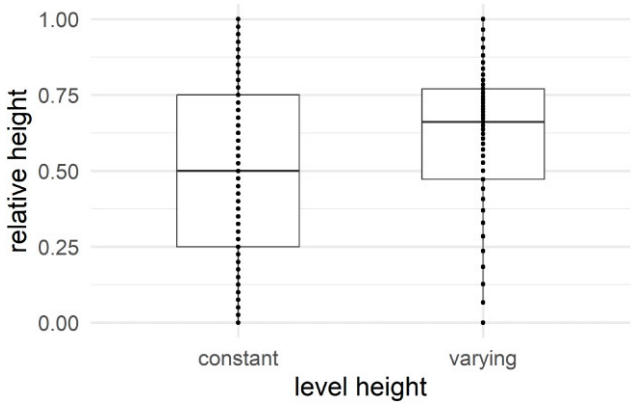

Figure 1. Distribution of the cumulative heights of the levels in the new varying height setting compared to the standard setting with constant level heights.

$$y(i) = a(i-c)^3 + b(i-d)^2, \tag{18a}$$

$$z(i) = \frac{y(i) + y(0)}{y(N_{lev}-1) + y(0)}, \tag{18b}$$

where c and d are parametrized as

$$c = \frac{h_{rel}(N_{lev}-1)}{2} + \frac{b}{3a} + \frac{(N_{lev}-1)}{4}, \tag{19a}$$

$$d = \frac{1}{2}, \tag{19b}$$

where a and b are parameters that can be chosen. In this study, we set $h_{rel} = 0.7$, $a = 1$, and $b = 6$ for our simulations. Fig. 1 illustrates the different heights of the levels in the new setting compared to the standard setting. The new scheme aims to have a slightly smother T-p profiles where temperature gradients are large like at pressures $p < 10^5\ Pa$.

2.4 Initial condition setup

We assume an initial T-p profile given by the picket-fence analytical solution at the substellar point. We implemented the suggestion of Sainsbury-Martinez et al. (2019) aiming for a hot adiabatic profile for the deep atmosphere of hot Jupiters. Furthermore, a hotter T-p profile can quickly cool down towards a realistic adiabatic gradient compared to a warming up from colder temperatures. The internal temperature, $T_{int}[K]$, was calculated in advance using the expression of Thorngren, Gao & Fortney (2019). A pressure grid with 1000 grid points is generated by

$$p(x) = p_{ref}\, e^{-\frac{20(x)}{10^3}}, \tag{20}$$

where p_{ref} is the reference pressure. The opacity at the layer i is defined as

$$\tau_i = \tau_{i+1} + \kappa(p_{i+1}, T_{i+1})(p_i - p_{i+1})/g. \tag{21}$$

The scheme of the initial conditions operates as follows:

(i) Computation of the Bond albedo, according to Parmentier et al. (2015), with $T_{\rm eff}$ assuming $\mu_\star = 1/\sqrt{3}$.

(ii) Computation of all γ_b, γ_p, and β with $T_{\rm eff}$ calculated, according to equation (8), for each column and according to the fitting coefficient tables in Parmentier et al. (2015) and definitions in Parmentier & Guillot (2014).

(iii) Computation of the IR band Rosseland mean opacity, $\kappa_R(p_i, T_i)$, in each layer from the fits and tables of Freedman et al. (2014).

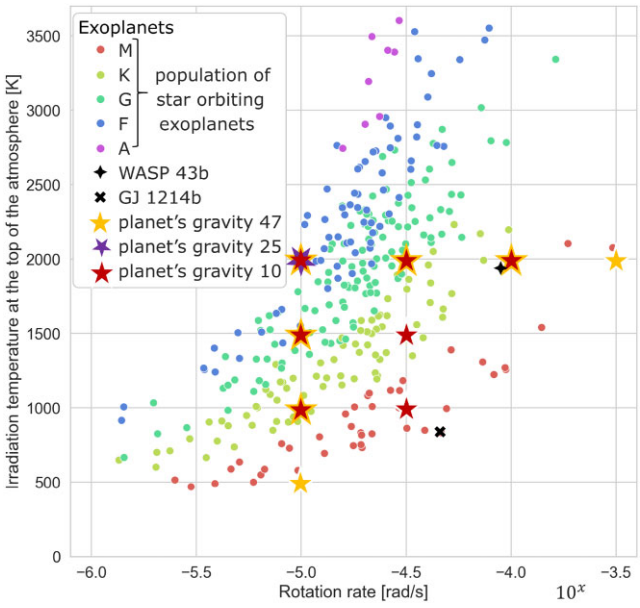

Figure 2. Grid of simulated exoplanetary parameters compared to the known exoplanets organized by host star type (retrieved on the 2021 November 22 from the entries with sufficient information in the NASA Exoplanet Archive – Akeson et al. 2013).

(iv) Computation of the temperature from the top to the bottom of the atmosphere with a first guess, followed by a convergence loop.

(v) Computation of the adiabatic correction of the initial T-p profile according to Parmentier et al. (2015).

(vi) Computation of an initial altitude grid, in addition to the T-p profile, with the hydrostatic equation in the bottom up approach.

(vii) Interpolation of the temperature with both altitude grids and the initial temperature structure.

(viii) Computation of the T-p profile with the hydrostatic equation and the reference pressure from bottom up.

3 TEST CASES

For investigating the differences between the NHD and QHD equation sets, we run simulations across a parameter grid. In the JWST mission, WASP 43b will be among the first exoplanets to be observed with the MIRI/LRS instrument (Bean et al. 2018; Venot et al. 2020), and many more exoplanets will follow in the coming years. Therefore, we used WASP 43b as role model planet and altered only the parameters for the rotation rate Ω, g and $T_{\rm eff}$. The $T_{\rm eff}$ in the equation (8) was changed in the way that the T_{irr} reaches our targeted values. Additionally, we analyse the effects rising from altering Ω, g, and $T_{\rm eff}$ with regard to the differing terms $\frac{Dv_r}{Dt}$, $\mathcal{F}_r$ and $\mathcal{A}_r$ in the NHD and QHD case. Due to the lack of computational resources, we performed simulations across nine parameter sets. Fig. 2 illustrates the grid values with the altering Ω, g, and $T_{\rm eff}$ one by one. Table 1 lists the other parameters for the simulations. For the divergence-damping and hyperdiffusion coefficients, we follow the suggestions by Hammond & Abbot (2022). The simulations are computed over 5100 d. We take the mean of the last 10 outputs covering 100 d. Each pair of NHD-QHD simulations share the same altitude grid. To compare the 18 simulations, the outputs are interpolated and extrapolated to pressures ranging from 10^8 to $10^3\ Pa$. For the first 100 d, D_{div} and $D_{hyp,\,v}$ was increased by a factor of 10 to damp waves caused by initial instabilities.

Table 1. Defined parameters for the all simulations.

Symbol	Model runs	Units	Description	Source
R_p	72 427 000	(m)	Planet radius	Gillon et al. (2012)
g	10 25 47.39	$[m\,s^{-2}]$	Gravity	-
Ω	10^{-5}, $10^{-4.5}$, 10^{-4}	$[rad\,s^{-1}]$	Rotation rate	
R_d	3714	$(JK^{-1}kg^{-1})$	Gas constant	Deitrick et al. (2020)
C_p	13 000	$(JK^{-1}kg^{-1})$	Atmospheric heat capacity	Deitrick et al. (2020)
P_{ref}	1×10^8	(Pa)	References pressure at the bottom	-
T_{int}	535	(K)	temperature of internal heat flux	according to Thorngren et al. (2019)
T_{irr}	500, 1000, 1500, 2000	(K)	Irradiation temperature at TOA	-
$T_\star$	1108, 2217, 3325, 4434	(K)	Stellar effective temperature	computed from T_{irr} see Guillot (2010)
$R_\star$	0.667	-	Stellar radius ratio relative to Earth	Gillon et al. (2012)
a	0.01525	(au)	Orbital distance	Gillon et al. (2012)
met	0	-	stellar metalicity [Fe/H]	-
Δt_M	300	(s)	Time step	-
$t_{M,\,tot}$	5100	$(Earth\ days)$	Run length	-
g_{level}	5	-	Grid refinement level ($g_{level} = 5 \sim 2^\circ$)	-
v_{layer}	40	-	Number of vertical layers	-
$O_{hyp,\,v}$	6	-	Order of hyperdiffusion operator	Hammond & Abbot (2022)
D_{div}	0.01	-	Divergence damping coefficient	Hammond & Abbot (2022)
$D_{hyp,\,h}$	0.0025	-	Horizontal hyperdiffusion coefficient	Hammond & Abbot (2022)
$D_{hyp,\,v}$	0.001	-	Vertical hyperdiffusion coefficient	Hammond & Abbot (2022)
η_{sp}	0.8	-	Bottom of sponge layer (fraction of z_{top})	Hammond & Abbot (2022)
$k^R_{sp,h}$	0.001	(s^{-1})	Horizontal Rayleigh sponge strength	Hammond & Abbot (2022)
$k^R_{sp,v}$	0.0001	(s^{-1})	Vertical Rayleigh sponge strength	-
k^{HD}_{sp}	0.01	(s^{-1})	Hyperdiffusive sponge strength	Hammond & Abbot (2022)
n_{lats}	20	-	Number of sponge layer latitude bins	Deitrick et al. (2020)

In our results, we compare and contrast the NHD and QHD T-p profiles, maps showing the temperature and horizontal wind velocity at $10^4\,Pa$, mean zonal wind, vertical and horizontal momenta-pressure profiles, Outgoing Longwave Radiation (OLR), OLR phase curve, and radiative and zonal wind time-scales. Additionally, we generate further composites with NHD and QHD equation sets, which we present in the **supplementary file**; temperature, horizontal and vertical wind at $10^4\,Pa$, the streamfunction Ψ, the tidally locked streamfunction Ψ', the components of the Helmholtz decomposition, vertical and horizontal density acceleration, and the sign of the $\frac{v tan(\Phi)}{10w} - 1$ for quality assessment (Mayne et al. 2019). The vertical and horizontal (zonal) density acceleration is computed as in Hammond, Tsai & Pierrehumbert (2020) and Hammond & Lewis (2021). In the discussion, we classify the results into climate states based on the simulations with the NHD case and relate the results to the literature. Furthermore, we computed (large-scale flow) characteristic quantities and scales, including the scale height H, Rossby number Ro, Rossby deformation radius L_D, Rhines scale, and the Brunt–Väisälä frequency N. We relate these characteristic values to climate states in the discussion. Sections A–F of the appendix describe how the tidally locked coordinates and wind, the streamfunction Ψ, the tidally locked streamfunction Ψ', Helmholtz decomposition, the OLR phase curve, the radiative and zonal time-scales, and the large-scale flow quantities and scales are calculated.

4 RESULTS

4.1 Altering rotation rate

Fig. 3 shows T-p profiles (vertical temperature-pressure profiles) for the NHD and QHD equation sets with $g = 10\,ms^{-2}$, $T_{irr} = 2000\,K$, and altering Ω. Looking at the differences between the NHD and QHD equation sets at the slow rotation rate, the regions around the eastern terminator and antistellar point reach much lower temperatures in the NHD case at pressures $<50\,000\,Pa$. In contrast, the areas around the poles and western terminator are warmer in the NHD case. At the fast rotation rate, the temperature differences between the NHD and QHD cases increase by two times in many regions. The temperatures at antistellar point, eastern terminator, and western terminator differ more than 1000, 800, and $450\,K$ at pressures $<10^5\,Pa$. In general, the differences in temperatures diminish at higher pressures. In the lower atmosphere, the high rotation rate produces larger temperature differences. At the low rotation rate, temperature differences almost vanish in the deep atmosphere.

Fig. 4 shows the temperature and horizontal wind at $10^4\,Pa$ for the NHD and QHD equation sets with $g = 10\,ms^{-2}$, $T_{irr} = 2000\,K$ and altering Ω. The NHD case shows a hotspot shift to the east at low Ω. Increasing Ω leads to smaller hotspot shifts to the east. The QHD case leads to the opposite effect with a larger shift to the east with higher Ω. Regarding the horizontal wind, we see strong divergence at the substellar point at low Ω in the NHD case. Higher Ω cause more deflection by Coriolis forces. Furthermore, jets have evolved at high latitudes on the eastern hemisphere, while a retrograde equatorial jet occurs on the western hemisphere. The QHD case has evolved a large jet spanning from pole to pole at low and high Ω, but a different wind field at moderate Ω interestingly. The wind field at moderate Ω looks similar to the NHD case, but varies at different pressures. The different wind field to the NHD case leads to different advection at low and high Ω. Therefore, the NHD case has lower temperatures at the nightside and higher temperatures at the poles than the QHD case.

Fig. 5 shows the zonal mean wind for the NHD and QHD equation sets with $g = 10\,ms^{-2}$, $T_{irr} = 2000\,K$, and altering Ω. We see a three-prograde jet system at all Ω in the NHD case and at some

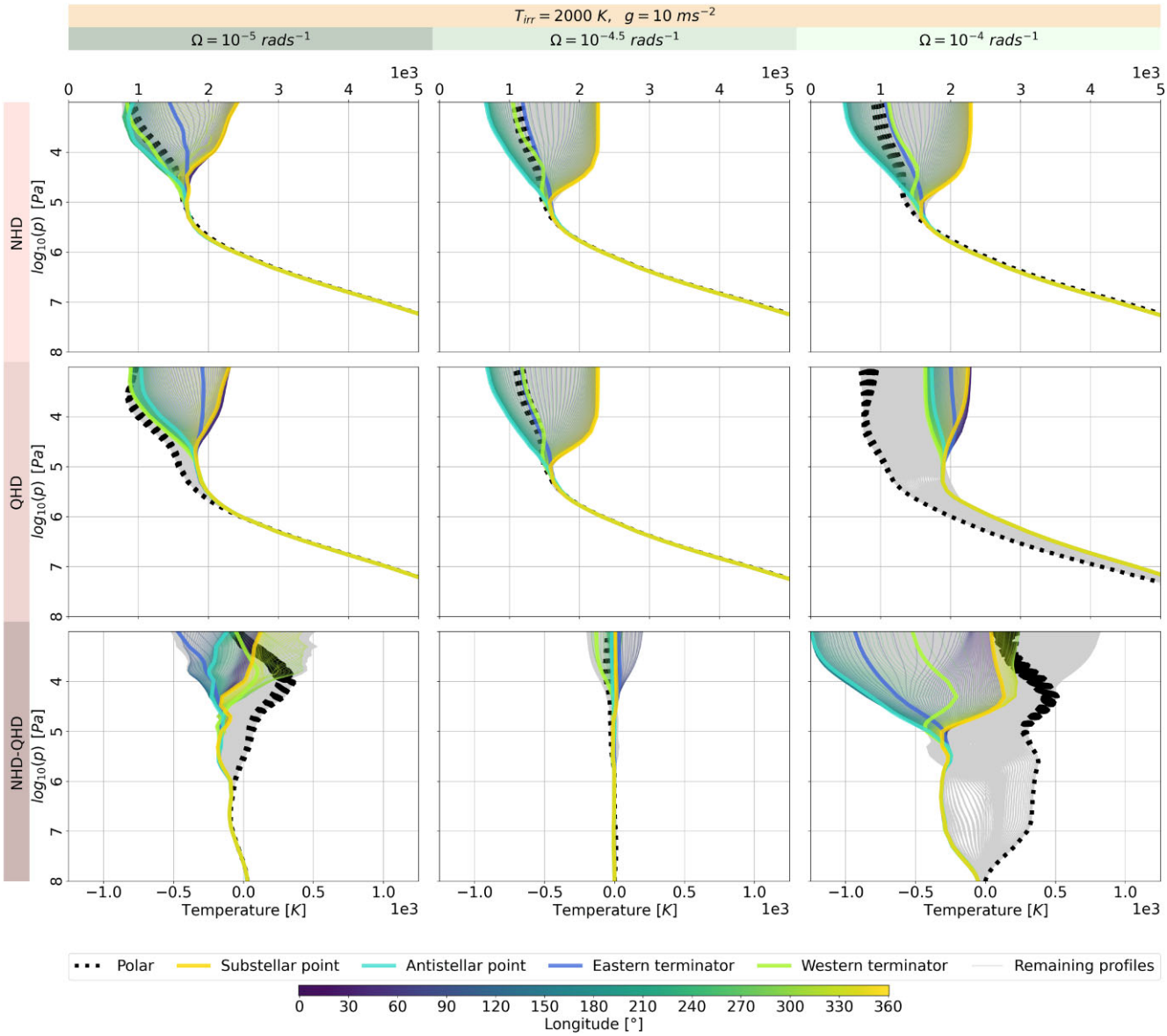

Figure 3. T-p profiles of covering entire planet for the NHD and QHD equation sets with $g = 10\,ms^{-2}$, $T_{irr} = 2000\,K$, and with altering Ω. The coloured lines indicate T-p profiles along the equator and its coordinates by the colourbar. The dotted black thin line shows T-p profiles at the latitudes 87°N and 87°S. The bold coloured lines represent T-p profiles at the western, eastern terminators, sub-, and antistellar point. The grey lines represents all the other T-p profiles.

Ω in the QHD case. The QHD case seems to be in transition to a two-prograde jet system with superrotation at low Ω. We ignore the very top layers because they might be affected by extrapolation and boundary conditions in some simulations. The QHD case has much higher horizontal wind speeds, which increase with Ω, except for the moderate Ω. There is a deep retrograde jet at low Ω in both cases but more pronounced in the NHD case. The height of the westerlies decreases faster as the rotation rate gets in the NHD case at pressure $p < 10^6\,Pa$ (in the upper atmosphere), as observed in Showman, Lewis & Fortney (2015).

Fig. 6 shows the zonal momenta $[kg/m^3 m\,s^{-1}]$ along vertical profiles at each grid point for NHD and QHD equation sets with $g = 10\,ms^{-2}$, $T_{irr} = 2000\,K$, and altering Ω (without the deep atmosphere). Throughout all profiles and simulation cases, the range of the momenta gets smaller with higher altitude mainly due to decreasing density. The QHD case would follow the same trend at pressure $p < 10^6\,Pa$, if the simulation of the moderate rotation rate did not resemble the NHD case. In the NHD case at the poles, the zonal momenta changes from a divergent to a more zonal field of momenta (see divergent component of the Helmholtz decomopostion in the **supplementary file**). The balance between eastward acceleration and vertical advection of westward momentum (Showman & Polvani 2011) favours westward winds above major westerly jet at lower latitudes in the upper atmosphere at higher rotation rates. The QHD simulations show two regime changes at pressure $p < 10^5\,Pa$ with increasing rotation rate. At high rotation rates, high positive momenta dominates at pressure $p < 10^7\,Pa$, and the flow pattern varies qualitatively to the NHD simulations. Interestingly, the flow pattern in the QHD case is qualitatively much more similar to that of the NHD case at moderate rotation rate at pressure $p < 10^5\,Pa$ (in the upper atmosphere). But in the deep atmosphere (at pressure $p > 10^5\,Pa$, the dynamical regime of the QHD case varies from that of the

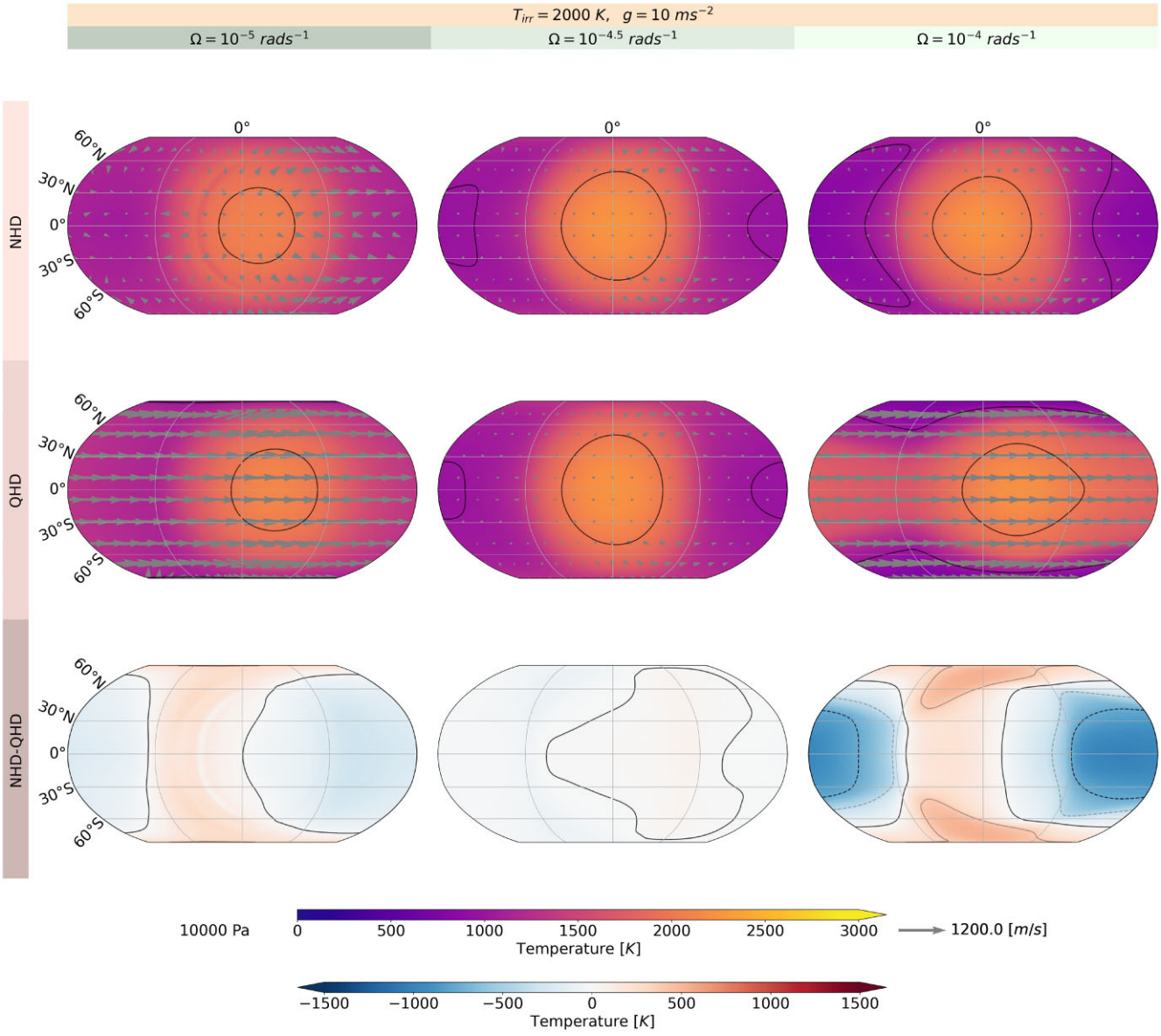

Figure 4. Temperature and wind speed at $10^4\ Pa$ for the the NHD and QHD equation sets with $g = 10\,ms^{-2}$, $T_{irr} = 2000\,K$, and with altering Ω.

NHD case substantially. Considering the entire simulated altitudes, the simulation with the QHD case has the smaller range of zonal momenta than the NHD case at low rotation rate. But at high rotation rate, range of the QHD case exceeds by around five times that of the NHD case at high rotation rates.

Fig. 7 shows the vertical momenta $[kgm^{-3}ms^{-1}]$ along vertical profiles at each grid point for the NHD and QHD equation sets with $g = 10\,ms^{-2}$, $T_{irr} = 2000\,K$, and altering Ω (without the deep atmosphere). The maxima of the upward momenta sinks to higher pressure the faster the planet rotates as observed in Showman et al. (2015).

Fig. 8 shows the phase curves of the upward flux at the top of the atmosphere (OLR) for the NHD and QHD equation sets with $g = 10\,ms^{-2}$, $T_{irr} = 2000\,K$, and altering Ω. The OLR reaches the highest values in the NHD case at the lowest rotation rate, whereas the QHD case does at moderate rotation rate. Furthermore, the hotspot is shifted more eastwards in the QHD case at low and high rotation rates (see the phase curves). At high rotation rate, the gap between the hotspot shifts in the simulations with the QHD and NHD equation sets developed the largest at high rotation rate. At moderate rotation, the difference in the hotspot shifts reaches the smallest value. In the region around the eastern terminator and on the night side, the NHD case remains cooler.

Fig. 9 shows the radiative and zonal wind time-scales for the NHD and QHD equation sets with $g = 10\,ms^{-2}$, $T_{irr} = 2000\,K$, and with altering Ω. The radiative time-scales vary less than the zonal wind time-scales for the NHD and QHD equations sets. The radiative time-scales on the dayside is conserved more than other time-scales when the planet rotates faster. Above about $10^5\ Pa$, the radiative time-scales on the day- and nightside remain the shortest for the NHD and QHD case. Furthermore, the radiative time-scales on the day- and nightside fall together in the deep atmosphere. But at pressures $p < 10^5\ Pa$, the radiative time-scales on the day- and nightside start to divert more and more in both cases. Around $10^5\ Pa$, we see the time-scales of the zonal wind become the shortest for both cases. For the slow and fast rotation rates, there may be a few switches between radiative and dynamical time-scales to be the shortest.

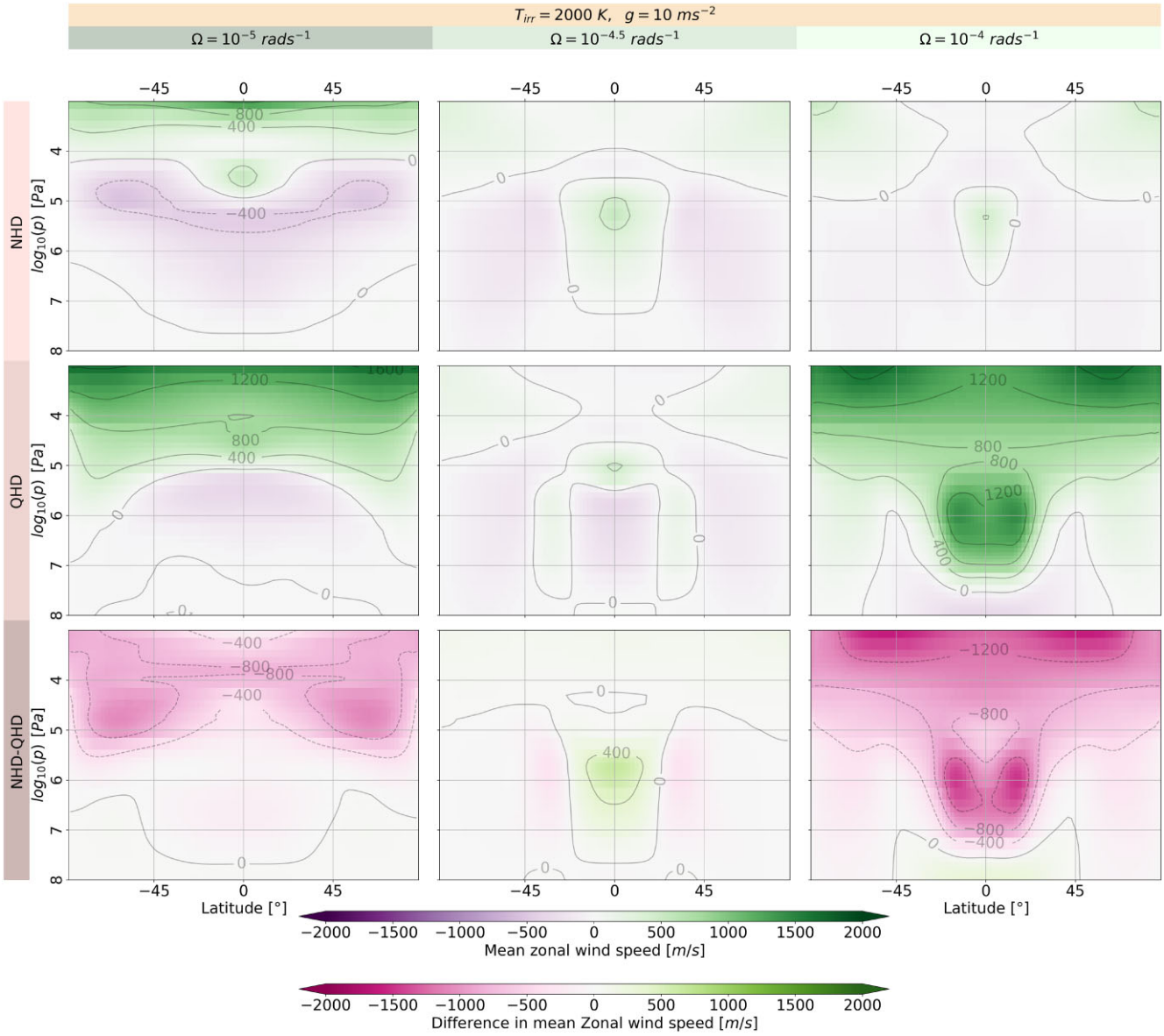

Figure 5. Zonal mean wind at each grid point for the NHD and QHD equation sets with $g = 10\,ms^{-2}$, $T_{irr} = 2000\,K$, and with altering Ω.

Regarding differences between the NHD and QHD equation sets, we see most differences occurring in the time-scale of the zonal wind. At the fast rotation rate, the QHD equation set shortens the time-scale of the zonal wind throughout the atmospheres, especially in the deep atmosphere. We see a slightly higher radiative time-scales on the dayside respectively lower on the nightside, which speaks for an higher heat transport in the QHD case. There is an increase in the time-scales of the zonal wind in the NHD case when the planet rotates faster. Whereas the QHD equation set leads to an decrease of the zonal wind time-scales in the deep atmosphere when the planet's rotation increases.

4.2 Altering gravity

Fig. 10 shows the T-p profiles for the NHD and QHD equation sets with the same $\Omega = 1 \times 10^{-5}\ rad\,s^{-1}$, $T_{irr} = 2000\,K$, and with altering g. Looking at similarities between NHD and QHD equation sets, when the spread of temperatures shrinks, the gravity becomes stronger. The decreasing day-night contrast occurs together with additional inversions and increasing rotation rates. The number of inversions increases in the T-p profiles around the equator with higher gravity. Furthermore, the base of the lowest inversions reach higher pressures the larger the gravity gets. Therefore, the temperatures are substantially lower in the deep atmosphere with higher gravity.

Looking at pressures $p \sim 10^5\ Pa$, differences between simulations with NHD and QHD equation sets, we see a decrease in the differences the stronger the gravity gets.

Fig. 11 shows the temperature and horizontal wind at $10^4\ Pa$ for the NHD and QHD equation sets with the same $\Omega = 1 \times 10^{-5}\ rad\,s^{-1}$, $T_{irr} = 2000\,K$, and with altering g. While the hotspot shift has an eastern offset at low g, it gets a western offset at higher g. The hotspot shift comes along with retrograde jet, ranging to high latitudes with much higher wind speeds. The offset got larger with the high wind speeds, but decreases with higher g. Differences between the NHD and QHD case decreases with higher g.

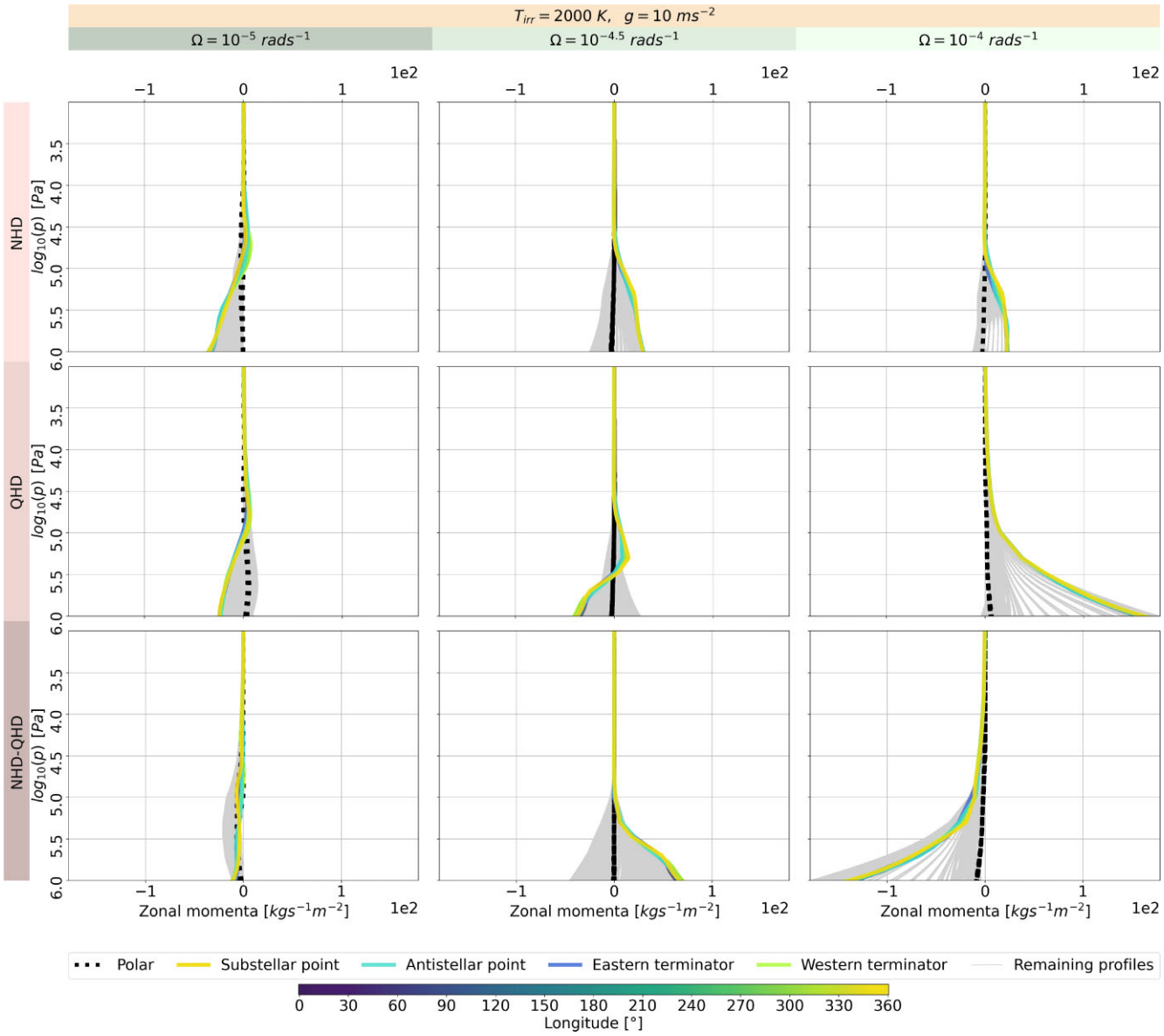

Figure 6. Zonal momenta at each grid point for the NHD and QHD equation sets with $g = 10\,ms^{-2}$, $T_{irr} = 2000\,K$, and with altering Ω. The profiles show only pressures $p \leq 10^6\,Pa$ (without the pressure range $10^6 \geq p \leq 10^8$). The coloured lines indicate momenta profiles along the equator and its coordinates by the colourbar. The dotted black thin line shows momenta profiles at the latitudes 87°N and 87°S. The bold coloured lines represent momenta profiles at the western, eastern terminators, sub-, and antistellar point. The grey lines represents all the other momenta profiles.

Fig. 12 shows the zonal mean wind for the NHD and QHD equation sets with the same $\Omega = 1 \times 10^{-5}\,rad\,s^{-1}$, $T_{irr} = 2000\,K$, and with altering g. The higher g leads to a change from the three-prograde jet system to a one-retrograde jet system. The system and climate state change brings higher wind speeds for the jet along. Furthermore, the wind flows in the deep atmosphere become weaker at higher g.

Fig. 13 shows the zonal momenta [$kg/m^3 m\,s^{-1}$] along vertical profiles at each grid point for NHD and QHD equation set with $\Omega = 1 \times 10^{-5}\,rad\,s^{-1}$, $T_{irr} = 2000\,K$, and with altering g (without the deep atmosphere). The zonal momenta, along the vertical profiles in the simulations with NHD and QHD equation sets, become more similar when the gravity becomes higher. Furthermore, higher gravity leads to a change to an easterly jet (retrograde flow) in both cases. Another effect of higher gravity is the strengthening of the jet at pressures $p < 10^5\,Pa$ in both cases. The jet reaches higher pressure with higher gravity in both cases. The highest momenta are found where the jet is the coldest regardless the gravity. Around the substellar point, the momenta remains still high, but the air masses get decelerated in a zone with a lot of upwelling.

Fig. 14 shows the vertical momenta [$kg/m^3 m\,s^{-1}$] along vertical profiles at each grid point for the NHD and QHD equation sets with $\Omega = 1 \times 10^{-5}\,rad\,s^{-1}$, $T_{irr} = 2000\,K$ and with altering g (without the deep atmosphere). Looking at the effects of increasing gravity, we see a wider range of vertical momenta when the gravity gets higher in both cases at pressures $p < 10^5\,Pa$.

Fig. 15 shows the OLR fluxes at the top of the atmosphere for the NHD and QHD equation set with $\Omega = 1 \times 10^{-5}\,rad\,s^{-1}$, $T_{irr} = 2000\,K$, and with altering g. Looking at the OLR phase curve, the maxima decrease with higher gravity in the NHD and QHD cases,

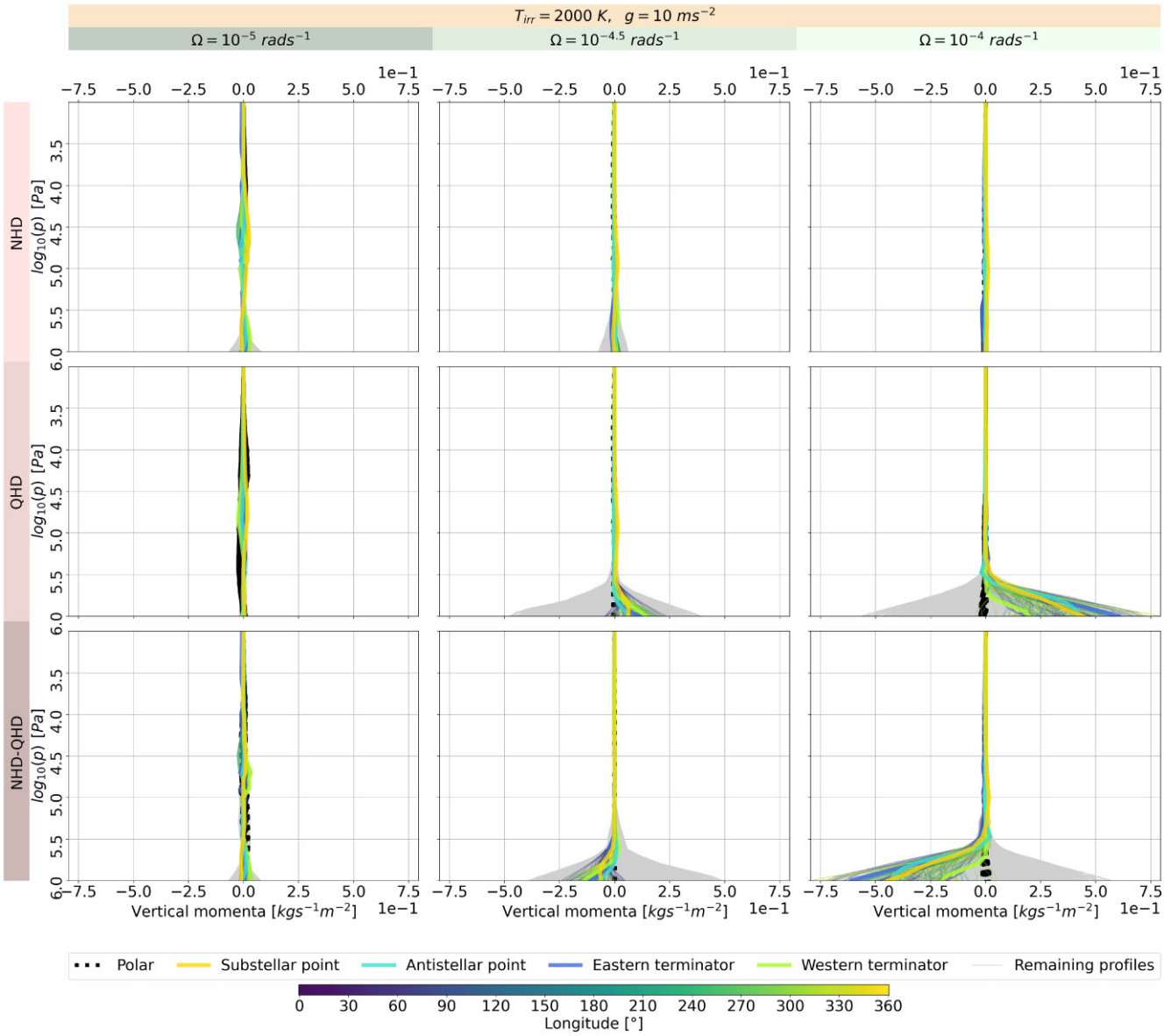

Figure 7. Vertical momenta at each grid point for the NHD and QHD equation sets with $g = 10\,ms^{-2}$, $T_{irr} = 2000\,K$, and with altering Ω. The profiles show only pressures $p \leq 10^6\ Pa$ (without the pressure range $10^6 \geq p \leq 10^8$). The coloured lines indicate momenta profiles along the equator and its coordinates by the colourbar. The dotted black thin line shows momenta profiles at the latitudes 87°N and 87°S. The bold coloured lines represent momenta profiles at the western, eastern terminators, sub-, and antistellar point. The grey lines represent all the other momenta profiles.

although the QHD case stays much higher above the NHD case when gravity is moderate. When gravity gains strength, the minima switches to the western terminator. Furthermore, we see a westward shifted hotspot together with a retrograde flow like in Carone et al. (2020), but the retrograde flow extends to higher latitudes. At both terminators, small wave patterns occur in both cases with moderate and high gravity. When the rotational wind re-enters the daylight zone, the OLR phase curve to rises from the minimum at moderate and high gravity. Moreover, the slope of the OLR phase curves fall less on the upstream side of the maxima in both cases with higher gravity.

Fig. 16 shows the radiative and zonal wind timescales for the NHD and QHD equation sets with $\Omega = 1 \times 10^{-5}\ rad\,s^{-1}$, $T_{irr} = 2000\,K$, and with altering g. The time-scale of the zonal wind shrinks at many heights when the gravity becomes higher. Similarly, the radiative time-scales get shorter when gravity increases.

4.3 Altering irradiation temperature

Fig. 17 shows the T-p profiles for the NHD and QHD equation sets with $\Omega = 1 \times 10^{-5}\ rad\,s^{-1}$, $g = 10\,ms^{-2}$, and with altering T_{irr}. The range of temperatures at pressures $p \leq 10^5\ Pa$ decreases when the irradiation temperature decreases in both cases. Regarding differences between the NHD and QHD cases, they get smaller by a magnitude with each 500 K step in temperature. Furthermore, the temperatures at the poles get the coldest when the irradiation temperatures are equal or less than 1500 K. Inversions start to disappear when the irradiation temperature lowers. The deep atmosphere has cooled down more the lower the irradiation temperature is set.

Fig. 18 shows the temperature and horizontal wind at $10^4\ Pa$ for the NHD and QHD equation sets with $\Omega = 1 \times 10^{-5}\ rad\,s^{-1}$, $g = 10\,ms^{-2}$, and with altering T_{irr}. Lower T_{irr} leads to a change from the three-prograde jet system to a one-prograde jet system. The jet is

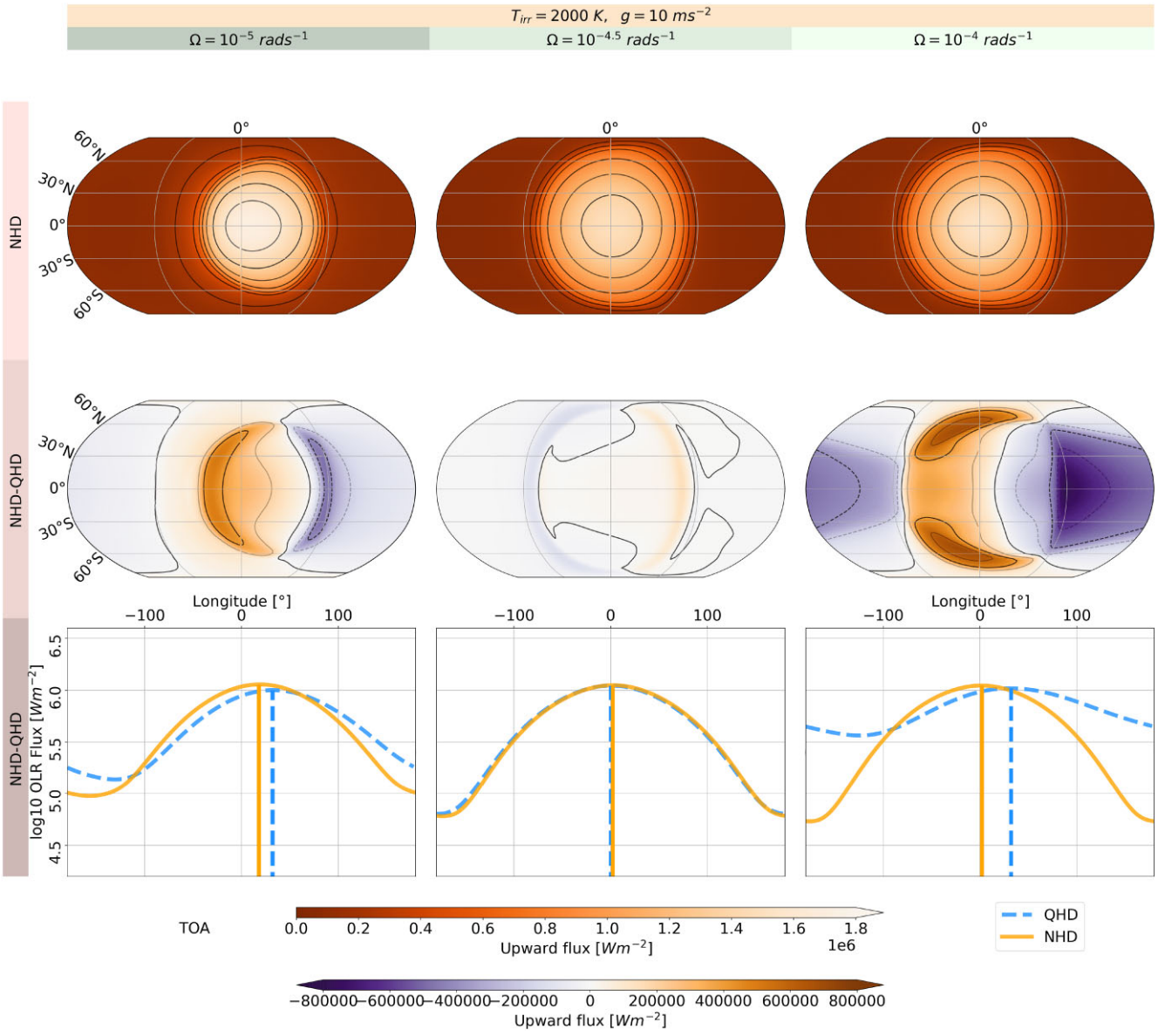

Figure 8. OLR fluxes at the top of the atmosphere for the NHD and QHD equation sets with $g = 10\,ms^{-2}$, $T_{irr} = 2000\,K$, and with altering Ω. Third row: OLR phase curves.

stronger in the one-prograde jet system and ranges from pole to pole. The offset of the hotspot is higher at moderate T_{irr}. But the hotspot starts to vanish at low T_{irr}. The differences become minor at low T_{irr}.

Fig. 19 shows the zonal mean wind for the NHD and QHD equation sets with $\Omega = 1 \times 10^{-5}\,rad\,s^{-1}$, $g = 10\,ms^{-2}$, and with altering T_{irr}. At lower T_{irr}, the jet gets shallower and differences between NHD and QHD case become minor. A peak of jet speeds is reached at $T_{irr} \sim 1500\,K$.

Fig. 20 shows the zonal momenta $[kg/m^3 m\,s^{-1}]$ along vertical profiles at each grid point for the NHD and QHD equation sets with $\Omega = 1 \times 10^{-5}\,rad\,s^{-1}$, $g = 10\,ms^{-2}$, and with altering T_{irr} (without the deep atmosphere). When the irradiation temperature lowers, all zonal wind components become positive at pressures $p \leq 10^5\,Pa$ in the NHD and QHD cases. We see an increase of zonal momenta, when the irradiation temperature decreases from 2000 to 1500 K. Additionally, the divergent component decreases and zonal component becomes stronger if the irradiation temperature lowers (see Helmholtz decomposition in the **supplementary file**). Regarding differences between the NHD and QHD cases, they become a magnitude smaller at each 500 K step in temperature.

Fig. 21 shows the vertical momenta $[kg/m^3 m\,s^{-1}]$ along vertical profiles at each grid point for the NHD and QHD equation sets with $\Omega = 1 \times 10^{-5}\,rad\,s^{-1}$, $g = 10\,ms^{-2}$, and with altering T_{irr} (without the deep atmosphere).

Fig. 22 shows the OLR fluxes at the top of the atmosphere for the NHD and QHD equation sets with $\Omega = 1 \times 10^{-5}\,rad\,s^{-1}$, $g = 10\,ms^{-2}$, and with altering T_{irr}. We see an increasing shift of the OLR to the East when the irradiation temperature is set lower. Similarly, the minima of the OLR phase curve occur around the western terminator in both simulations with lowered irradiation temperature. Furthermore, the differences between NHD and QHD equation sets in the OLR decrease when we set the irradiation temperature lower.

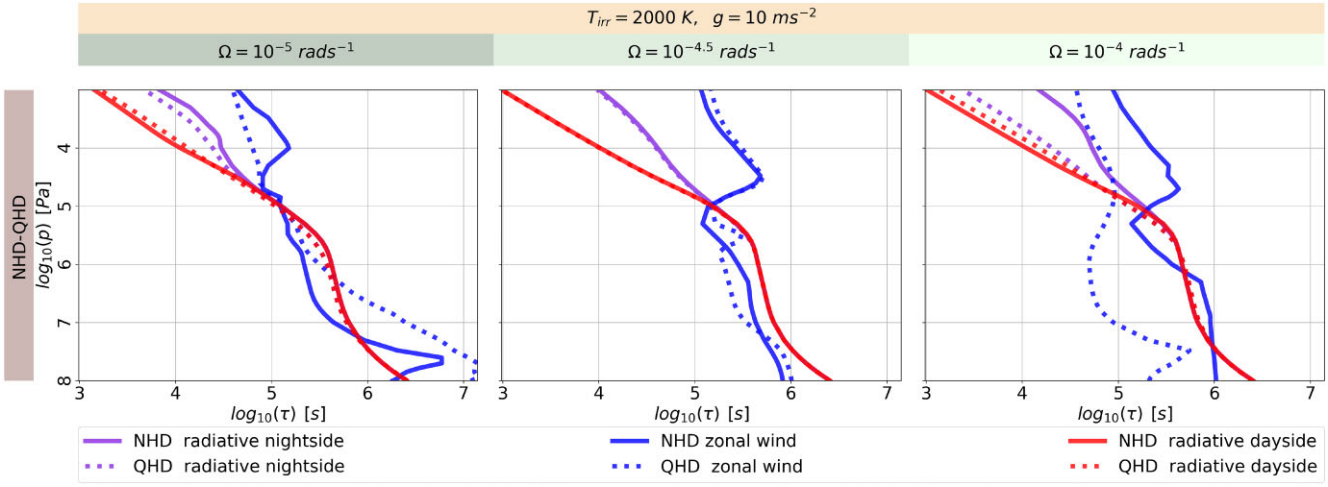

Figure 9. Radiative and zonal wind time-scales for the NHD and QHD equation sets with $g = 10\,ms^{-2}$, $T_{irr} = 2000\,K$, and with altering Ω.

Fig. 23 shows the radiative and zonal wind time-scales for the NHD and QHD equation sets with $\Omega = 1 \times 10^{-5}\,rad\,s^{-1}$, $g = 10\,ms^{-2}$, and with altering T_{irr}. At a irradiation temperature of 1500 K, the time-scale of the zonal wind stays much shorter than the radiative time-scales at pressures $10^{4.5} \leq p \leq 10^{7.5}\,Pa$. We see a more efficient advection by the zonal wind when the divergent component weakens. But the radiative time-scales get shorter than the time-scale of the zonal wind when the irradiation temperature is lowered to $1000\,K$. The zonal wind gets weaker and therefore less efficient of advection.

5 DISCUSSION

The difference between the NHD and QHD equation sets in THOR lies in the Dv_r/Dt, the Lagrangian derivative of the vertical velocity, $\mathcal{F}_r$, the hyperdiffusive flux, and $\mathcal{A}_r$, the vertical component of the advection terms. These terms lead to deviations in the vertical momenta in the simulations with QHD. The altered vertical momenta affects the horizontal momenta and the temperature structure indirectly. Those changes caused by a different dynamical equations set even lead to different climate states in the simulated time period.

As first approach, we can compare to the analytic solutions of Showman & Polvani (2011), which applied the linearized shallow water equations. They designed the equation set to be the simplest as possible to cleanly identify specific dynamical processes; therefore, a two-layer model was implemented. Those analytic solutions were calculated with the zonal wavenumber $k = 0.5$ and a rotation period of 3 Earth days. The rotation periods in our study are 7.27, 2.3, and 0.73 Earth days. Therefore, all analytic solutions lie between our simulations with $\Omega = 1 \times 10^{-5}\,rad/s$ and $\Omega = 1 \times 10^{-4.5}\,rad/s$. The closest parametrization between our results and those analytic solutions is $\tau_{rad} = 1\,d$ and $\tau_{drag} = 1\,d$, which corresponds to the top left plot of fig. 3 of Showman & Polvani (2011). In our simulations, the radiative time-scales reach values between $\tau_{rad} \sim 0.12\,d$ for dayside and $\tau_{rad} \sim 1.11\,d$ at the height of the jet. Furthermore, τ_{diff} becomes $1.69 \times 10^{-4}\,d$ when $D_{hyp,\,h} = 0.0025$ is used in the following equation [according to Hammond & Abbot (2022)]

$$\tau_{diff} \sim \frac{\Delta t}{2^{2n+1} D_{hyp,h}}. \tag{22}$$

Rossby-wave gyres do not appear in the analytic solutions (Showman & Polvani 2011) with $\tau_{rad} = 1\,d$ and $\tau_{drag} = 1d$. When τ_{rad} and τ_{drag} become higher, cyclones and anticyclones become visible in the analytic solutions. In our results, we do see Rossby-wave gyres pumping zonal momenta from higher latitudes to lower latitudes, when gravity or the rotation rate gets more intense (e.g. see figure with high g and high Ω in the **supplementary file** and Fig. 11). However, τ_{rad} is smaller in our composites with altering Ω than in the analytic solutions of the linearized shallow-water equations. The equilibrated solutions in Showman & Polvani (2011) lead to a single maxima and minima of the geopotential gh for $\tau_{rad} = \tau_{drag} = 0.1\,d$. When gh for τ_{rad} or τ_{drag} become higher, 2 minima and 2 maxima evolve. In our results, we see 1 maxima and a chevron respectively 2 minima. That pattern evolves likely due to the different τ_{rad} on the day- and nightside compared to the uniform time-scales in Komacek, Showman & Parmentier (2019). Komacek et al. (2019) did run 36 experiments with a comparable setting ($c_P = 13\,000\,Jkg^{-1}K^{-1}$, $R = 3700\,Jkg^{-1}K^{-1}$, $a = 9.437 \times 10^7\,m$, $g = 9.36ms^{-2}$, and $\Omega = 2.078 \times 10^{-5}\,s^{-1}$). They show the vertical and horizontal wind for different τ_{drag} and T_{eq} at $10^2\,Pa$. Their simulations with $\tau_{drag} \leq 10^6\,s$ led to no superrotating jet and a more divergent flow, whereas simulations with $\tau_{drag} \geq 10^6\,s$ show a superrotating jet. Our comparable simulation with $g = 10ms^{-2}$, $\Omega = 1 \times 10^{-5}\,rad\,s^{-1}$, and $T_{irr} = 2000\,K$ falls with $\tau_{diff} = 1.69 \times 10^{-4}\,d$ below the threshold of $\tau_{drag} \leq 10^6\,s$ and produces a similar horizontal and vertical flow pattern, although we see the similarity at $10^4\,Pa$ instead of at $10^2\,Pa$. The differences to Komacek et al. (2019) probably occur because of different dynamical cores (dynamical equation sets) and spatially different radiative time-scales.

5.1 Examination of climate states

We classify the NHD simulation outputs into climate states according to jet behaviours and manifestations of the components of the Helmholtz decomposition. The stated climate states are presented hereafter and illustrated in Fig. 24. We consider this classification as a first assumption to figure out parameters where the QHD case (and maybe GCMs with HPEs) perform not as accurately. So, it should not be seen as a definitive classification scheme.

Moreover, we computed large-scale flow quantities and other characteristic values and scales in Table 2. We discuss those indicators in relation to the climate states in the next section.

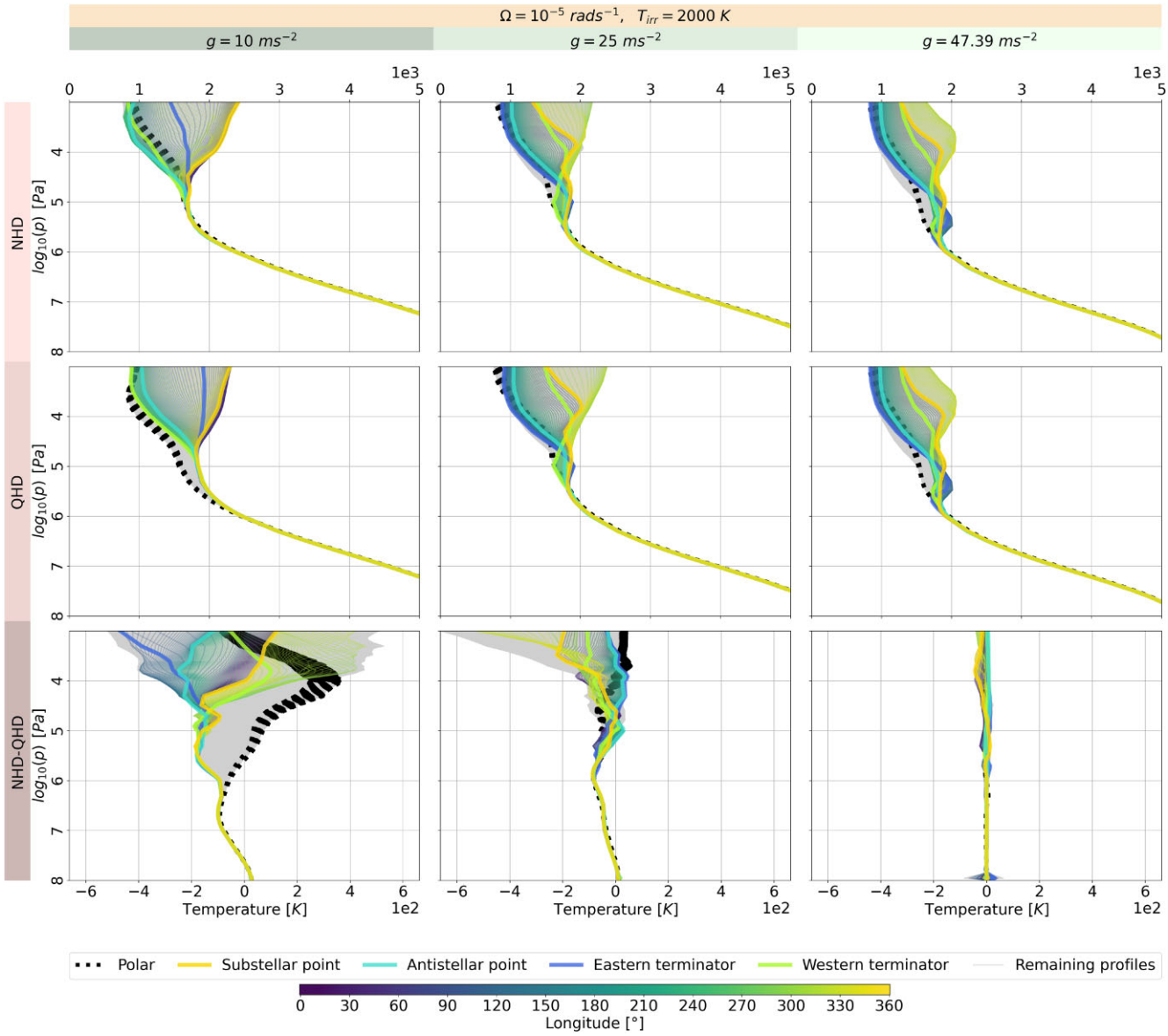

Figure 10. T-p profiles of covering entire planet for NHD and QHD equation sets with the same $\Omega = 1 \times 10^{-5}\ rad\,s^{-1}$, $T_{irr} = 2000\,K$ and with altering g. The coloured lines indicate T-p profiles along the equator and its coordinates by the colourbar. The dotted black thin line shows T-p profiles at the latitudes 87°N and 87°S. The bold coloured lines represent T-p profiles at the western, eastern terminators, sub- and antistellar point. The grey lines represents all the other T-p profiles.

5.1.1 Three prograde jets

When we alter the planetary rotation rate Ω at irradiation temperatures $T_{irr} = 2000\,K$ and gravity $g = 10\,ms^{-2}$, we see a transition from a climate state with a dominate divergent component to a climate state with higher Coriolis forces. A dominate large 'extra-tropical' zone expands near to the equator with higher rotation rates (Parmentier 2014). In that zone, the advection term becomes small or even negligible and the force balance is mainly made up among the Coriolis term and the pressure gradient. The Rossby number *Ro* for $\Omega = 10^{-4.5}$ and $\Omega = 10^{-4}\ rads^{-1}$ are in the range of 0.031–1.39, respectively, in the range of 0.0098–0.44. For the maximum horizontal wind speeds in our simulations, we get $Ro = 0.19$ and $Ro = 0.15$ for the NHD and QHD case for $\Omega = 10^{-4.5}\ rads^{-1}$. For $\Omega = 10^{-4}\ rads^{-1}$, we get $Ro = 0.052$ and $Ro = 0.14$ for the NHD and QHD case for the horizontal winds in our simulations. The too high wind speed in the simulation with the QHD equation set prevents the Coriolis force to act on the jet structures at $\Omega = 10^{-4}\ rads^{-1}$. At $\Omega = 10^{-4.5}\ rads^{-1}$, the horizontal wind in QHD case is more moderate than at lower Ω and therefore the balancing regarding the Coriolis force is more similar to the NHD case.

Looking at the Helmholtz decomposition at $10^4\ Pa$, all components are weaker than at lower rotation rates (see the plots of the Helmholtz decomposition in the **supplementary file**). The divergent component is still dominant compared to simulations with higher g or lower T_{irr}. The rotational eddy and rotational jet components evolved moderate weakly.

The scale height H and the Brunt–Väisälä frequency are 525.24 km and $N = 0.00816\ s^{-1}$ for the three altered Ω at $T_{\rm irr} = 2000\,K$ and $g = 10\,ms^{-2}$. The Rossby deformation radius $L_{\rm D}$ are 1.32 and 0.42 $R_{\rm p}$ for $\Omega = 10^{-4.5}$ and $\Omega = 10^{-4}\ rads^{-1}$. So, we expect smaller eddy sizes at higher Ω. The Rhines scales L_{RH} vary between 0.46 and 3.11 $R_{\rm p}$. For

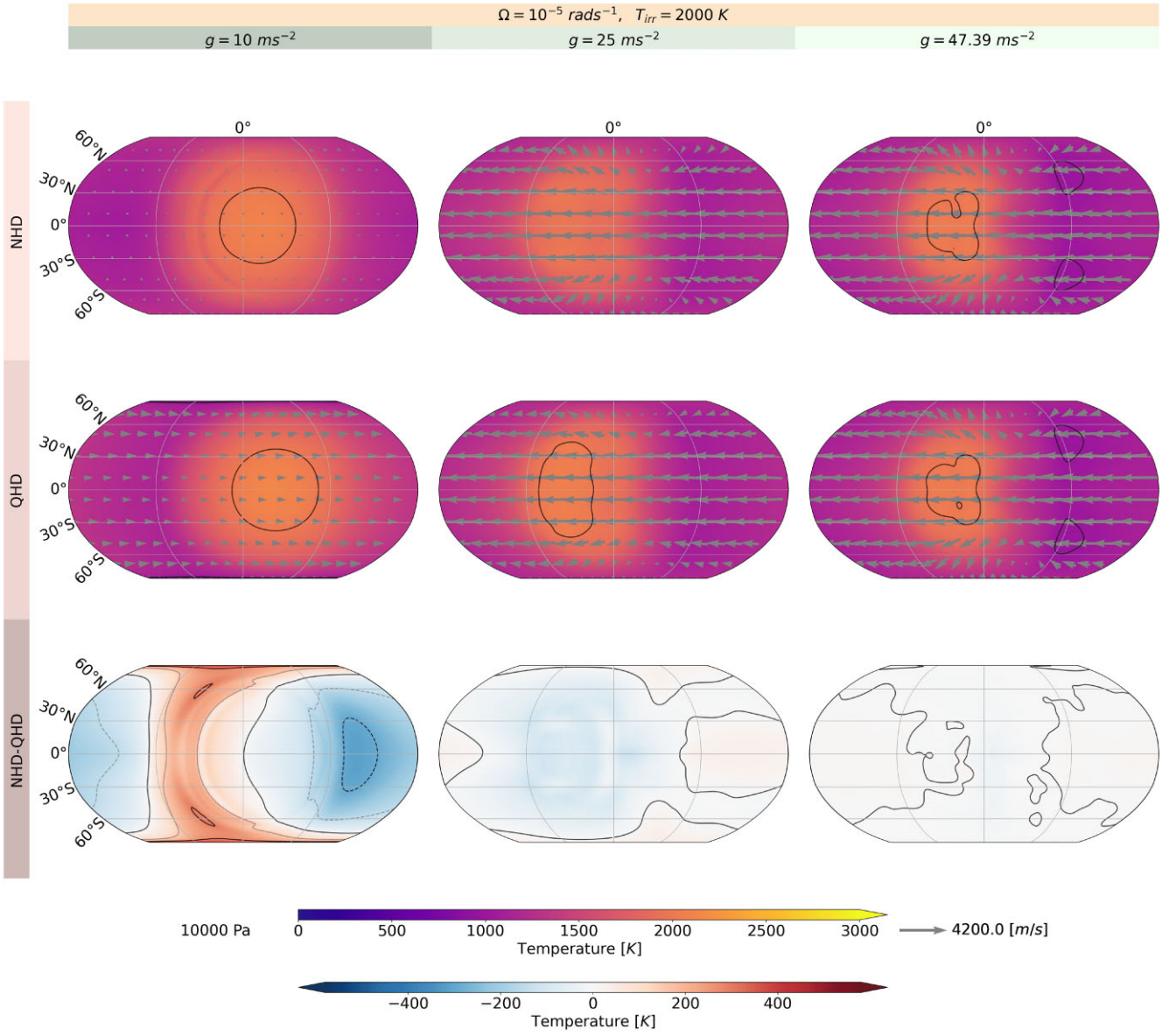

Figure 11. Temperature and wind speed at 10^4 *Pa* for the NHD and QHD equation sets with $\Omega = 1 \times 10^{-5}$ $rad\,s^{-1}$, $T_{irr} = 2000\,K$, and with altering g.

our maximum wind speeds in our simulations, $L_{\rm RH}$ becomes 1.14, respectively, $0.06\,R_{\rm p}$, for $\Omega = 10^{-4.5}$ and $\Omega = 10^{-4}$ $rads^{-1}$. Such small scales let small-scale vortices boost the larger atmospheric flow with their energies (Parmentier 2014). The values for $L_{\rm RH}$ increase with higher latitude and the likelihood for the appearance of Rossby waves. At higher latitudes, we do see planetary waves at 10^4 *Pa*.

The NHD case shows the emergence of high-latitude prograde jets in addition to the deeper, prograde, and primary superrotating equatorial jet. Showman et al. (2009) and Rauscher & Kempton (2014) observed the three jet structure in their GCM simulations as well but for both HD 189733b and HD 209458b, respectively, with non-synchronous rotation rates.

We see differences in our simulations between the NHD and QHD equation sets growing with increased rotation rate. Wind speeds and momenta in the QHD simulations underlay those in the NHD simulations at slow rotation. But the zonal momenta in the QHD case exceed by about five times those in the NHD case at high rotation rates. The differences in the momenta lead to significant differences in the advection and the temperature structure at pressures $p \leq 10^6$ *Pa* at slow and high rotation rates. The differences in the temperature range grow from about 600 *K* at the slow rotation to 1200 *K* at fast rotation rate. The difference between the NHD and QHD equation sets do not behave linearly and include dynamical regime and climate changes in the QHD case. We see even very similar regimes and climates at moderate rotation rate at pressures $p \leq 10^4$ *Pa*, but the dynamical equations lead to totally different regimes in the deep atmosphere. We noticed two dynamical regime and climate state changes by altering the rotation rate in the QHD case at pressures $p \leq 10^4$ *Pa*. The QHD case changes from a two-jet system with superrotation to a three-jet system with weak extra-tropical conditions and then back to the state with two jets and superrotation when we alter the rotation rate. There might further dynamical regime changes and multiple stable climate states at different parameters that we did not simulate. Considering deeper atmosphere layers with pressures $p > 10^5$ *Pa*, the range of the zonal momenta is lower in the QHD case than the NHD case

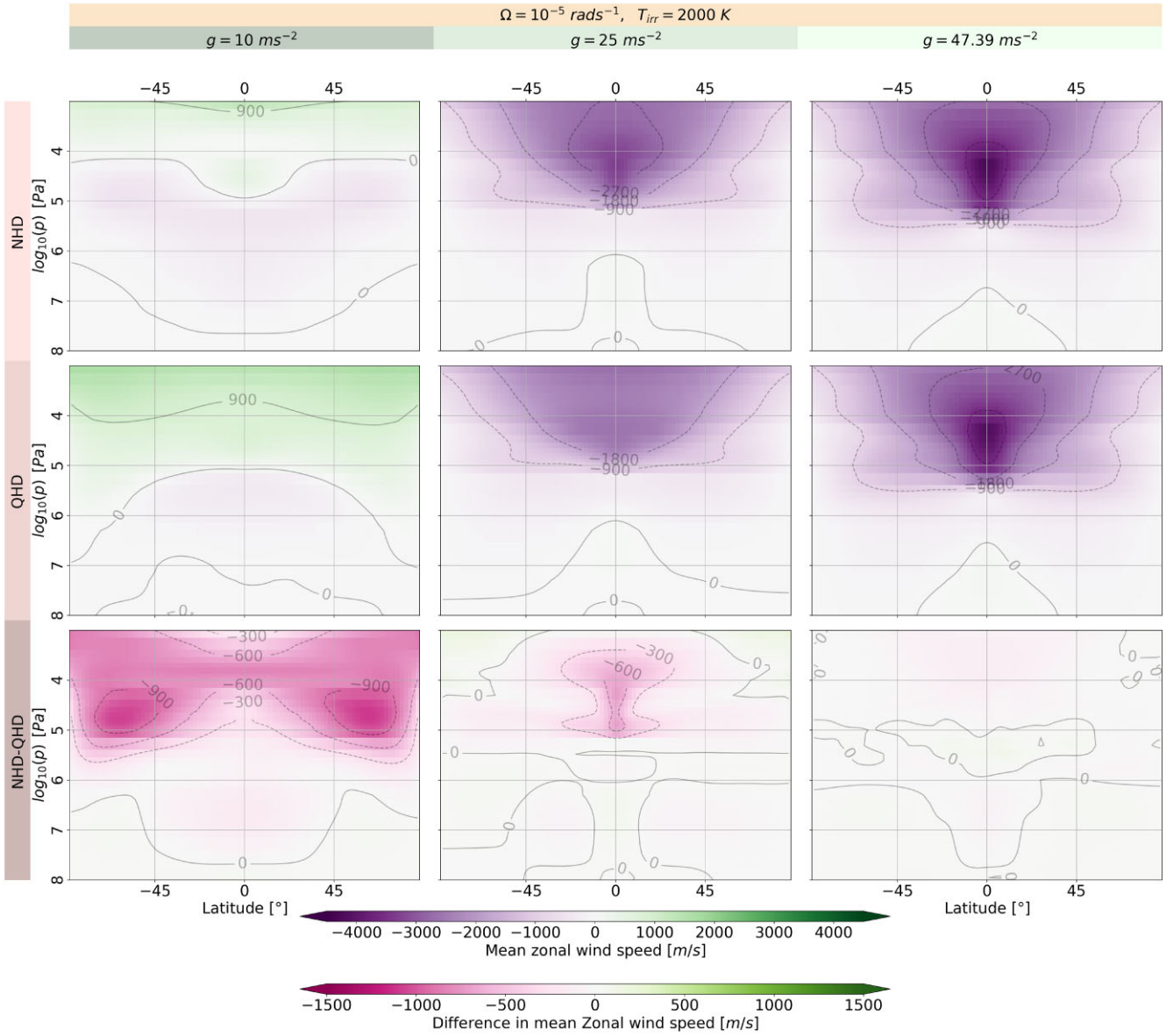

Figure 12. Zonal mean wind for the NHD and QHD equation sets with $\Omega = 1 \times 10^{-5}\ rad\,s^{-1}$, $T_{irr} = 2000\,K$, and with altering g.

at low rotation rate but larger at high rotation rate. Furthermore, we see a slow down of overturning circulation in the standard and tidally locked coordinates with increasing Ω (see the plots of the overturning circulation in the **supplementary file**). The overturning circulations of NHD cases differs quantitatively and qualitatively from circulations in the QHD case.

In the QHD case, the terms $\frac{Dv_r}{Dt}$, $\mathcal{F}_r = 0$, and $\mathcal{A}_r$ lead to different vertical and indirectly to higher horizontal momenta. Therefore, the QHD case implies that GCMs with HPEs simulate too high zonal velocities at these parametrizations. The higher zonal wind speeds encounter the Coriolis forces. We expect a range of critical wind speed at a given rotation rate at which the climate switches to another climate state when the extra-tropical zone is relatively large. Higher wind speeds in combination with the smaller Rossby deformation radius L_D, moderate Coriolis forces may cause totally different climate states at certain parameters. Consequently, the models show different shifts of hotspot in simulations with different hydrodynamic equation sets depending on the parameters.

The faster rotation rates also cause deviations with other approximations; as Tort et al. (2015) has already proved for terrestrial regimes, the traditional approximation gets increasingly less valid, when the rotation becomes faster. Regarding another Coriolis term, $-2\Omega\omega\cos\phi$ can be neglected if $2\Omega H\cos(\phi)U^{-1} \ll 1$, as White & Bromley (1995) showed. For our simulation at low g and at $\Omega = 10^{-4}\ rads^{-1}$, $2\Omega H\cos(\phi)U^{-1}$ is about 0.21 and 0.11 for a wind speed of $500\,m^{-1}$ at the equator, respectively, for the mid-latitudes. Therefore, the term $-2\Omega\omega\cos\phi$ gets more relevant in this climate state with extra-tropical conditions and GCMs with the traditional approximation in their dynamical equation sets may predict incorrectly. Mayne et al. (2019) has shown that increased rotation rate leads to significant differences in the flow and the flow becomes dominated by the Coriolis forces. Furthermore, a higher rotation rate result in a net warming on the dayside and a net cooling on the nighside in their simulation although the more complete equations manifest less those warming and cooling effects. At higher pressures, they noticed only temperature changes by a

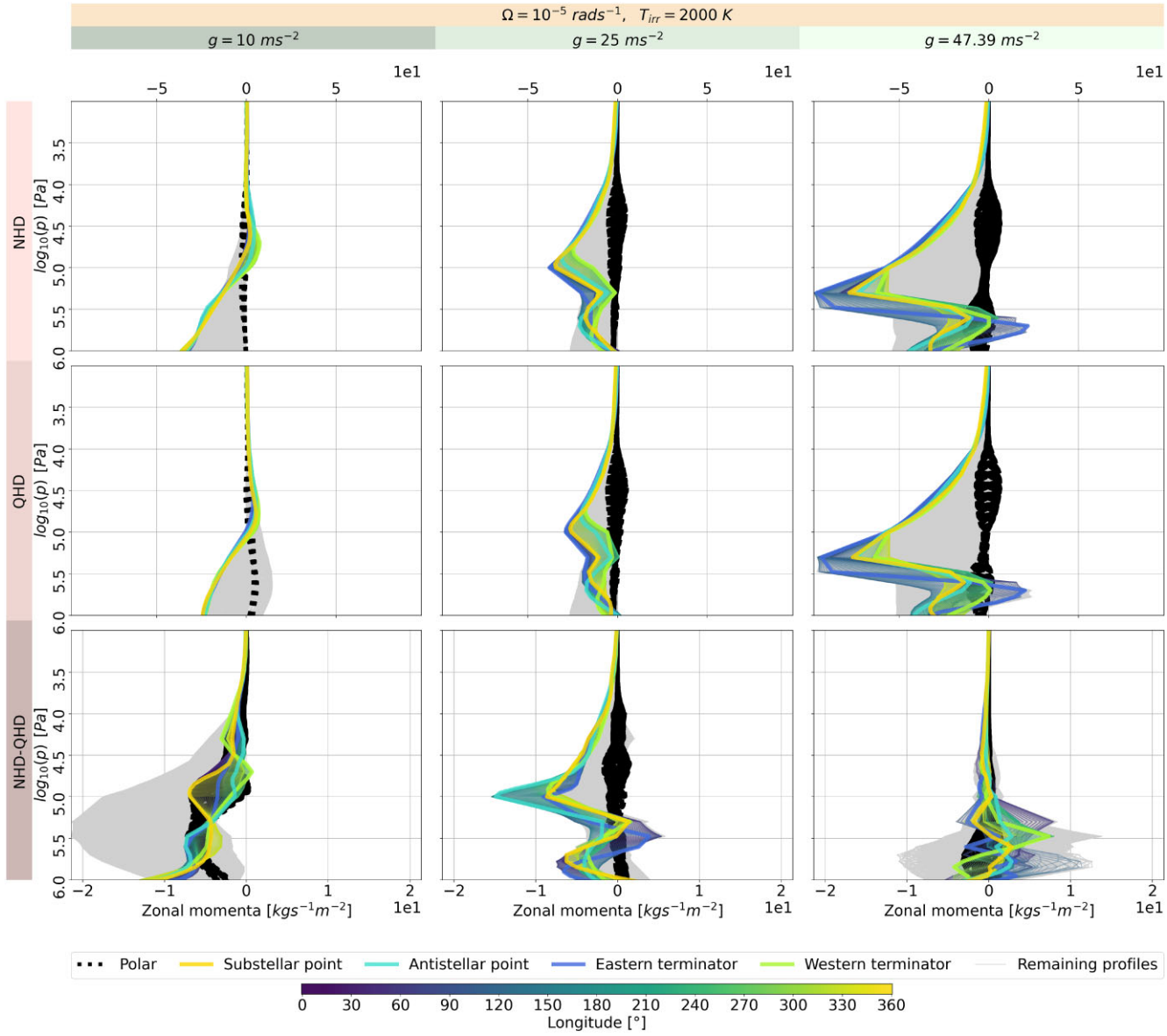

Figure 13. Zonal momenta at each grid point for NHD and QHD equation set with $\Omega = 1 \times 10^{-5}\, rad\, s^{-1}$, $T_{irr} = 2000\, K$, and with altering g. The profiles show only pressures $p \leq 10^6\, Pa$ (without the pressure range $10^6 \geq p \leq 10^8$). The coloured lines indicate momenta profiles along the equator and its coordinates by the colourbar. The dotted black thin line shows momenta profiles at the latitudes 87°N and 87°S. The bold coloured lines represent momenta profiles at the western, eastern terminators, sub-, and antistellar point. The grey lines represents all the other momenta profiles.

few degrees. Mayne et al. (2019) suggested to analyse and compare different dynamical equation sets with a full RT solution, as used in Amundsen et al. (2016). Similarly, as in Mayne et al. (2019), we see a net warming on the dayside and a net cooling on the nightside at pressures $p \leq 10^5\, Pa$. But in the deep atmosphere, temperatures start to vary increasingly by increased rotation rates in our simulations. That difference among both studies in the deep atmosphere may arise from different type of planet: hot, fast rotating Jupiters may respond differently than on slowly rotating and warm Neptunes. Furthermore, we simulated a much larger fraction of the deep atmosphere than Mayne et al. (2019). Regarding the RT, we expect effects on the dynamics and temperature structure due to different RT implementations. Additionally, we expect some differences in the GCM implementations that lead to varying results when comparing to other studies.

5.1.2 *Radial flow*

This idealized climate state has a radial and divergent flow on the dayside as well as a convergent flow on the nightside in the upper atmosphere, analogous to a global Hadley or Walker cell. Vica versa for some deeper layers. The Helmholtz decomposition would show a dominant divergent component. That climate state is an idealized and needs higher ratio of T_{irr} to Ω, which is likely unrealistic compared to the observed exoplanets so far. At lower rotation rates Ω, at $T_{irr} = 2000\, K$ and $g = 10\, ms^{-2}$, we see a transition to a climate state with a dominant divergent component, a moderate weak rotational eddy component and weak rotational jet component (see the plots of the Helmholtz decomposition in the **supplementary file** and Fig. 24). The three-jet system is still present in this transitional phase. As the Coriolis forces get weaker, winds get less deflected and can flow more direct from the dayside to the nightside. We see wind flows deflected

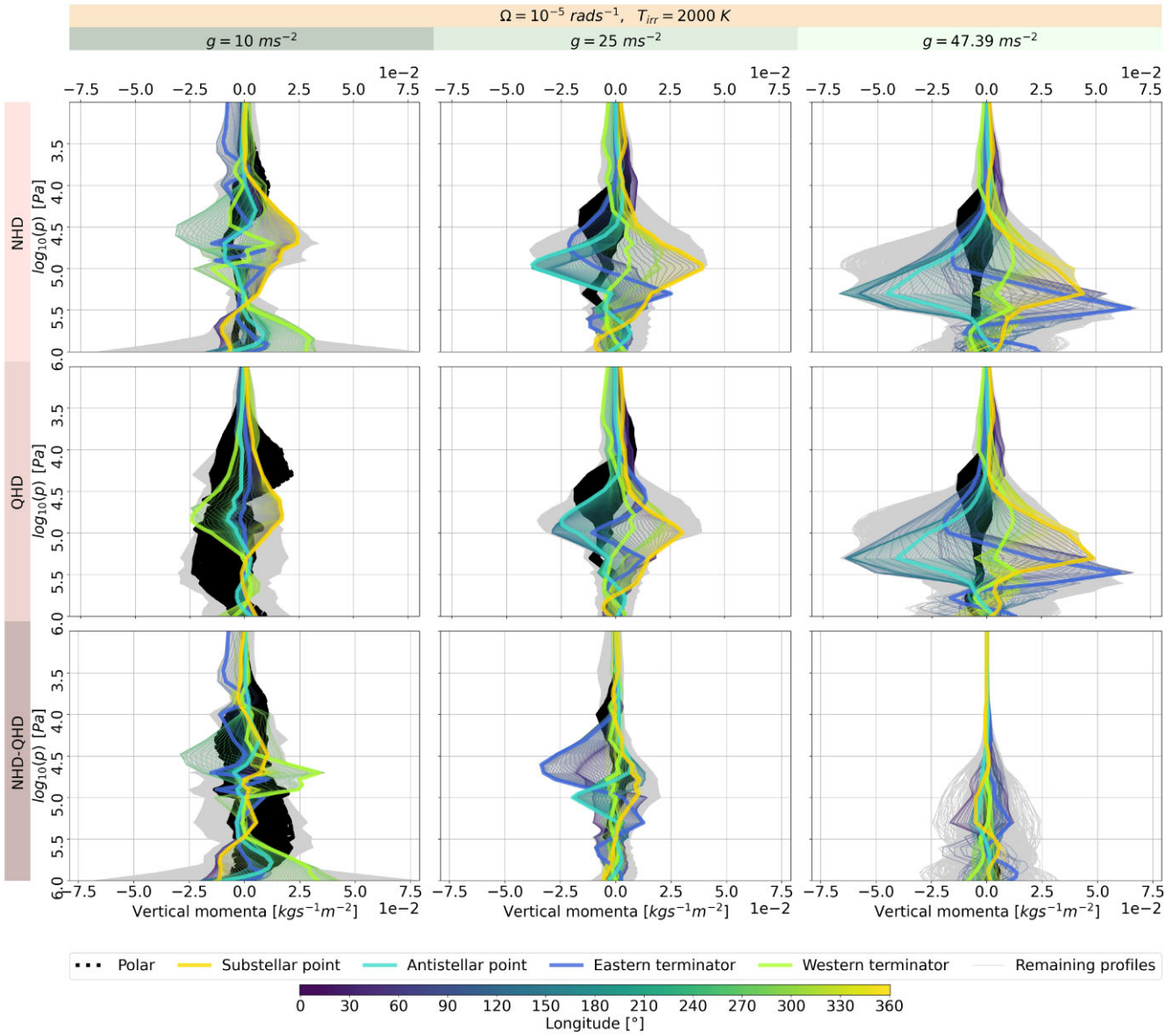

Figure 14. Vertical momenta at each grid point for NHD and QHD equation sets with $\Omega = 1 \times 10^{-5}$ $rad\,s^{-1}$, $T_{irr} = 2000\,K$ and with altering g. The profiles show only pressures $p \leq 10^6$ Pa (without the pressure range $10^6 \geq p \leq 10^8$). The coloured lines indicate momenta profiles along the equator and its coordinates by the colourbar. The dotted black thin line shows momenta profiles at the latitudes 87°N and 87°S. The bold coloured lines represent momenta profiles at the western, eastern terminators, sub-, and antistellar point. The grey lines represents all the other momenta profiles.

less and crossing more directly over the poles to the nightside (e.g. at $10^4 Pa$). There are certainly more simulations in this parameter space needed to characterize that area in the parameter grid. The circulation state may change at lower Ω. It cannot excluded if there is a retrograde superjet at lower Ω and if radial flow is evolved due to a balance between prograde and retrograde tendencies (similar to the simulations with higher g). A similar radial flow pattern was found by Carone et al. (2018) for tidally locked ExoEarths (TRAPPIST 1b, TRAPPIST 1d, Proxima Centauri b, and GJ 667 C f) at relatively low Ω.

The gradual transition to the climate state is seen at $T_{eq} = 1414.21\,K$ and $H = 525.24\,km$. The Rossby number Ro varies between 0.098 and 4.39 from winds of 100–4500 ms^{-1}. The Rossby deformation radius and Rhines scale are 4.19 and 0.83–5.54. The Brunt–Väisälä frequency remains the same as at higher Ω, $N = 0.00816\,s^{-1}$.

5.1.3 *Prograde superrotation*

This circulation and climate state occurs on the one side at high g and high T_{irr}, on the other side at low and high g, at relatively high T_{int} compared to the $T_{\rm irr}$.

The $T_{\rm int}$ lies above the value computed according to the expression in Thorngren et al. (2019), 300 and 400 K, respectively. The high $T_{\rm int}$ is debatable; high $T_{\rm int}$ might be the reality as strong magnetic fields have been detected by (Yadav & Thorngren 2017; Cauley et al. 2019). The magnetic field strength determines the T_{int} substantially (Christensen, Holzwarth & Reiners 2009). Thorngren et al. (2019) excluded $T_{\rm int} = 100\,K$ for planets with clouds because of the cold trap, especially for $Teq \sim$ 1100–1600 K (Lines et al. 2018a). Nevertheless, higher $T_{\rm int}$ can be realistic because of a significant higher entropy, which causes a higher internal heat flux (Thorngren et al. 2019). Regarding the cooling rate of hot (ultra)

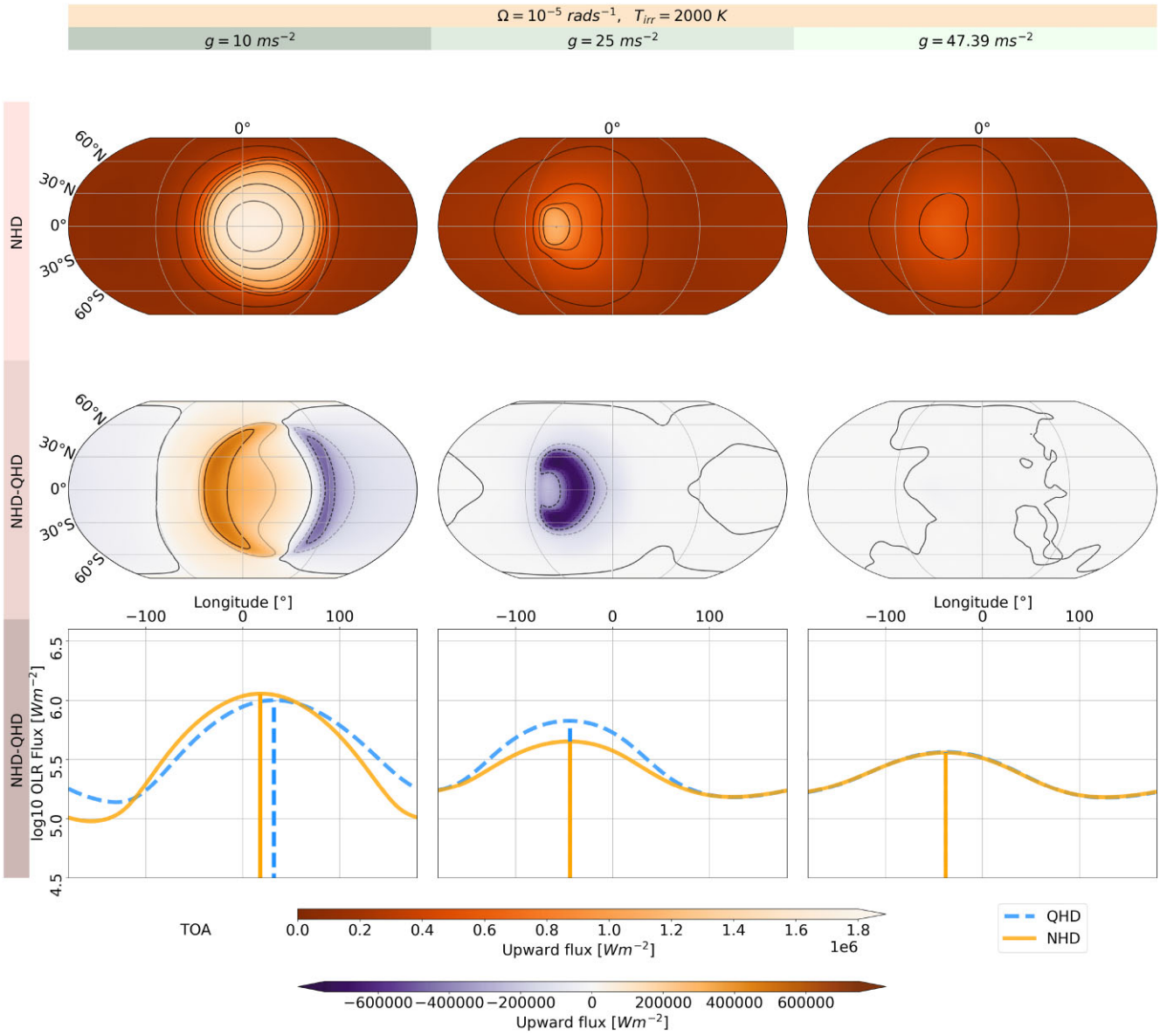

Figure 15. OLR fluxes at the top of the atmosphere for NHD and QHD equation sets with $\Omega = 1 \times 10^{-5}\ rad\,s^{-1}$, $T_{irr} = 2000\,K$, and with altering g. Third row: OLR phase curves.

Jupiters, Showman & Guillot (2002), Guillot & Showman (2002), Youdin & Mitchell (2010), and Tremblin et al. (2017) predicted a downward heat transport by the atmosphere. As a theoretical proof, Mendonça (2020) found heat transport from the upper into the deeper atmosphere by the atmospheric circulation. Similarly, Komacek et al. (2022) saw the coupling of internal evolution and atmospheric structure with the atmospheric dynamics in their simulations.

The Rossby number Ro lies between 0.098 and 4.39. For the maximum wind speeds in our simulation, we get $Ro < 1.18$. The climate state have Rossby deformation radii $L_D \leq 3.63\,R_p$. The Rhines scales L_{RH} vary between 0.83 and 5.54 R_p and are smaller than 2.9 R_p for the maximum wind speeds in our simulation. The Brunt–Väisälä frequency is $N > 0.01\,s^{-1}$. The scale height is $H = 55.42\,km$ for $g = 47.39\,ms^{-2}$, and $H \leq 393.93\,km$ for $g = 10\,ms^{-2}$.

Differences between simulations outputs from NHD and QHD equation sets are quantitatively relatively small and negligible at $T_{\rm irr} = 1500\,K$ and $g = 47.39\,ms^{-2}$, respectively $g = 10\,ms^{-2}$. Qualitatively, the differences are more pronounced in the circulation pattern at $10^4\,Pa$. In this transitional phase, the QHD performs not so well compared to clear distinguishable circulation and climate states.

A dominant rotational jet component, a dominant rotational eddy component, and a weaker divergent component characterize that climate state (see the plots of the Helmholtz decomposition in the **supplementary file**). Comparable simulations were computed by Kataria et al. (2015) and Schneider et al. (2022) for WASP 43b with the HPEs, although our parametrization differs by slightly higher $T_{\rm irr}$ and slightly higher Ω. Our results with the parametrization $\Omega = 10^{-4}\,rad\,s^{-1}$, $T_{\rm irr} = 2000\,K$, and $g = 47.39\,ms^{-2}$ partially agree to those of Kataria et al. (2015) and Schneider et al. (2022). We see a prograde jet and Rossby gyres that transport zonal momenta to low latitudes as well as retrograde flow at high latitudes like in their study (e.g. see figure with simulation computed with $g = 47.39\,ms^{-2}$ $T_{\rm irr} = 2000\,K$ and altering Ω in the **supplementary file**). But the speed of

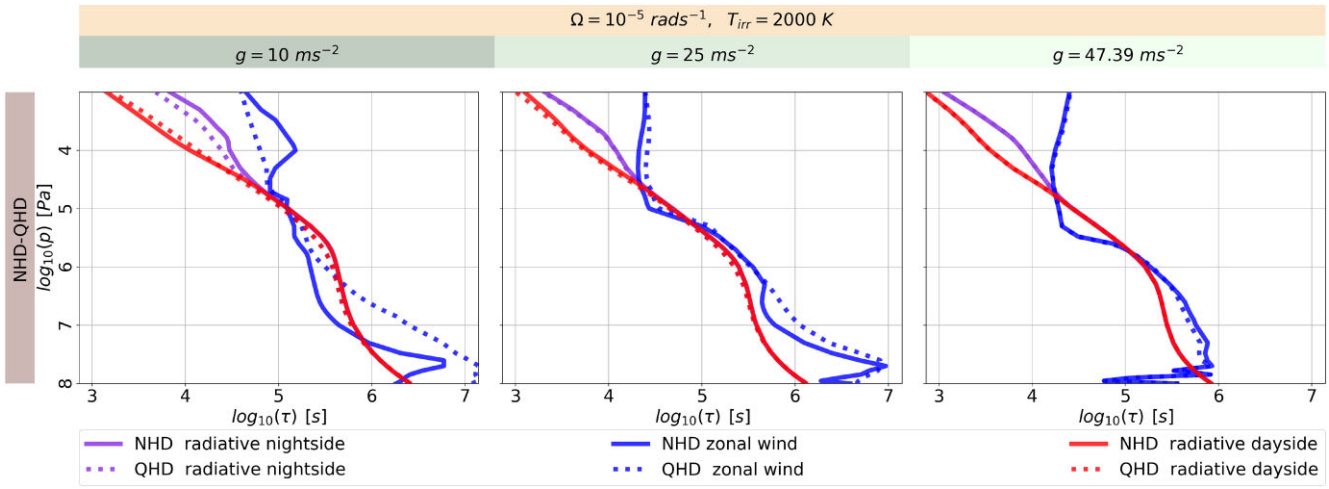

Figure 16. Radiative and zonal wind timescales for the NHD and QHD equation sets with $\Omega = 1 \times 10^{-5}$ $rad\,s^{-1}$, $T_{irr} = 2000\,K$, and with altering g.

the jet remains with $\sim$1800 ms^{-1} for the NHD and QHD case much lower than the wind speeds of 5500 ms^{-1} in studies of Kataria et al. (2015) and Schneider et al. (2022). At this parametrization, it seems the HPEs predict too high wind speeds compared to the NHD and QHD equation sets. The differences between the NHD and QHD case are less than 100 K and minor compared to the low gravity.

5.1.4 Retrograde superjet

In this circulation and climate state, a retrograde superjet leads to a westward offset of the hotspot. This climate states occurs at high gravity and low rotation rate ($T_{irr} = 2000\,K$, $\Omega = 10^{-5}$ $rad\,s^{-1}$, $g = 25\,ms^{-2}$, and $g = 47.39\,ms^{-2}$, respectively; see Fig. 24). This climate state has a dominant rotational jet component, a weak divergent component, and a weak rotational eddy component (see the plots of the Helmholtz decomposition in the **supplementary file**). We see a transition from retrograde to prograde superrotation in the simulations with $T_{\rm irr} = 2000\,K$, $\Omega = 10^{-4.5}$ $rad\,s^{-1}$, and $g = 47.39\,ms^{-2}$, respectively partially in the simulation with $T_{\rm irr} = 1500\,K$, $\Omega = 10^{-5}$ $rad\,s^{-1}$, and $g = 47.39\,ms^{-2}$ (see Fig. 24).

The equilibrium temperature lies around $T_{\rm eq} = 1414.21\,K$. The scale height is 110.83 and 210.1 km, respectively. The Rossby number is around 0.098–4.39. The high winds in our simulations imply encountered Coriolis forces, partially tropical conditions. The Rossby deformation radius is 4.19, while the Rhines scales varies in a range of 0.83–5.54.

Differences between simulations outputs from NHD and QHD equation sets are less than 200 and less than 100 K at $T_{\rm irr} = 2000\,K$, $\Omega = 10^{-5}$ $rad\,s^{-1}$, $g = 25\,ms^{-2}$ and $g = 47.39\,ms^{-2}$, respectively, for pressures larger than 10^4 Pa. The smaller temperature differences come along with a stronger retrograde superjet.

5.2 Implication for the superrotation

We see a complete shift in the climate regime in our simulations towards a retrograde jet spreading to high latitudes at pressures $p \leq 10^{5.5}$ Pa and at low Ω when gravity increases. Many studies [e.g. Showman & Guillot (2002); Showman et al. (2009); Dobbs-Dixon et al. (2010); Tsai, Dobbs-Dixon & Gu (2014); Kataria et al. (2015); Amundsen et al. (2016); Zhang & Showman (2017); Mendonça et al. (2018b)] have shown that tidally locked hot Jupiters produce an equatorial eastward wind jet in 3D simulations. The equatorial eastward jet transports heat to the nightside and shifts the hotspot to the east (Knutson et al. 2007). Nevertheless, there are several exceptions among hot Jupiters; Dang et al. (2018) observed a westward shifted hotspot in CoRoT 2b. Similarly, May et al. (2022) made observations of a westward shift for WASP 140b. Several factors can counter superrotation (Carone et al. 2020), clouds (Helling et al. 2016; Parmentier et al. 2016; Mendonça et al. 2018b), including variability in the cloud coverage Armstrong et al. (2016), Dang et al. (2018, possible for CoRoT 2b and HAT P7b), higher metallicity in the planet's atmosphere (Kataria et al. 2015; Drummond et al. 2018a), and magnetic fields (Rogers & Komacek 2014; Kataria et al. 2015; Arcangeli et al. 2019; Hindle, Bushby & Rogers 2019) may affect the circulation significantly. Moreover, planets may evolve retrograde flow because of non-synchronous planetary rotation (Rauscher & Kempton 2014). We suggest that the choice of the dynamical equation set may counter superrotation as well as lead to different jet systems and climate states. Furthermore, we assume additional physical schemes may alter the balances for the evolution of jet systems and climate states.

Many of the previous studies used simplified Newtonian cooling or grey RT solutions; (Lee et al. 2021) showed the improvements for more realistic RT solution We consider more realistic RT solution in GCMs and other schemes, in addition to the dynamical cores as a key consideration, when investigating differences between dynamical equation sets. WASP 43b orbits its host star with 0.8315 d relatively quickly (Hellier et al. 2011) and is unusually dense. Carone et al. (2020) simulated WASP 43b and got varying results compared to Kataria et al. (2015), Mendonça et al. (2018b), and Schneider et al. (2022); The simulations of WASP 43b in Carone et al. (2020) show westward (retrograde) flow in the upper thermal photosphere ($p \leq 8000\,Pa$) as soon as the model simulates deep wind jets. They found a strong tendency of an equatorial westward flow in the eddy-mean-flow analysis for $p < 10^4$ Pa for WASP 43b. Carone et al. (2020) concluded that the deep atmosphere may significantly influence the atmospheric flow in the observable middle and upper atmosphere of hot Juptiers. Deitrick et al. (2020) also stated a retrograde flow at 10^6 Pa in the simulations of HD 189733b. Investigating eddy transport, Mayne et al. (2017) noticed a deceleration of the superrotating jet due to the evolution of the deep atmosphere (the model did not reach steady state after 10 000 Earth days). In their

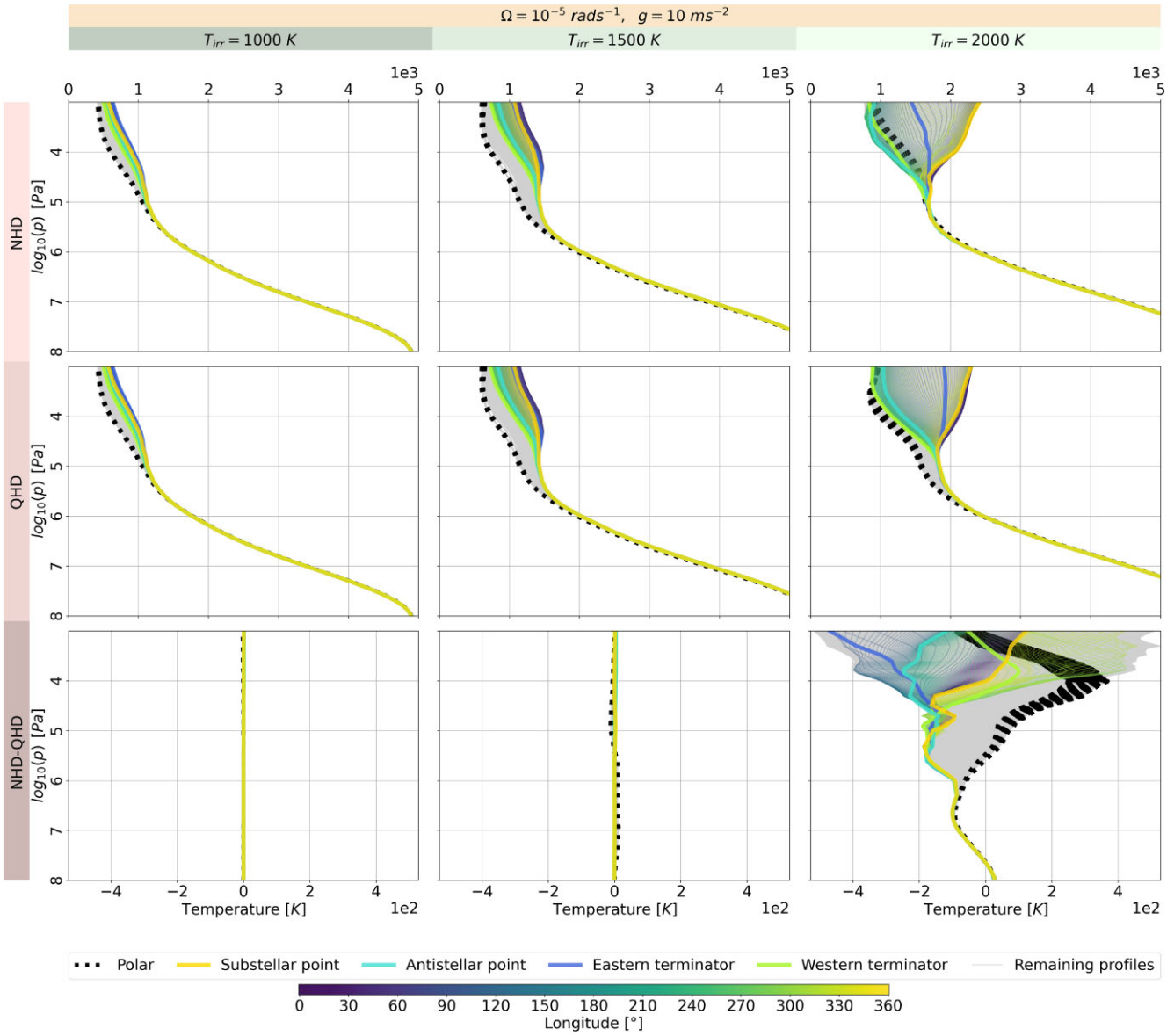

Figure 17. T-p profiles of covering entire planet for the NHD and QHD equation sets with $\Omega = 1 \times 10^{-5}\ rad\,s^{-1}$, $g = 10\,ms^{-2}$, and with altering T_{irr}. The coloured lines indicate T-p profiles along the equator and its coordinates by the colourbar. The dotted black thin line shows T-p profiles at the latitudes 87°N and 87°S. The bold coloured lines represent T-p profiles at the western, eastern terminators, sub-, and antistellar point. The grey lines represents all the other T-p profiles.

study, air masses sink over the poles and rise over the equator. The horizontal temperature gradient at greater depths ($p > 10^6\ Pa$) powers the deep circulation.

Retrograde flow has been noted in simulation in few cases; Showman et al. (2015) performed simulations for HD 189733b altering irradiation (warm and cool Jupiters) and rotation periods (0.55, 2.2, and 8.8 Earth days). Their simulations with fast rotation or low irradiation show retrograde flow in the zonal-mean wind. More retrograde flow patterns were found for tidally locked exo-Earths with fast rotation (less than 3 Earth days; Carone, Keppens & Decin 2015). Carone et al. (2020) showed that retrograde flow over the equator can appear on dense and hot Jupiters. Mayne et al. (2017) highlighted that vertical angular momentum in balance of horizontal interactions plays a crucial role for the evolution of superrotation. Carone et al. (2020) identified unusually deep wind jets (already predicted by Thrastarson & Cho 2011) accompanied by deeper convective layers. Those deep wind jets may impact the upper atmosphere ($p < 10^6\ Pa$) by zonal momentum transport at depths ($p > 10^6\ Pa$) that was supposed to increase with faster rotation. More studies are required to understand the exact mechanisms and regimes that can produce retrograde flow.

Mayne et al. (2019) analysed indirectly the effect of gravity on the dynamic equation set via temperature contrast and the scale height. They concluded that the maximum variation appears between varying and constant g, when the temperature contrast is altered, and their view when g is supposedly altered as well (scale height). The deep (equation) case varies roughly 30 per cent to the full (equation) case at the top of the atmosphere. Mayne et al. (2019) stated that the resulting flows in the simulations with the primitive and deep equation set respond independently of the treatment of g. Our results support

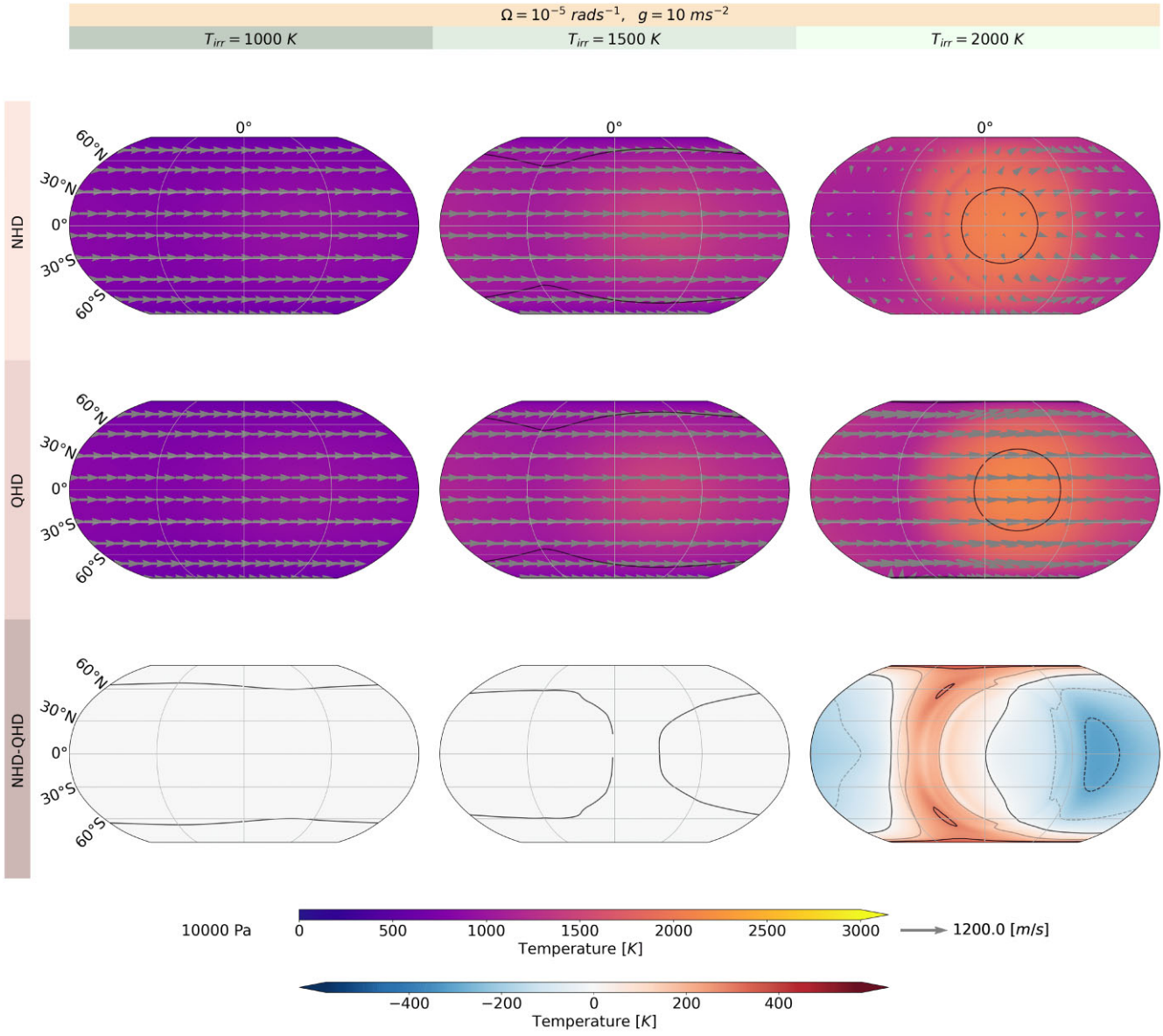

Figure 18. Temperature and wind speed at $10^4\ Pa$ for the NHD and QHD equation sets with $g = 10\,ms^{-2}$, $\Omega = 1 \times 10^{-5}\ rad\,s^{-1}$, and with altering T_{irr}.

the idea of independence of g partially; At high gravity differences among NHD and QHD nearly vanish. It can be explained by the growing dominance of the gravity term over other terms. But at low gravity, the other terms in the NHD and QHD equation set reveal their effects and the related differences that cannot anymore be encountered by the gravity term. We cannot comment how the full equation responses in comparison to other equation sets, since the THOR model does not provide the option for varying g yet. Only an extensive study on the effects of the gravity term with different dynamical equation sets can provide a full answer. The combination of high gravity in the deep atmosphere with decreasing gravity in the upper atmosphere may even lead to total different climate states than presented in here.

We have to note that the Bond albedo changes with g with altered gravity and with that the incoming shortwave radiation. Therefore, we see effects of g combined with radiative effects on the dynamics.

Mayne et al. (2019) showed that increased planetary temperature contrast lead to an accelerated zonal flow while comparing the primitive with the full equation set. They see significant changes in the thermal structure. As a consequence the regime becomes advectively dominated. The changes in the zonal flow and advection end in changed temperature structure (Mayne et al. 2019). We see growing differences between the NHD and QHD equation set in the zonal momenta in our simulations when we increase the irradiation temperature. At lower irradiation temperatures, the differences nearly vanish and a superrotation is evolved. The deviations in the temperature remain much smaller at lower temperatures. That is not surprising, since the temperature is not included directly in the altered terms in the QHD case, $\frac{Dv_r}{Dt}$, $\mathcal{F}_r$ and $\mathcal{A}_r$. Therefore, the deviations have to rise from the changed dynamics that alter the temperature advection and therefore the temperature structure at higher irradiation temperature more significantly. At higher irradiation temperatures, the spread in the T-p profiles (day–night contrast) increases with higher irradiation temperatures. Hence the temperature advection gets a more decisive role in the temperature structure of planets. In the comparable study of Deitrick et al. (2020), only minor differences

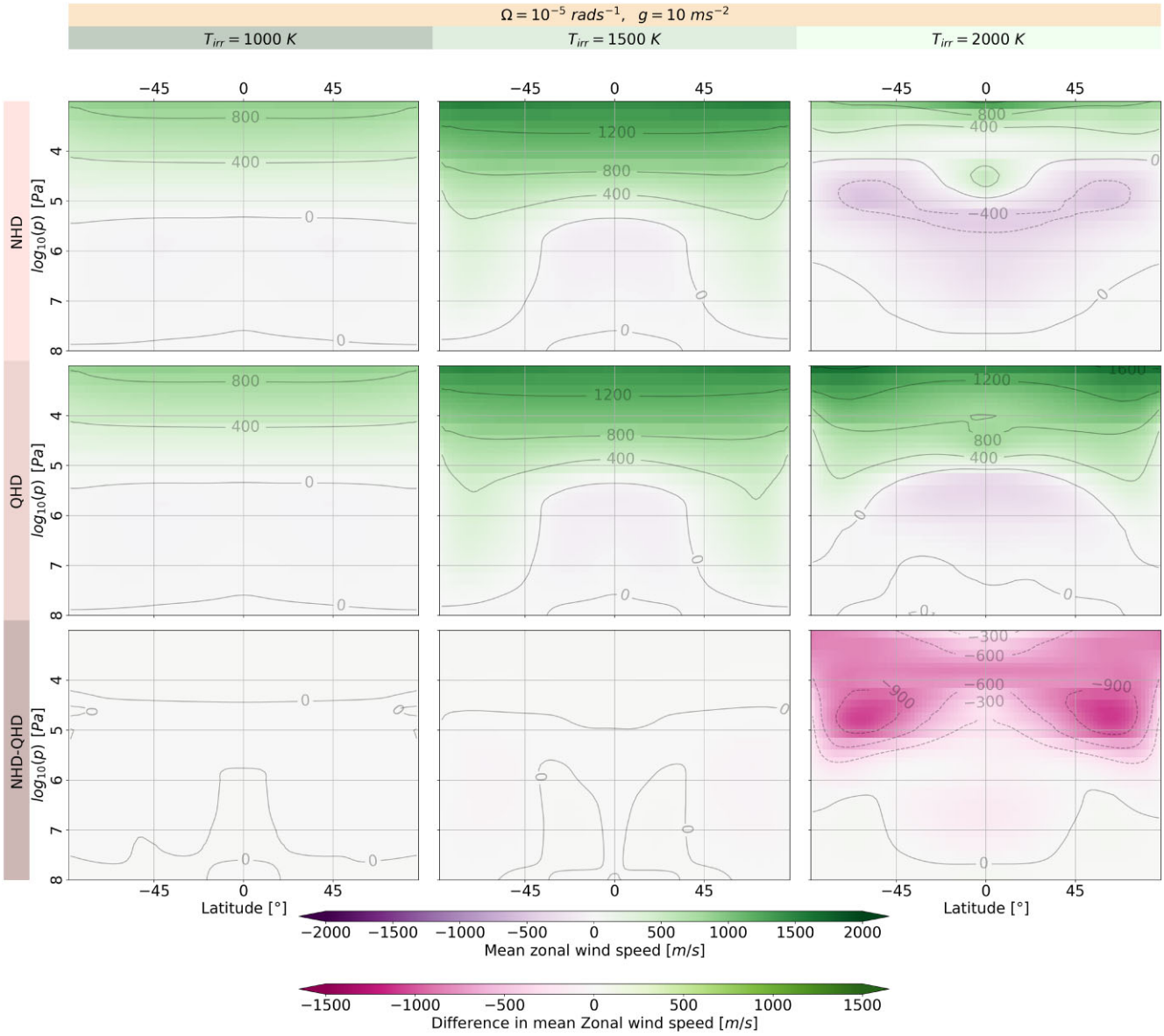

Figure 19. Zonal mean wind at each grid point for the NHD and QHD equation sets with $g = 10\,ms^{-2}$, $\Omega = 1 \times 10^{-5}\ rad\,s^{-1}$, and with altering T_{irr}.

appear in the temperature among simulations with NHD and QHD equation sets in the simulations of HD 189733b. They stated slightly higher velocities in the NHD case and differences of jet velocity of roughly 5 per cent. THOR produces a superrotation as well in their simulation.

May et al. (2022) compared Spitzer phase curves and showed evidence for a trend of increasing phase offset with increasing orbital period at $4.5\mu m$ (for $T_{\rm eq} \equiv 1300\,K$), as already shown in Parmentier & Crossfield (2018). Our results show larger offsets with larger orbital periods for the NHD case when gravity is low (for $T_{eq} \equiv 1414.21\,K$). This comes along with a weaker overturning circulation with increasing Ω (see the plots of the overturning circulation in the **supplementary file**). The QHD case does not show a trend in this regard and the offset changes more due to climate state changes at low g. At higher gravity, the offset switches direction due to climate state changes. We see a decrease of the eastward offset of the hotspot when superrotation is prograde, g is high, and Ω increases.

Moreover, Zhang & Showman (2017) suggested that only the radiative and advective time-scales affect the hotspot offset. So, the radiative time-scale should not be changed by the rotation rate. Consequently, the rotation rate should change the wind speed in tidally locked hot Jupiter when the rotation rate is altered because of the trend of the offset. Therefore, faster rotation rates should lead to weaker equatorial jets. In our simulations, we see the radiative time-scales changing in the NHD and QHD case when the rotation rate is altered due to temperature advection. Moreover, the radiative time-scales on the nightside vary much more than those on the dayside when the rotation rate alters. Nevertheless, we see a weakening of the equatorial jets with higher rotation rates in the NHD case. The QHD case does not show weakening, much more a strengthening with higher rotation rates. Looking at the entire parameter grid we simulated, the offset changes, when we altered g, $T_{\rm irr}$, and Ω. We see the offset changes due to several parameters. Similarly, Hammond & Pierrehumbert (2018) showed dependence of the offset on a non-dimensional parameter, which is related to the radius, scale height,

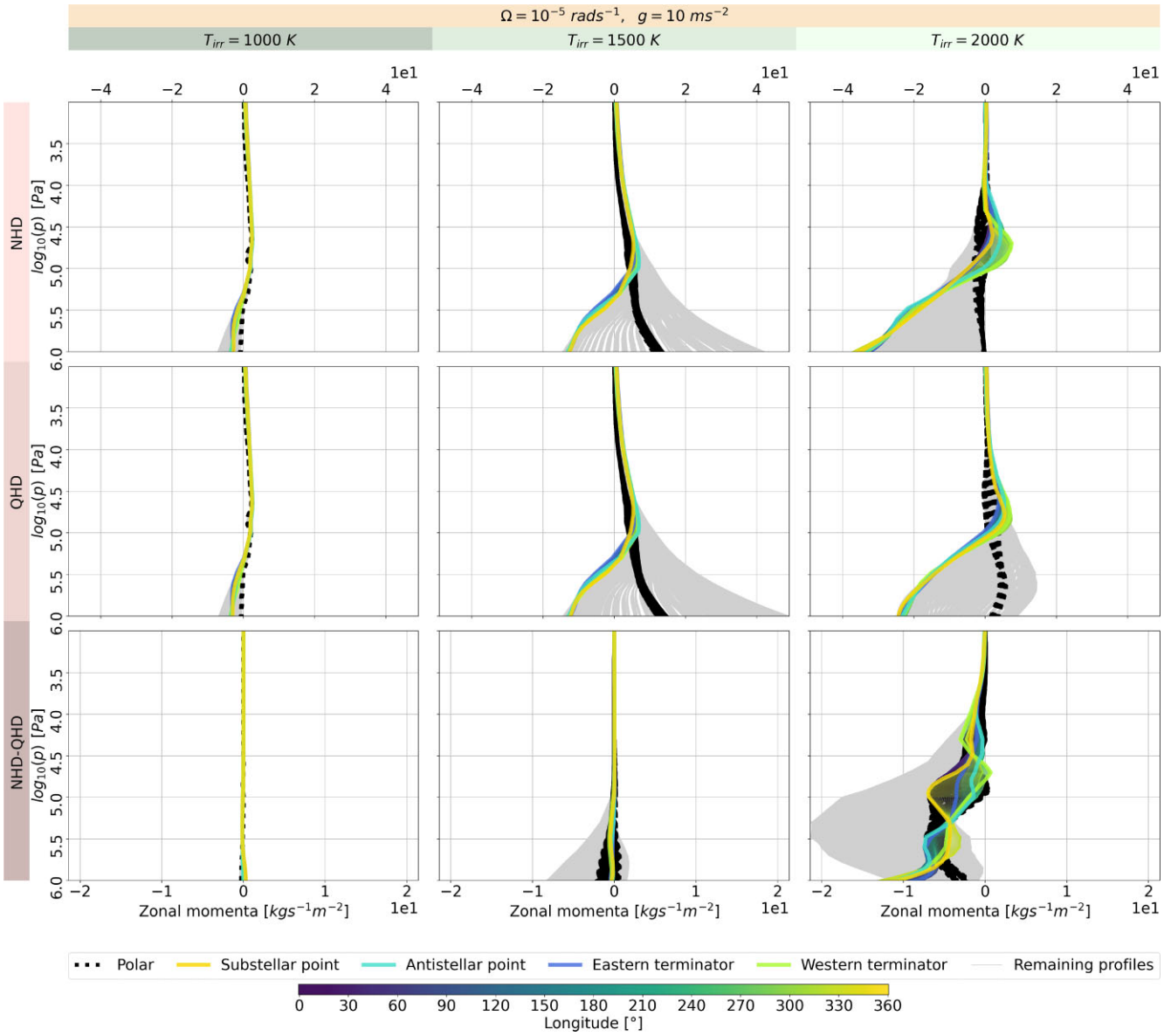

Figure 20. Zonal momenta at each grid point for the NHD and QHD equation sets with $\Omega = 1 \times 10^{-5}\ rad\,s^{-1}$, $g = 10\,ms^{-2}$, and with altering T_{irr}. The profiles show only pressures $p \leq 10^6\ Pa$ (without the pressure range $10^6 \geq p \leq 10^8$). The coloured lines indicate momenta profiles along the equator and its coordinates by the colourbar. The dotted black thin line shows momenta profiles at the latitudes 87°N and 87°S. The bold coloured lines represent momenta profiles at the western, eastern terminators, sub-, and antistellar point. The grey lines represents all the other momenta profiles.

gravity, and rotation rate. May et al. (2022) observed the dependence of the offset is not only bound to the rotation rate as in hot Jupiters but also to gravity for cooler Jupiters with consistent nightside temperature near $\sim$1000 K. The different jet structures and offsets of the hotspots in our simulated parameter grid imply a dependence on multiple parameters as Hammond & Pierrehumbert (2018) and May et al. (2022) suggested.

Comparable simulations to ours in the studies of Kataria et al. (2015; SPARC/MITgcm) and Schneider et al. (2022) (expeRT/MITgcm), but computed with HPEs, show three times higher wind speeds for WASP 43b than our results. Unfortunately, the lower wind speeds in our simulations are mostly due to the limit imposed by the model top. Moreover, our parametrization differs by slightly higher $T_{\rm irr}$ and slightly higher Ω. The GCM with HPE in Kataria et al. (2015) predicts a superrotation with high wind speeds up to 4800 ms^{-1}. The wind speeds in our simulations lie around $\sim$1000 and $\sim$500 ms^{-1} for our QHD case with $T_{\rm irr} = 2000\,K$, $g = 10\,ms^{-2}$, $\Omega = 1 \times 10^{-5}$, and $\Omega = 1 \times 10^{-4.5}$, respectively. The QHD case already predicts too high wind speeds compared to the NHD case depending on the parametrization. The HPEs seem to predict even much higher wind speeds at this parametrization, but it needs to be studied more extensively. Furthermore, the simulation for HD 209458b in Kataria et al. (2015) can be classifed in a transitional state between our *three prograde jets* and the *radial flow*. Therefore, we expect elements of a three prograde jets combined with a dominant divergent component if computed with the NHD equation set.

On the other hand, if we compare simulations for HD 189733b, the THOR model (with the double-grey dual band RT scheme) produces a prograde superrotation in Deitrick et al. (2020) with wind speeds up to $\sim$5600 ms^{-1} in the NHD case, even higher than

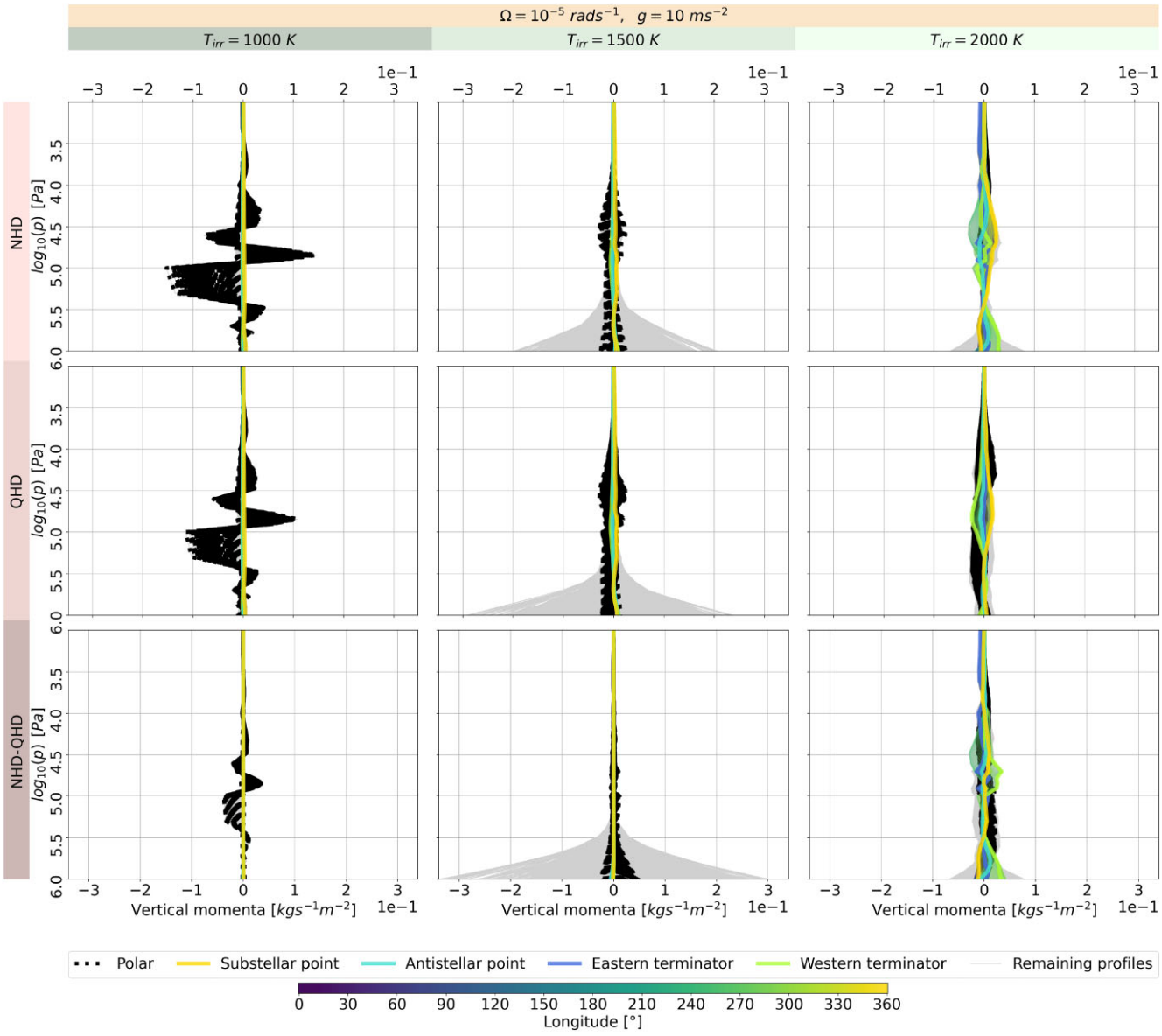

Figure 21. Vertical momenta at each grid point for the NHD and QHD equation sets with $\Omega = 1 \times 10^{-5}\, rad\, s^{-1}$, $g = 10\, ms^{-2}$, and with altering T_{irr}. The profiles show only pressures $p \leq 10^6\ Pa$ (without the pressure range $10^6 \geq p \leq 10^8$). The coloured lines indicate momenta profiles along the equator and its coordinates by the colourbar. The dotted black thin line shows momenta profiles at the latitudes 87°N and 87°S. The bold coloured lines represent momenta profiles at the western, eastern terminators, sub-, and antistellar point. The grey lines represents all the other momenta profiles.

in the QHD case. Kataria et al. (2016) simulated HD 189733b as well. The zonal mean wind speed goes a bit beyond 3200 ms^{-1}, but it remains lower than in Deitrick et al. (2020). Although Deitrick et al. (2020) and Kataria et al. (2016) predict a superrotation, the jet maxima is found at 2 mag higher pressures in Kataria et al. (2016). We consider different physical scheme as well combination with different dynamical equation sets have an effect on the jet structure and the climate state, but is has to be investigated further. In a comparison of radiative schemes, Lee et al. (2021) showed different RT schemes can lead to different wind speed and temperatur e structures.

Hot Jupiter climates are often associated with a equatorial prograde superrotating jet (see Showman, Tan & Parmentier (2020) for full review). That concept is often supported by GCM simulations that show a prograde superrotation. Comparing jet systems in different studies, most simulations for hot Jupiters [e.g. Kataria et al. (2015, 2016); Amundsen et al. (2016); Schneider et al. (2022)] show only prograde superrotation. So far, only Carone et al. (2020) predicts a retrograde flow for WASP 43b, embedded in a strong superrotation, with the GCM MITgcm with HPEs. Like in Carone et al. (2020), we see retrograde flow in similar cases depending on the parametrization, but we did not explicitly simulate WASP 43b. Nevertheless, we predict even a retrograde superjet in one of the four different circulation states. The evolution of climate states and the jet structures depend on the parametrization and choice of the dynamical equation set. Zonal momentum transport may play a crucial role for the evolution of retro-, prograde, and cross-the-poles wind flow. Such association with the momentum transport was found by Carone et al. (2020). They associate the upwards zonal momentum transport to a deep jet, which leads to the retrograde flow in the upper

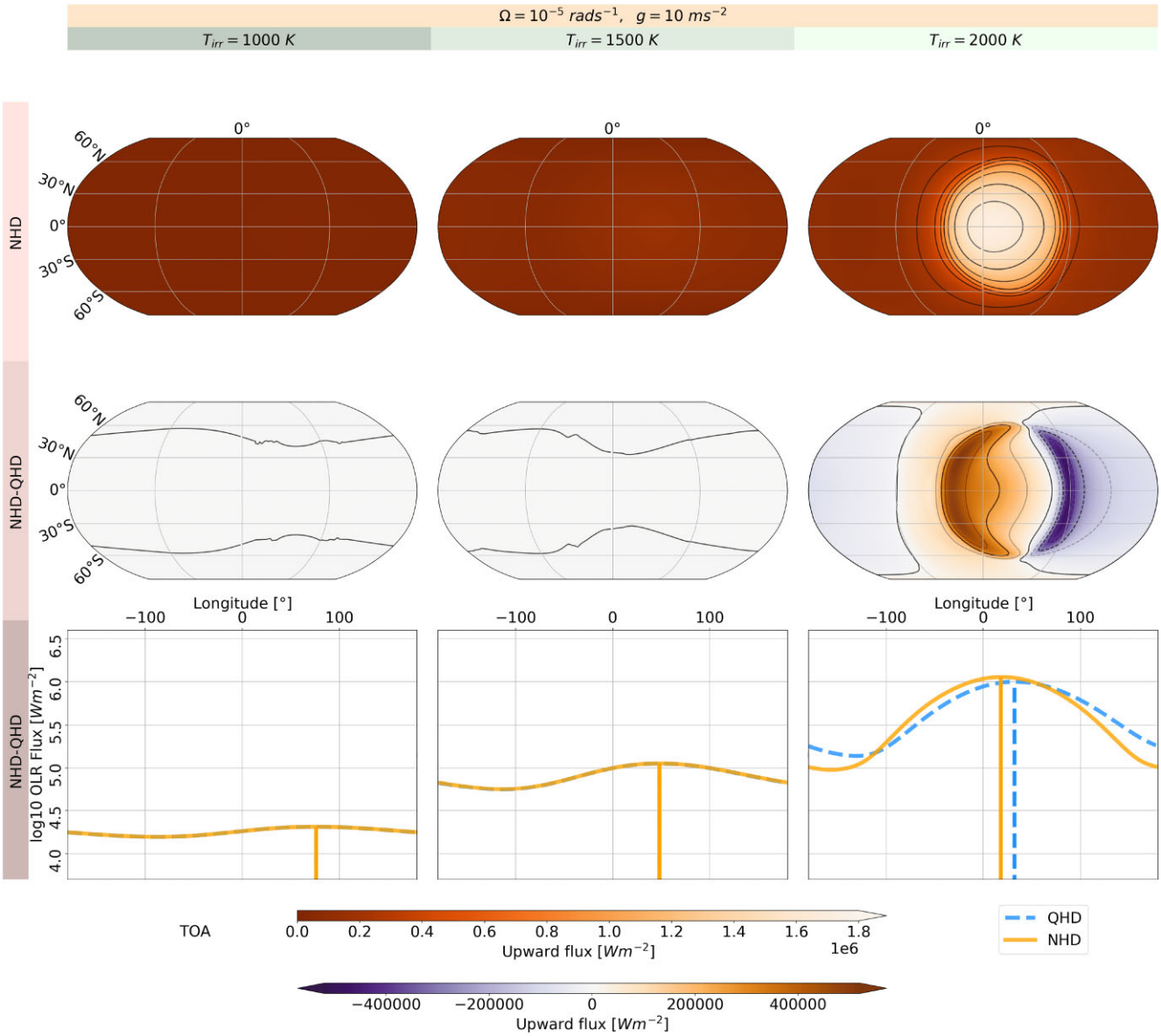

Figure 22. OLR fluxes at the top of the atmosphere for NHD and QHD equation sets with $\Omega = 1 \times 10^{-5}\ rad\,s^{-1}$, $g = 10\,ms^{-2}$, and with altering T_{irr}. Third row: OLR phase curves.

atmosphere. Such momenta transport can be missed by HPEs, since they ignore several terms of the full equation set related to momenta transport such as $2\Omega\cos(\phi)$, $\frac{-uw}{r}$ and $\frac{-uv}{r}$ (see the full review on dynamical equation sets in Mayne et al. 2014a). Even the NHD case does represent the full equation set since g does not alter with the altitude. We illustrated some effects of g on the different dynamics and outcomes by altering g. Therefore, our simulation outcome may change drastically, depending on the parametrization when the full equation set is implemented in THOR.

Regarding the evolution of different jet system, Sergeev et al. (2022b) demonstrated an interesting case of climate bistability in TRAPPIST-1e. They found two distinct jet systems for a $10^5\ Pa$ nitrogen-dominated atmosphere. They characterized one strong equatorial prograde jet (with strong day-night contrast) and two mid-latitude prograde jets (with weak day-night contrast). In their numerical experiments, the bistability was highly sensitive to the model setup, such as initial conditions, surface boundary conditions, physical parametrization of convection and cloud radiative effects. They found a balance between the zonally asymmetric heating, mean overturning circulation, and mid-latitude baroclinic instability. As not the only study, Edson et al. (2011), Noda et al. (2017), and Carone et al. (2018) discovered transitional states between well-defined jet systems and climate states similarly to our study. Some rocky exoplanets seem to be sensitive not only to GCM setup Sergeev et al. (2022b) but as well to the GCM choice, as shown by Sergeev et al. (2022a) and Turbet et al. (2022). As an addition to these studies, our study shows that choice of the dynamical equation set within a GCM leads to evolution of different climate state.

The discussion about the dynamics on hot Jupiters (e.g. Kataria et al. 2015; Mendonça et al. 2018b; Mayne et al. 2019; Carone et al. 2020; Deitrick et al. 2020; Schneider et al. 2022) together with our results have no reached a consensus yet. Further studies of the dynamics of hot Jupiters with GCMs with the full equation set are needed.

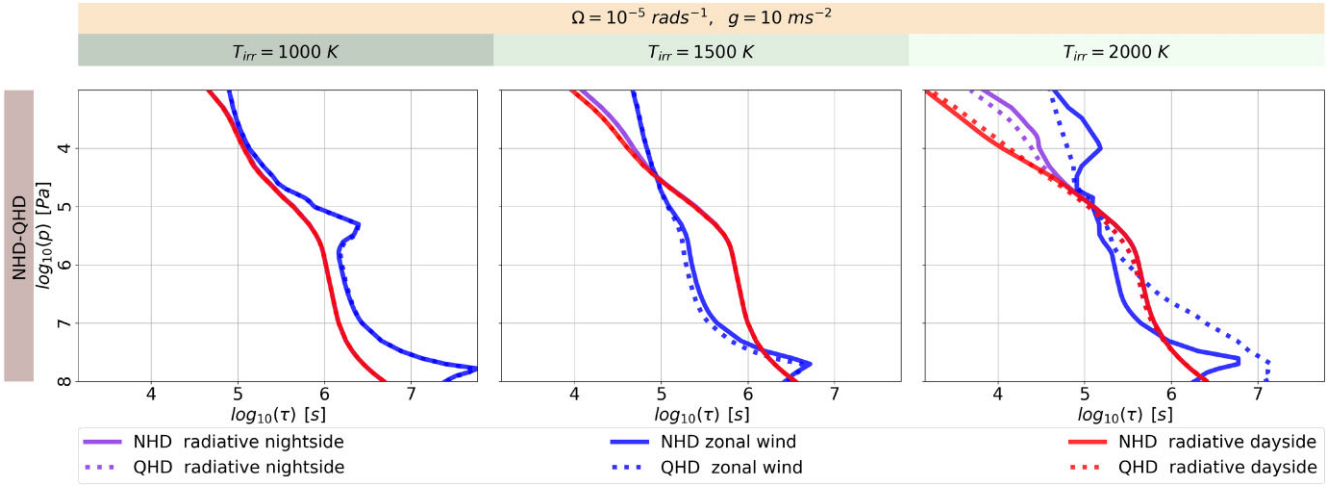

Figure 23. Radiative and zonal wind time-scales for the NHD and QHD equation sets with $\Omega = 1 \times 10^{-5}\ rad\,s^{-1}$, $g = 10\,ms^{-2}$, and with altering T_{irr}.

Many simulations uses HPEs which come along with shortcomings due to their approximations made for Earth. We demonstrate with our comparison that such approximations can lead to complete changes in the jet structure and climate state that just arise from the choice of the dynamical equation set. In several parameter settings, we see prograde superrotation, but as well deviations from prograde superrotation, such as retrograde superjet, disrupted superrotation and a three-jet instead of a one-jet structure. None the less, we should be careful since climate state and observational features may change over long integration times (e.g. 50 000–250 000 Earth days) as Wang & Wordsworth (2020) have shown. They saw the evolution of two prograde off-equatorial jets to a single prograde equatorial jet ranging up to the poles. Also, they found the hotspot shift becomes eastward after long integration times. Regarding the reason of the long convergence, they hint to the long radiative time-scales in the deep atmosphere. They run simulations for the warm sub-Neptune GJ 1214b with the GCM LMDZ with HPEs and with two-stream grey gas RT scheme. Our comparable simulations have too high $T_{\rm int}$ in comparison to GJ 1214b and might be in a different climate state.

We assume the climate states on hot Jupiters are more diverse than the simple superrotation. Armstrong et al. (2016) found a westward shift of the hotpsot and brightness peak with Kepler measurements of HAT-P-7b. Similarly, May et al. (2022) observed a westward offset of the hotspot for WASP 140b. Moreover, Dang et al. (2018) presented thermal phase observations of the hot Jupiter CoRoT 2b obtained with the Infrared Array Camera on the Spitzer Space Telescope. They detected a westward offset of the hotspot of $23 \pm 4°$. The large westward offset in Dang et al. (2018) might be another evidence of retrograde flow or even retrograde superjet in hot Jupiter atmospheres. Simulations including magnetohydrodynamics (MHD) predicted a westward flow (Rogers & Komacek 2014). A more recent study (Hindle et al. 2019) showed simulations with MHD, which led to westward shifts of the hotspot for HAT P-7b and CoRoT 2b. For these reasons, we conclude hot Jupiter atmospheres might be more diverse than so far assumed.

5.3 Limitations and future improvements

The GCM THOR can encounter numerical instability when the gradient between the nightside and dayside temperatures is too large (Deitrick et al. 2020), most problematic when modelling ultra hot Jupiters. As a consequence, we could not simulate pressures lower than $\sim 7 \times 10^2$ or $10^3\ Pa$ (depending on the parametrization), which affects the dynamics and temperature structure to some degree. Future updates to the THOR GCM will address the issue of large day-night temperature gradients.

Mayne et al. (2019) performed simulations for warm, tidally locked and slowly rotating Neptunes and super Earths with a duration of 1000 Earth days. They saw the evolution of the maximum zonal wind speed and structure ceased in their simulations at lower pressures (pseudo-steady). The deep, high pressure atmosphere still evolve slowly in their simulations after 1000 Earth days. The slow evolution of the deep atmosphere does not appear to have a significant effect on the dynamics of the upper, low pressure atmosphere for hot Jupiters (Mayne et al. 2017). On the contrary, Carone et al. (2020) suggested advection of zonal momenta upwards from the deeper atmosphere.

In this study, we run the simulations for 5000 Earth days and for a certain number of Earth days and did not set the duration according to a convergence condition. The computation time would take too long for two dozens of simulation cases to finish the study in a meaningful time. We simulated the deep atmosphere to $10^8\ Pa$, which needs significantly more time to converge (Mayne et al. 2017). However, we simulated the deep atmosphere to stabilize THOR, especially for the first few hundreds days. Regarding sufficient time periods for convergence to steady state, Wang & Wordsworth (2020) simulated GJ 1214b for 50 000 d to observe the transition from two equatorial jet into one jet. Such long integration times are beyond our current computational resources for parameter grid we computed. Christie et al. (2022) set the simulation time on basis of evolved features that different models create early on. Important feature such as the equatorial jet can be evolved in 7800 d (Menou 2012) for GJ 1214b. A shorter run time was used in Komacek et al. (2022) but with a shallower atmosphere and a surface pressure of $10^6\ Pa$. A more detailed analysis on the convergent time for deep atmosphere is done by Schneider et al. (2022). They did run simulations with a surface pressure of $10^8\ Pa$ for WASP 43b and HD 209458b for 12 000 Earth days. While HD 209458b did converge within the 12 000 Earth days, WASP 43b did evolve steadily during the full simulation time. The temperature change rate drops from $\sim$1.5 to $\sim 0.05\ Kd^{-1}$ at the end of the simulation. Regarding the final state of the deeper atmosphere, Schneider et al. (2022) confirmed the independence of the initial conditions for WASP 43b. As Sergeev et al. (2022b) showed the

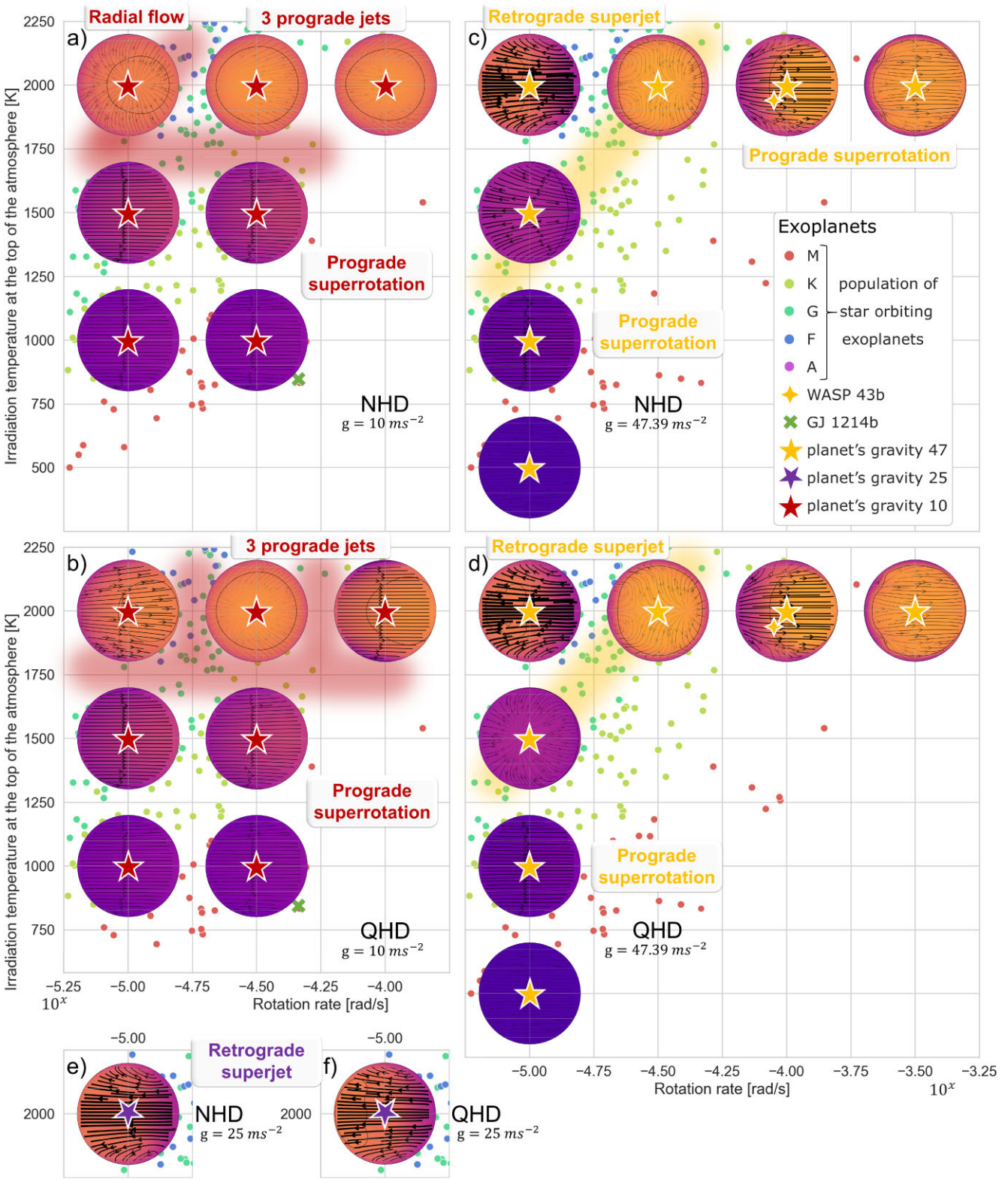

Figure 24. Classification of the simulations to circulation and climate states in the parameter grid of known exoplanets (retrieved on the 2021 November 22 from the entries with sufficient information in the NASA Exoplanet Archive - Akeson et al. 2013). Orthographic projections shows the temperature and horizontal wind flow on the dayside at 10^4 *Pa*. The shaded lines in red and yellow show assumptions for possible classifiers. Subplots (a) and (b) show the classification of simulations for the NHD, respectively, QHD case with $g = 10\,ms^{-2}$, altering Ω, and with altering T_{irr}. Subplots (c) and (d) show the classification of simulations for the NHD, respectively, QHD case with $g = 47.39\,ms^{-2}$, altering Ω, and with altering T_{irr}. Subplots (e) and (f) show the classification of simulations for the NHD, respectively, QHD case with $g = 25\,ms^{-2}$, $\Omega = 1 \times 10^{-5}\,rad\,s^{-1}$, and $T_{irr} = 2000\,K$.

Table 2. Characteristic values and scales in comparison to the circulation and climate states in the NHD case. The characteristics include scale height H, Rossby number Ro, Rossby deformation radius L_D, Rhines scale, and the Brunt–Väisälä frequency N of the all simulations using a similar setting as in Parmentier (2014) and Lee et al. (2020; for details of the calculations see Appendix F). We set $L = R_p$ and the characteristic velocity in a range between 100 and 4500 ms^{-1}. The Rossby number and Rossby deformation radius is evaluated for the mid-latitudes. For the Rossby deformation, we set $D = H$. For the Rhines scale, we use the equatorial value for the β-Term and use the range between 100 and 4500 ms^{-1} for the wind speeds. Rossby deformation radius and Rhines scale are calculated as ratios to R_p.

Ω ($rads^{-1}$)	g (ms^{-1})	T_{irr} (K)	T_{eq} (K)	H (km)	Ro -	L_D (R_p)	L_{Rh} (R_p)	N (s^{-1})	Circulation state -	Features -
10^{-5}	10	2000	1414.21	525.24	0.098–4.39	4.19	0.83–5.54	0.00816	three prograde jets and radial flow	three deeper retrograde jets
$10^{-4.5}$	10	2000	1414.21	525.24	0.031–1.39	1.32	0.46–3.11	0.00816	three prograde jets	three deeper retrograde jets
10^{-4}	10	2000	1414.21	525.24	0.0098–0.44	0.42	0.26–1.75	0.00816	three prograde jets	shallow equatorial retrograde flow
10^{-5}	25	2000	1414.21	210.1	0.098–4.39	4.19	0.83–5.54	0.0204	retrograde superjet	jet width from pole to pole
10^{-5}	47.39	2000	1414.21	110.83	0.098–4.39	4.19	0.83–5.54	0.039	retrograde superjet	jet width from pole to pole
10^{-5}	10	1000	707.11	262.62	0.098–4.39	2.96	0.83–5.54	0.011	prograde superrotation	jet width from pole to pole
10^{-5}	10	1500	1060.66	393.93	0.098–4.39	3.63	0.83–5.54	0.0094	massive prograde superrotation	jet width from pole to pole
$10^{-4.5}$	47.39	2000	1414.21	110.83	0.031–1.39	1.32	0.46–3.11	0.039	interrupted prograde superrotation	two interrupted retrograde high-latitude jets
10^{-4}	47.39	2000	1414.21	110.83	0.0098–0.44	0.42	0.26–1.75	0.039	prograde superrotation	-
10^{-5}	47.39	1000	707.11	55.42	0.098–4.39	2.96	0.83–5.54	0.055	retrograde superjet	jet width from pole to pole
10^{-5}	47.39	1500	1060.66	83.12	0.098–4.39	3.63	0.83–5.54	0.045	prograde superrotation	jet width from pole to pole

high sensitivity of the model setup in relation to the evolution of the distinct climate states, more studies are needed to examine bistability and even multistability of exoplanets.

At lower resolution, THOR approaches steady state around 2500–3000 Earth days for simulations of HD 189 733 b, while high-resolution simulations converge after 10 000 Earth days [Deitrick et al. (2020), indicated by the superrotation index according to Mendonça (2020)]. The zonal flow undergoes a quick development and changes only very little after 2000 Earth days (Deitrick et al. 2020) in the simulations of HD 189733b. They also showed that the upper atmosphere reached steady state, although the lower atmosphere did not reach it in their simulations with $g_{level} = 5$ (around 2°). For hot Jupiters, we expect even shorter convergence times due to higher temperatures so that 5000 d are sufficient to observe differences between NHD and QHD equation sets at pressures $p \leq 10^6\ Pa$.

Higher resolutions conserve mass better as Deitrick et al. (2020) noted that THOR conserves mass at $g_{level} = 5$ (around 2°) slightly less well than at $g_{level} = 6$ (around 1°), although the output looks qualitatively very similar. Moreover, terms such as $\cos\phi$ become relevant for the mesoscale motion (Draghici 1989) on Earth. Furthermore, more complex atmospheric motions may appear if the model resolution increases like on Jupiter (Schneider & Liu 2009; Gastine & Wicht 2021; Heimpel et al. 2022). On exoplanets, a higher resolution may lead to larger differences among simulations with different dynamical equation sets. Furthermore, mass, energy, numerical dissipation, and integration errors lead to gradual changes of the total axial momentum (see more details in Deitrick et al. 2020; Mendonça 2020).

Regarding the gravity, THOR has a constant value throughout the atmosphere. A decreasing gravity with height would change the simulation outputs and their realism. We expect further implications for the QHD equation set and other approximations, especially at higher altitudes respectively at lower pressures ($p < 10^5\ Pa$) since we find the largest differences at low gravity.

6 SUMMARY AND CONCLUSIONS

For exoplanet atmosphere GCMs, several hydrodnymaic equation sets are used across the literature. However, only a few studies have compared the differences between equation sets and their effects on the atmospheric dynamical properties (Mayne et al. 2019; Deitrick et al. 2020). This will be important to consider as spectral phase curve data is produced by JWST.

In this study, we compared the NHD and QHD equation sets (following the nomenclature and definitions in Deitrick et al. 2020) in the GCM THOR. We simulated atmospheres across a parameter grid to reveal the validity of the equation sets for a wide range of the exoplanet population. Additionally, we implemented a two-stream, non-grey, 'picket-fence' scheme to THOR, which increases the realism of the RT in the model.

Our results show significant differences between the NHD and QHD equation sets in the GCM THOR for fast rotation rates, lower gravity, and higher irradiation temperatures. The NHD and QHD equation sets in THOR differ only in the terms Dv_r/Dt, the Lagrangian derivative of the vertical velocity, $\mathcal{F}_r$, the hyperdiffusive flux, and $\mathcal{A}_r$, the vertical component of the advection term. However, those terms cause significantly different results in the dynamics and the vertical temperature structure in several regimes. Depending on the parameters, the NHD and QHD equation sets even evolve to different dynamics, radiative regime, and climate state.

Overall, our study shows the evolution of different climate states that arise just due to different selection of Navier-Stokes equations and approximations. We show the implications of approximations made for Earth but used for non Earth-like planets. Our results agree qualitatively to comparable studies of Mayne et al. (2019) and Deitrick et al. (2020). Mayne et al. (2019) made a similar comparison but with the Met Office Unified Model. They compared simulations of slow-rotating, small Neptune-sized planets with the primitive and deep equation set. Deitrick et al. (2020) used THOR in a similar comparison of the NHD and QHD equation sets and showed already significant differences in the dynamics in two regimes (Earth like case

and HD 189733b). We showed that differences between the NHD and QHD equation sets can vary depending on the parametrization and choice of the dynamical equation set. Finally, our results show the relevance in the use of different dynamical equation sets depending on planetary and system properties.

Future investigations may extend this study by comparing the full equation set, NHD equation set and hydrostatic, shallow approximations in GCMs. Additionally, Mayne et al. (2019) suggested to implement chemical equilibrium (Drummond et al. 2016, 2018b) and a cloud scheme like in Lines et al. (2018b). A more sophisticated spectral RT scheme like Deitrick et al. (2022) may also alter our findings. Longer simulations times, similar to Wang & Wordsworth (2020), and GCMs with the full equation set may reveal new circulation and climate states as well as multistabilities.

ACKNOWLEDGEMENTS

PAN and EKHL are supported by the SNSF Ambizione Fellowship grant (#193448). Parts of this work have been carried out within the framework of the NCCR PlanetS supported by the Swiss National Science Foundation under grants 51NF40_182901 and 51NF40_205606. Financial support to RD was provided by the Natural Sciences and Engineering Research Council of Canada (NSERC; Discovery Grant RGPIN-2018-05929), the Canadian Space Agency (Grant 18FAVICB21), and the European Research Council (ERC; Consolidator Grant 771620). MH gratefully acknowledges funding from Christ Church, Oxford. Data and plots were processed and produced using PYTHON version 3.9 (Van Rossum & Drake Jr 1995) and the community open-source PYTHON packages BOKEH (Van de Ven et al. 2022), MATPLOTLIB (Hunter 2007), CARTOPY (Met Office 2015; Elson et al. 2022), JUPYTER (Kluyver et al. 2016), NUMPY (Harris et al. 2020), PANDAS (pandas development team 2020), SCIPY (Jones et al. 2001, Virtanen et al. 2020), SEABORN (Waskom 2021), WINDSPHARM (Dawson 2016), and XARRAY Hoyer & Hamman (2017). Calculations were performed on UBELIX (http://www.id.unibe.ch/hpc), the HPC cluster at the University of Bern. We thank the IT Service Office (Ubelix cluster), the Physikalisches Institut and the Center for Space and Habitability at the University of Bern for their services. This research has made use of the NASA Exoplanet Archive, which is operated by the California Institute of Technology, under contract with the National Aeronautics and Space Administration under the Exoplanet Exploration Program (NASA Exoplanet Archive Institute and Akeson et al. 2013).

DATA AVAILABILITY

We used the development version of the GCM THOR (available on https://github.com/exoclime/THOR). The code for the picket-fence scheme and the new mode for the initial conditions were uploaded on the lead author's GitHub: https://github.com/PA-NOTI/THOR_picket_fence_scheme. The code on the lead author's GitHub was used to run the GCM THOR simulations. The added features got integrated in the main Github of the GCM THOR. The input and output files of the GCM THOR are available on Zenodo, DOI: 10.5281/zenodo.7620774 and DOI: 10.5281/zenodo.8014271. All other data and code are available from the authors on a collaborative basis.

REFERENCES

Adams S. et al., 2019, J. Parallel Distrib. Comput., 132, 383
Akeson R. L. et al., 2013, PASP, 125, 989
Álvarez Ó., Izquierdo A., González C. J., Bruno M., Mañanes R., 2019, Cont. Shelf Res., 181, 174
Amundsen D. S. et al., 2016, A&A, 595, A36
Arcangeli J. et al., 2019, A&A, 625, A136
Armstrong D. J., de Mooij E., Barstow J., Osborn H. P., Blake J., Saniee N. F., 2016, Nature Astron., 1, 0004
Bean J. L. et al., 2018, PASP, 130, 114402
Beltz H., Rauscher E., Brogi M., Kempton E. M. R., 2021, AJ, 161, 1
Bjerknes V., 1904, Meteorol. Z., 21, 1
Blecic J., Dobbs-Dixon I., Greene T., 2017, ApJ, 848, 127
Bretherton F. P., 1964, Tellus, 16, 181
Broeg C. et al., 2013, in Saglia R., ed., EPJ Web of Conferences Vol. 47, Hot Planets and Cool Stars. Garching, Germany, p. 03005
Caldas A., Leconte J., Selsis F., Waldmann I. P., Bordé P., Rocchetto M., Charnay B., 2019, A&A, 623, A161
Carone L., Keppens R., Decin L., 2015, MNRAS, 453, 2412
Carone L., Keppens R., Decin L., Henning T., 2018, MNRAS, 473, 4672
Carone L. et al., 2020, MNRAS, 496, 3582
Cauley P. W., Shkolnik E. L., Llama J., Lanza A. F., 2019, Nature Astron., 3, 1128
Chandrasekhar S., 1935, MNRAS, 96, 21
Charnay B., Meadows V., Misra A., Leconte J., Arney G., 2015, ApJ, 813, L1
Charney J., 1955, Tellus, 7, 22
Charney J. G., Eliassen A., 1949, Tellus, 1, 38
Christensen U. R., Holzwarth V., Reiners A., 2009, Nature, 457, 167
Christie D. A. et al., 2022, PSJ, 3, 261
Cowan N. B., Agol E., 2008, ApJ, 678, L129
Daley R., 1988, Tellus Series A, 40, 96
Dang L. et al., 2018, Nature Astron., 2, 220
Dawson A., 2016, J. Open Res. Softw., 4, e31
de Verdière A. C., Schopp R., 1994, J. Fluid Mech., 276, 233
Deitrick R., Mendonça J. M., Schroffenegger U., Grimm S. L., Tsai S.-M., Heng K., 2020, ApJS, 248, 30
Deitrick R., Heng K., Schroffenegger U., Kitzmann D., Grimm S. L., Malik M., Mendonça J. M., Morris B. M., 2022, MNRAS, 512, 3759
Dobbs-Dixon I., 2009, in Pont F., Sasselov D., Holman M. J., eds, Proc. IAU Symp. 253, Transiting Planets. Cambridge Univ. Press, Cambridge, p. 273
Dobbs-Dixon I., Agol E., 2013, MNRAS, 435, 3159
Dobbs-Dixon I., Cowan N. B., 2017, ApJ, 851, L26
Dobbs-Dixon I., Lin D. N. C., 2008, ApJ, 673, 513
Dobbs-Dixon I., Cumming A., Lin D. N. C., 2010, ApJ, 710, 1395
Draghici I., 1989, Meteorol. Hydrol, 19, 13
Drummond B., Tremblin P., Baraffe I., Amundsen D. S., Mayne N. J., Venot O., Goyal J., 2016, A&A, 594, A69
Drummond B., Mayne N. J., Baraffe I., Tremblin P., Manners J., Amundsen D. S., Goyal J., Acreman D., 2018a, A&A, 612, A105
Drummond B., Mayne N. J., Manners J., Baraffe I., Goyal J., Tremblin P., Sing D. K., Kohary K., 2018b, ApJ, 869, 28
Dutton J. A., 2002, The Ceaseless Wind: An Introduction to the Theory of Atmospheric Motion. Dover Publications, New York
Eckart C., 1960, The Hydrodynamics of Oceans and Atmospheres. Pergamon Press, Oxford
Edson A., Lee S., Bannon P., Kasting J. F., Pollard D., 2011, Icarus, 212, 1
Elson P. et al., 2022, SciTools/cartopy: v0.21.1, Zenodo, available at: https://doi.org/10.5281/zenodo.7430317
Feng Y. K., Line M. R., Fortney J. J., Stevenson K. B., Bean J., Kreidberg L., Parmentier V., 2016, ApJ, 829, 52
Flowers E., Brogi M., Rauscher E., Kempton E. M. R., Chiavassa A., 2019, AJ, 157, 209
Freedman R. S., Lustig-Yaeger J., Fortney J. J., Lupu R. E., Marley M. S., Lodders K., 2014, ApJS, 214, 25
Gastine T., Wicht J., 2021, Icarus, 368, 114514
Gerkema T., Zimmerman J. T. F., Maas L. R. M., van Haren H., 2008, Rev. Geophys., 46, RG2004
Gill A. E., 1982, Atmosphere – Ocean Dynamics. Academic Press, London
Gillon M. et al., 2012, A&A, 542, A4

Guillot T., 2010, A&A, 520, A27
Guillot T., Showman A. P., 2002, A&A, 385, 156
Hammond M., Abbot D. S., 2022, MNRAS, 511, 2313
Hammond M., Lewis N. T., 2021, Proc. Natl Acad. Sci., 118, e2022705118
Hammond M., Pierrehumbert R. T., 2018, ApJ, 869, 65
Hammond M., Tsai S.-M., Pierrehumbert R. T., 2020, ApJ, 901, 78
Harris C. R. et al., 2020, Nature, 585, 357
Heimpel M. H., Yadav R. K., Featherstone N. A., Aurnou J. M., 2022, Icarus, 379, 114942
Hellier C. et al., 2011, A&A, 535, L7
Helling C. et al., 2016, MNRAS, 460, 855
Heng K., Showman A. P., 2015, Annu. Rev. Earth Planet. Sci., 43, 509
Heng K., Menou K., Phillipps P. J., 2011a, MNRAS, 413, 2380
Heng K., Frierson D. M. W., Phillipps P. J., 2011b, MNRAS, 418, 2669
Hindle A. W., Bushby P. J., Rogers T. M., 2019, ApJ, 872, L27
Hollingsworth J. L., Kahre M. A., 2010, Geophys. Res. Lett., 37, L22202
Hoyer S., Hamman J., 2017, J. Open Res. Softw., 5, 10
Hunter J. D., 2007, Comput. Sci. Eng., 9, 90
Irwin P. G. J., Parmentier V., Taylor J., Barstow J., Aigrain S., Lee E. K. H., Garland R., 2020, MNRAS, 493, 106
Jones E., Oliphant T., Peterson P., 2001, SciPy: Open Source Scientific Tools for Python, https://www.scipy.org
Kataria T., Showman A. P., Fortney J. J., Marley M. S., Freedman R. S., 2014, ApJ, 785, 92
Kataria T., Showman A. P., Fortney J. J., Stevenson K. B., Line M. R., Kreidberg L., Bean J. L., Désert J.-M., 2015, ApJ, 801, 86
Kataria T., Sing D. K., Lewis N. K., Visscher C., Showman A. P., Fortney J. J., Marley M. S., 2016, ApJ, 821, 9
Kelly K., Šavrič B., 2021, Trans. GIS, 25, 6
King J. I. F., 1956, ApJ, 124, 272
Kluyver T. et al., 2016, in Fernando L., Birgit S., eds, Positioning and Power in Academic Publishing: Players, Agents and Agendas, IOS Press, p. 87
Knutson H. A. et al., 2007, Nature, 447, 183
Koll D. D. B., Abbot D. S., 2015, ApJ, 802, 21
Komacek T. D., Showman A. P., 2016, ApJ, 821, 16
Komacek T. D., Showman A. P., Tan X., 2017, ApJ, 835, 198
Komacek T. D., Showman A. P., Parmentier V., 2019, ApJ, 881, 152
Komacek T. D., Gao P., Thorngren D. P., May E. M., Tan X., 2022, ApJ, 941, L40
Lebonnois S., Hourdin F., Eymet V., Crespin A., Fournier R., Forget F., 2010, J. Geophys. Res. (Planets), 115, E06006
Lee E. K. H., Casewell S. L., Chubb K. L., Hammond M., Tan X., Tsai S.-M., Pierrehumbert R. T., 2020, MNRAS, 496, 4674
Lee E. K. H., Parmentier V., Hammond M., Grimm S. L., Kitzmann D., Tan X., Tsai S.-M., Pierrehumbert R. T., 2021, MNRAS, 506, 2695
Lee E. K. H., Prinoth B., Kitzmann D., Tsai S.-M., Hoeijmakers J., Borsato N. W., Heng K., 2022, MNRAS, 517, 240
Lines S. et al., 2018a, MNRAS, 481, 194
Lines S. et al., 2018b, A&A, 615, A97
Mathis S., Prat V., 2019, A&A, 631, A26
May E. M. et al., 2022, AJ, 163, 256
Mayne N. J., Baraffe I., Acreman D. M., Smith C., Wood N., Amundsen D. S., Thuburn J., Jackson D. R., 2014a, Geosci. Model Develop., 7, 3059
Mayne N. J. et al., 2014b, A&A, 561, A1
Mayne N. J. et al., 2017, A&A, 604, A79
Mayne N. J., Drummond B., Debras F., Jaupart E., Manners J., Boutle I. A., Baraffe I., Kohary K., 2019, ApJ, 871, 56
Mayor M., Queloz D., 1995, Nature, 378, 355
Mendonça J. M., 2020, MNRAS, 491, 1456
Mendonça J. M., Grimm S. L., Grosheintz L., Heng K., 2016, ApJ, 829, 115
Mendonça J. M., Grimm S. L., Grosheintz L., Heng K., 2018a, Astrophysics Source Code Library, record ascl:1807.010
Mendonça J. M., Malik M., Demory B.-O., Heng K., 2018b, AJ, 155, 150
Mendonça J. M., Tsai S.-m., Malik M., Grimm S. L., Heng K., 2018c, ApJ, 869, 107
Menou K., 2012, ApJ, 744, L16
Met Office, 2010–2015, Cartopy: a Cartographic Python Library with a Matplotlib Interface. Exeter, Devon, available at:https://scitools.org.uk/cartopy
Müller-Wodarg I. C. F., Mendillo M., Yelle R. V., Aylward A. D., 2006, Icarus, 180, 147
Nagler P. C. et al., 2019, J. Astron. Instrum., 08, 1950011
Navier C., 1823, Mém. Acad. R. Sci. Inst. France, 6, 389
Noda S. et al., 2017, Icarus, 282, 1
Norbury J., Roulstone I., 2002a, Large-Scale Atmosphere-Ocean Dynamics, Vol. 1: Analytical Methods and Numerical Models. Cambridge Univ. Press, Cambridge
Norbury J., Roulstone I., 2002b, Large-Scale Atmosphere-Ocean Dynamics: Volume 2: Geometric Methods and Models. Cambridge University Press
Olson G. L., Kunasz P. B., 1987, J. Quant. Spec. Radiat. Transf., 38, 325
The pandas development team, 2020, pandas-dev/pandas: Pandas, Zenodo, available at: https://doi.org/10.5281/zenodo.3509134
Parmentier V., 2014, PhD thesis, Laboratoire Universitaire d'Astrophysique de Nice; Observatoire de la Cote d'Azur, France
Parmentier V., Crossfield I. J. M., 2018, in Deeg H. J., Belmonte J. A., eds, Handbook of Exoplanets. Springer International Publishing AG, Cham, p. 116
Parmentier V., Guillot T., 2014, A&A, 562, A133
Parmentier V., Guillot T., Fortney J. J., Marley M. S., 2015, A&A, 574, A35
Parmentier V., Fortney J. J., Showman A. P., Morley C., Marley M. S., 2016, ApJ, 828, 22
Parmentier V., Showman A. P., Fortney J. J., 2021, MNRAS, 501, 78
Phillips N., 1990, WMO-No. 700, World Meteorological Organization, Geneva
Rauscher E., Kempton E. M. R., 2014, ApJ, 790, 79
Rauscher E., Menou K., 2010, ApJ, 714, 1334
Rauscher E., Menou K., 2012, ApJ, 750, 96
Richardson L. F., 1922, Quart. J. Royal Meteorol. Soc., 48, 282
Ricker G. R. et al., 2014, in Oschmann J. M., Jr, Clampin M., Fazio G. G., MacEwen H. A., eds, Proc. SPIE Conf. Ser. Vol. 9143, Space Telescopes and Instrumentation 2014: Optical, Infrared, and Millimeter Wave. SPIE, Bellingham, p. 914320
Rogers T. M., Komacek T. D., 2014, ApJ, 794, 132
Sainsbury-Martinez F. et al., 2019, A&A, 632, A114
Schneider A. D., Carone L., Decin L., Jørgensen U. G., Mollière P., Baeyens R., Kiefer S., Helling C., 2022, A&A, 664, A56
Schneider T., Liu J., 2009, J. Atmos. Sci., 66, 579
Sergeev D. E. et al., 2022a, PSJ, 3, 212
Sergeev D. E., Lewis N. T., Lambert F. H., Mayne N. J., Boutle I. A., Manners J., Kohary K., 2022b, PSJ, 3, 214
Sergeev D. E. et al., 2023, preprint (arXiv:2306.03614)
Showman A. P., Guillot T., 2002, A&A, 385, 166
Showman A. P., Polvani L. M., 2011, ApJ, 738, 71
Showman A. P., Cooper C. S., Fortney J. J., Marley M. S., 2008, ApJ, 682, 559
Showman A. P., Fortney J. J., Lian Y., Marley M. S., Freedman R. S., Knutson H. A., Charbonneau D., 2009, ApJ, 699, 564
Showman A. P., Cho J. Y. K., Menou K., 2010, in Seager S., ed., Exoplanets. Univ. Arizona Press, p. 471
Showman A. P., Lewis N. K., Fortney J. J., 2015, ApJ, 801, 95
Showman A. P., Tan X., Parmentier V., 2020, Space Sci. Rev., 216, 139
Stevenson K. B. et al., 2016, PASP, 128, 094401
Stokes G. G., 1845, Trans. Camb. Phil. Soc., 8, 287
Stokes G. G., 1846, Rep. Br. Assoc. Adv. Sci., 1, 1
Sukoriansky S., Dikovskaya N., Galperin B., 2007, J. Atmos. Sci., 64, 3312
Tan X., Komacek T. D., 2019, ApJ, 886, 26
Tan X., Showman A. P., 2020, ApJ, 902, 27
Tanguay M., Robert A., Laprise R., 1990, Mon. Weather Rev., 118, 1970
Taylor J., Parmentier V., Irwin P. G. J., Aigrain S., Lee E. K. H., Krissansen-Totton J., 2020, MNRAS, 493, 4342
Thorngren D., Gao P., Fortney J. J., 2019, ApJ, 884, L6
Thrastarson H. T., Cho J. Y.-K., 2011, ApJ, 729, 117
Thuburn J., Wood N., Staniforth A., 2002, Q. J. R. Meteorol. Soc., 128, 1771

Tinetti G. et al., 2016, in MacEwen H. A., Fazio G. G., Lystrup M., Batalha N., Siegler N., Tong E. C., eds, Proc. SPIE Conf. Ser. Vol. 9904, Space Telescopes and Instrumentation 2016: Optical, Infrared, and Millimeter Wave. SPIE, Bellingham, p. 99041X
Tokano T., 2013, Geophys. Res. Lett., 40, 4538
Tort M., Dubos T., Melvin T., 2015, Q. J. R. Meteorol. Soc., 141, 3056
Tremblin P. et al., 2017, ApJ, 841, 30
Tsai S.-M., Dobbs-Dixon I., Gu P.-G., 2014, ApJ, 793, 141
Turbet M. et al., 2022, PSJ, 3, 211
Van de Ven B., Eswaramoorthy P., Metzger T. C., Paprocki M., Rudiger P., Thomas I., 2022, Bokeh. Available at:https://github.com/bokeh/bokeh
Van Rossum G., Drake F. L., 1995, Python tutorial. Centrum voor Wiskunde en Informatica, Amsterdam, The Netherlands, https://www.python.org/
Venot O. et al., 2020, ApJ, 890, 176
Virtanen P. et al., 2020, Nat. Meth., 17, 261
Wang H., Wordsworth R., 2020, ApJ, 891, 7
Waskom M., 2021, J. Open Source Softw., 6, 3021
White A. A., Bromley R. A., 1995, Q. J. R. Meteorol. Soc., 121, 399
White A. A., Hoskins B. J., Roulstone I., Staniforth A., 2005, Q. J. R. Meteorol. Soc., 131, 2081
Yadav R. K., Thorngren D. P., 2017, ApJ, 849, L12
Yamazaki Y. H., Skeet D. R., Read P. L., 2004, Planet. Space Sci., 52, 423
Youdin A. N., Mitchell J. L., 2010, ApJ, 721, 1113
Zeitlin V., 2018, Geophysical Fluid Dynamics: Understanding (Almost) Everything With Rotating Shallow Water Models. Oxford University Press
Zhang X., Showman A. P., 2017, ApJ, 836, 73

SUPPORTING INFORMATION

Supplementary data are available at *MNRAS* online.

suppl_data

Please note: Oxford University Press is not responsible for the content or functionality of any supporting materials supplied by the authors. Any queries (other than missing material) should be directed to the corresponding author for the article.

APPENDIX A: TIDALLY LOCKED COORDINATES AND VELOCITIES

For analysis of symmetries in the atmosphere of a tidally locked planet, we make use of the 'tidally locked coordinate system' suggested by Koll & Abbot (2015). In the transformation, the traditional latitude-longitude system (ϑ, λ) get replaced by the 'tidally locked coordinate system' (ϑ', λ') as the following:

The coordinates are effectively a rotation of regular latitude-longitude coordinates, so that the polar axis runs from the substellar point to the antistellar point. They define the tidally locked latitude $\vartheta 0$ to be the angle to the terminator and the tidally locked longitude to be the angle about the substellar-antistellar axis. That rotation of the coordinate system results into the tidally locked coordinates according to Koll & Abbot (2015) as

$$\vartheta' = sin^{-1}(\cos\vartheta\,\cos\lambda), \tag{A1a}$$

$$\lambda' = tan^{-1}\left(\frac{\sin\lambda}{\tan(\vartheta)}\right), \tag{A1b}$$

where ϑ' is the tidally locked latitudes, λ' the tidally locked longitude, ϑ the original latitude, and λ' the orginal longitude. The tidally locked wind velocities consist of fractions of the original zonal and meridional wind components. The fractions change depending on the coordinates. According to Koll & Abbot (2015), the tidally locked zonal and meridional wind u' and v' are defined as

$$u' = \cos\vartheta\left(\frac{\partial\lambda'}{\partial\lambda}\frac{u}{\cos\vartheta} + \frac{\partial\lambda'}{\partial\vartheta}v\right), \tag{A2a}$$

$$v' = \frac{\partial\vartheta'}{\partial\lambda}\frac{u}{\cos\vartheta} + \frac{\partial\vartheta'}{\partial\vartheta}v, \tag{A2b}$$

where u and v are the zonal and meridional wind components of the original coordinate system.

APPENDIX B: STREAMFUNCTION AND TIDALLY LOCKED STREAMFUNCTION

For analysing the mass flow, we performed the tidally locked streamfunction Ψ' and the Eulerian mean meridional streamfunction Ψ in the same fashion as Hammond & Lewis (2021) as

$$\Psi = \frac{2\pi a\cos\vartheta}{g}\int_0^p [v]_\lambda \mathrm{d}p, \tag{B1a}$$

$$\Psi' = \frac{2\pi a\cos\vartheta'}{g}\int_0^p [v']_{\lambda'} \mathrm{d}p, \tag{B1b}$$

where g declares the gravity, a the equatorial radius, $[v]_\lambda$ averaged wind over longitude, and the $[v']_{\lambda'}$ an averaged wind over tidally locked longitude.

APPENDIX C: HELMHOLTZ DECOMPOSITION

We performed a Helmholtz decomposition, according to Hammond & Lewis (2021), to analyse changes due to altered parameters in our grid that might be discovered in the components of the total circulation such as the overturning circulation, stationary waves, and superrotating jet. In the Helmholtz decomposition, the total circulation is split up into the divergent and rotational components, u_d and u_r (Dutton 2002):

$$u = u_d + u_r \tag{C1a}$$

$$= \nabla\chi + k\times\nabla\psi, \tag{C1b}$$

where χ stands for the velocity potential function and ψ for a streamfunction, which are defined as:

$$\nabla^2\,\chi = \delta, \tag{C2a}$$

$$\nabla^2\,\psi = \zeta, \tag{C2b}$$

where δ is the divergence and ζ the vorticity.

APPENDIX D: OLR PHASE CURVE

Cowan & Agol (2008) formulated the phase curve as

$$F = \int_{\lambda_1}^{\lambda_2}\int_{\vartheta_1}^{\vartheta_2}\int_{-\pi/2}^{\pi/2} R^2\frac{F_{TOA}}{\pi}\cos^2(\theta)\cos(\vartheta-\alpha)\,\mathrm{d}\phi\,\mathrm{d}\vartheta\,\mathrm{d}\lambda, \tag{D1}$$

where F_{TOA} is the flux at the top of the atmosphere coming from the each atmospheric column of the GCM at a given wavelength λ, ϕ, and ϑ, declaring the latitude and longitude and α the orbital phase angle. Deitrick et al. (2022) introduced a formalism to calculate the F on an icosahedral grid as

$$F = \sum_{i=1}^{N_{grid}}\frac{F_{TOA,i}}{\pi}\mu_i\frac{A_i}{R_p^2}, \tag{D2}$$

where A_i declares the area of each control volume at the top of the atmosphere R_p, the radius of the planet and

$$\mu_i = \begin{cases} \cos(\phi)\cos(\vartheta - \alpha), & \alpha - \frac{\pi}{2} < \vartheta < \alpha + \frac{\pi}{2}, \\ 0, & \vartheta > \alpha + \frac{\pi}{2} \; or \; \vartheta < \alpha - \frac{\pi}{2}. \end{cases} \tag{D3}$$

We take the approach of Deitrick et al. (2022) to adapt it to a longitude-latitude grid and limit it to long-wave radiation. Kelly & Švarič (2021) defined the surface area of a grid-cell in a longitude-latitude grid on the sphere as

$$\begin{aligned} A_S &= \int_{\phi 1}^{\phi 2} \int_{\vartheta 1}^{\vartheta 2} R_p^2 \cos(\vartheta)\, \mathrm{d}\phi\, \mathrm{d}\vartheta \\ &= R_p^2(\vartheta 2 - \vartheta 1)(\sin(\phi_2) - \sin(\phi_1)). \end{aligned} \tag{D4}$$

By switching to longitude-latitude grid, we modify the equation (D2) with equation (D4) and reformulate as OLR phase curve as

$$F_{OLR} = \sum_{i=1}^{N_{grid}} \frac{F_{OLR,TOA,i}}{\pi} \mu_i(\Delta\vartheta)(\sin(\phi + \Delta\phi) - \sin(\phi - \Delta\phi)) \tag{D5}$$

where $\Delta\vartheta$ is the longitudinal width of a grid cell and $\Delta\phi$ the latitudinal width; and we defined μ_i as

$$\mu_i = \begin{cases} \cos(\phi)\cos(\vartheta - \alpha), & \cos(\phi)\cos(\vartheta - \alpha) \geq 0, \\ 0, & \cos(\phi)\cos(\vartheta - \alpha) < 0. \end{cases} \tag{D6}$$

APPENDIX E: RADIATIVE AND ZONAL TIME-SCALES

We computed the radiative time-scale as in Showman & Guillot (2002) as

$$\tau_{rad} \sim \frac{P}{g} \frac{c_p}{4\sigma_B T^3}, \tag{E1}$$

where $P\,[Pa]$ declares the pressure, $g\,[ms^{-2}]$ the gravity, σ_B the Stefan-Boltzmann constant, $c_p\,[Jkg^{-1}K^{-1}]$ the heat capacity at constant pressure, and $T\,[K]$ the temperature. The zonal time-scales were calculated as well like in Showman & Guillot (2002) as

$$\tau_{znd} \gtrsim \frac{R}{u_{max}}, \tag{E2}$$

where R is the planetary radius and u_{max} the maximum of the zonal wind speed. We computed the radiative and zonal time-scale for each layer with the related values.

APPENDIX F: LARGE-SCALE FLOW QUANTITIES

For the analytics, we used several quantities for the large-scale flow characteristics. The scale height H is defined in Parmentier (2014), and we reformulated it as

$$H = \frac{k_B T}{mg} = \frac{R_d T}{g}, \tag{F1}$$

where $k_B\,[m^2kgs^{-2}K^{-1}]$ is the Bolzmann constant, $T\,[K]$ the temperature of the gas, $g\,[ms^{-2}]$ the gravity, $m\,[kg]$ the mass of the gas, and $R_d\,[Jkg^{-1}K^{-1}]$ the specific gas constant.

The Rossy number indicates the balance in the momentum equation between the Coriolis and the advection term (Parmentier 2014; Kataria et al. 2016):

$$Ro \equiv \frac{U}{fL}, \tag{F2}$$

where $L\,[m]$ is the typical horizontal scale, $U\,[m/s]$ the typical wind speed, and $f\,[rads^{-1}]$ the Coriolis parameter as

$$f = 2\Omega \sin(\vartheta), \tag{F3}$$

where $\Omega\,[rad]s^{-1}$ represents the rotation rate of the planet and $\vartheta[rad]$ the latitude. The typical horizontal scale is typically calculated as the Rossby deformation radius $L_D\,[m]$ (see hereafter). The Coriolis force becomes negligible, and the advection, pressure gradient, and dissipation remain the terms relevant in the force balance, when the Rossby number is much larger than one (Parmentier 2014). On the other hand, a much smaller Rossby number indicates a force balance among pressure gradient and Coriolis force.

Pressure gradients may equalized by gravity waves, unless the gravity waves are not deflected by Coriolis force. The Rossby deformation radius $L_D\,[m]$ defines the distance at which the gravity waves get deflected by the Coriolis force (Parmentier 2014):

$$L_D = \frac{ND}{f}, \tag{F4}$$

where $N\,[s^{-1}]$ is the Brunt–Väisälä frequency (actually the oscillation frequency of gravity waves) and $D\,[m]$ the vertical length scale of the atmosphere. The vertical length scale of the atmosphere is calculated at the order of one scale height, so $D = H$. The the Brunt–Väisälä frequency is defined in an isothermal atmosphere as (Parmentier 2014):

$$N = \sqrt{\frac{c_p g}{R_d H}}, \tag{F5}$$

where $c_p[JK^{-1}]$ represents the heat capacity [we corrected a typing mistake in Parmentier (2014)]. The Rhines scale L_{Rh} indicates the scale at which the transition from dominant linear advection to the appearance of an inverse cascade occurs. The inverse cascade is the energy injection of small scales vortices into larger atmospheric flow. The Rhines scale is also known as the indicator of flow reorganization into the bands of alternating zonal jets, often called zonation (Sukoriansky, Dikovskaya & Galperin 2007). In unsteady flow regimes, the Rhine scale might be associated with the moving energy front propagating towards the decreasing wavenumbers. The Rhines scale is defined as (Parmentier 2014):

$$L_{Rh} = \pi \sqrt{\frac{U}{\beta}}, \tag{F6}$$

where β corresponds to the meridional gradient of the Coriolis force, which is also known as the 'β-effect, and defined as (Parmentier 2014; Kataria et al. 2016):

$$\beta = \frac{2\Omega \cos(\vartheta)}{R_p}, \tag{F7}$$

where R_p is the radius of the planet.

This paper has been typeset from a TEX/LATEX file prepared by the author.